BLOCK COPOLYMER DERIVED MESOPOROUS THIN FILMS: PROCESSING, CHARACTERIZATION, AND APPLICATIONS

A Dissertation

Presented to the Faculty of the Graduate School

of Cornell University

in Partial Fulfillment of the Requirements for the Degree of

Doctor of Philosophy

by

Phong Du

May 2006

© 2006 Phong Du

ALL RIGHTS RESERVED

BLOCK COPOLYMER DERIVED MESOPOROUS THIN FILMS: PROCESSING, CHARACTERIZATION, AND APPLICATIONS

Phong Du, Ph.D.

Cornell University 2006

The development of diblock copolymers as structure directing agents for phase selective additives to generate thin films is discussed. Different systems ranging from pure organic [(poly(αmethyl styrene–block–4-hydroxystyrene) and poly(α styrene–block–isoprene) with photoactive crosslinkers] to an organic-inorganic [poly(isoprene–block–ethylene oxide) with 3-glycidyloxypropyltrimethoxysilane and aluminum-tri-sec-butoxide] to a non-oxide high temperature system [poly(isoprene–block–dimethylamino ethylmethacrylate) with a polyureamethylvinylsilazane additive] are explored. Characterization is accomplished through a variety of techniques (atomic force microscopy, scanning electron microscopy, grazing incidence small angle x-ray scattering, nuclear magnetic resonance, and Rutherford backscattering) and supplemented by quantitative analysis (radial and bond orientation distribution functions, Voronoi diagrams, and GISAXS simulations). Hybrid organic-inorganic mesoporous monolayer thin films are used as templates to structure silicon at the $\sim$30 nm length scale through a transient laser induced melt and capillarity driven pore filling process.

BIOGRAPHICAL SKETCH

Phong was born in Saigon, Vietnam and immigrated to the United States with his family in the early 1980s. He was raised in the Southern Californian communities of Glendale and La Mirada and developed an early liking of the sciences and mathematics. Some of his favorite T.V. shows include The Simpsons, Freaks and Geeks, Arrested Development, Stargate, Futurama, MacGyver, The A-Team, The Smurfs, Duck Tales, and just about every other after school cartoon show. He relished waking early on Saturdays to catch those wonderful weekend toons (currently unavailable at press time). He planted a tree once—long ago—back at his elementary school and has yet return to see it. He enjoyed playing basketball and his weekly bike trip to the local comic book store (Marvels, Kingdom Come, The Long Halloween, Red Son) during his youth.

Phong first attended La Mirada High School in 1990 as an entry level nerd. At graduation: über nerd. He graduated as valedictorian in 1995 and attended the University of California, Los Angeles for his undergraduate studies in Applied Mathematics and Physics. He enjoyed the UCLA campus and all the wonderful and crazy things offered by Los Angeles. Early attempts at being a pirate were scrubbed after he realized he possessed neither the peg leg(s) nor parrots for the role. He especially enjoyed his ESS 20 class; camping all over California visiting national parks, deserts, and beaches cataloging plants and rocks. He briefly toured Europe.

His graduate career at Cornell University in Materials Science and Engineer began in the fall of 2000 and starting working for Professor Ulrich Wiesner in the field of polymer science. He had no idea what "PIPEO" was for a solid month. Thanksgiving Eve 2000 was the time he busted his face either in a bar fight or chasing after a bus. It was at Cornell that he met his beautiful wife, Surbhi, and they married in early 2006.

To my family and friends for all their support

ACKNOWLEDGEMENTS

There are so many people that deserve to be in this section for all their help during my time at Cornell. First and foremost, my parents and family for all the support they have provided, not just during my tenure here, but for as long as I can remember. My friends from La Mirada, especially Dan, Nick, Raj, Chris, and Kenneth, for always being available and coming together during those rare times that I make it back to California despite having their own busy lives to conduct.

Those friends I've made here at Cornell, friends that I'm sure will always be a part of my life, that made my stay all the more enjoyable. My great poker buddies, Luke, Darren, Nowak, Kneppler, Jon, Ray, Doobie, Marvin, and Tom, that always kept things interesting week in, week out. The people in the Bard office, Joseph, Carol, Patty, Vicki, and Julie, that were always willing to lend a helping hand and a pleasure to speak to. All the facility managers, John S., Mick, Yuanming, John H., John G., and Carol and the CHESS staff, Detlef, Arthur, and Ernie, who directly helped with my research. Connie and Shahyaan for their invaluable help with the excimer laser experiments and general company.

My advisor, for the patience with putting up with an "incorrigible" student.

And my wonderful wife, for sticking with me through it all.

BORT OUT!

"In the kingdom of hope, there is no winter."

TABLE OF CONTENTS

LIST OF TABLES

LIST OF FIGURES

CHAPTER 1

INTRODUCTION

The ability to manipulate matter on surfaces in the range of tens to hundreds of nanometers is of great importance to a variety of ever evolving technologies that demand greater precision, accuracy, and functionality. Block copolymer thin films ($<$150 nm) are one of the more promising routes being examined for this task as they offer ease of processing and "bottom-up" phase separation induced structure formation on the nanometer length scale. To further their utility, small molecule-type additives enhance and/or introduce new materials properties, such as mechanical and thermal strength, beyond those found in the parent block copolymer systems. Applications developed from these mesostructured surfaces demand user-controlled precision and accuracy which remains a challenging aspect of these systems.

Control over pure organic block copolymer thin film ordering have been achieved through use of electric fields [1, 2], flow fields [3], surface interactions [4–7], and solvent vapor annealing [8, 9]. Substantially well-ordered films were achieved through lengthy treatment times (c.a. hours to days) to insure the defects annealed out of the film. The fast developing field of nanotechnology demanded further functionality to develop applications such as sensors, optoelectronics devices, and supports for separation and catalysis [10–12]. The transition to a hybrid organic-inorganic thin film system was pioneered by Wiesner et al. [13] through the addition of an inorganic aluminiosilicate component. While providing added functionality, this new component complicates the energy landscape and limits the available processes to affect the ordering within the thin film. Two competing mechanisms, namely the polymer mobility and the crosslinking rate of the inorganic species, make it challenging to optimize the thin film ordering in these hybrid systems.

Here, I report on the development of amphiphilic copolymers as structure directing agents for small molecule additives to form functional mesostructured thin films. The different systems co-assemble into well-defined morphologies through enthalpic and entropic optimization, incorporating the additives into the material. Chapter 2 deals with the concept of introducing additives that are selective to only one phase of the copolymer. Two systems, poly(αmethyl styrene–b–4-hydroxystyrene) and poly(α styrene–b–isoprene) with crosslinking agents, are used with "top-down" techniques to generate thin films structured both on the macro- and mesoscale. A third system, poly(isoprene–b–ethylene oxide) with the additives aluminum-tri-sec-butoxide and 3-glycidyloxypropyltrimethoxysilane, transitions from previous all-organic systems to a hybrid system that opens up additional opportunities through the introduction of new materials properties associated with the inorganic additives.

The hybrid organic-inorganic system is further discussed in Chapter 3 in greater detail. Thin film samples ranging from mono- to multilayer assemblies are characterized through a variety of methods, both on the local (Atomic Force and Scanning Electron Microscopy) and global (Grazing Incidence Small Angle X-ray Scattering) scale, with the various techniques providing complimentary data. Quantitative analysis (Voronoi diagrams, radial and bond orientation distribution functions, and GISAXS simulations) identifies numerous sample characteristics (e.g. grain size, defect density, type and location, angular distribution, film thickness, scattering object geometry, aspect ratio, and ordering regime) and gauges the development of the thin film system. Links between processing/composition parameters and final film quality and ordering are established and facilitate making the proper decisions for targeted film dimensions and ordering specifically tailored to meet the end users' needs.

Chapter 4 leverages the advances made from the previous chapters, in particular the transition to an aluminosilicate system (gaining thermal stability) and the development of good ordering, to structure silicon at the nanometer length scale through a completely novel method. These inorganic monolayer-type thin films ($\sim$20 nm) are employed as templates for a laser induced capillary driven filling process to create nanopillar arrays with a characteristic spacing ($\sim$30 nm) not easily accessible with current photolithographic techniques. Samples are irradiated with several 30 ns pulses from a XeCl excimer laser (λ=308 nm) at a fluence sufficient to melt the underlying silicon substrate and fill the nanopores. Characterization of the surface before and after laser melt confirms an efficient pattern transfer and registry between the parent template and nanopillar arrays. High aspect ratio nanopillars are achieved through deposition of amorphous silicon to help fill the pores from the top of the template during the laser melt process. Placement of these arrays can be controlled through the use of a mask to determine the pattern of the laser irradiated surface.

Generalization to non-oxide thin films, especially materials with high temperature resistance is discussed in Chapter 5. A different diblock copolymer poly(isoprene–b–dimethylamino ethylmethacrylate) is used with a polyureamethylvinylsilazane to generate SiC and SiCN materials. The selection of a new inorganic additive presents some interesting challenges, in particular its compatibility with the copolymer and the protection of its chemical integrity. The thin film geometry proves especially important to the determination of chemical composition through nuclear magnetic resonance and Rutherford backscattering measurements.

Bibliography

[1] P. Mansky, J. DeRouchey, T. P. Russell, J. Mays, M. Pitsikalis, T. Morkved, and H. Jaeger. "Large-area domain alignment in block copolymer thin films using electric fields" *Macromolecules*, **1998**, *31*, 4399.

[2] T. L. Morkved, M. Lu, A. M. Urbas, E. E. Ehrichs, H. M. Jaeger, P. Mansky, and T. P. Russell. "Local control of microdomain orientation in diblock copolymer thin films with electric fields" *Science*, **1996**, *273*, 931.

[3] D. E. Angelescu, J. H. Waller, R. A. Register, and P. M. Chaikin. "Shear-induced alignment in thin films of spherical nanodomains" *Adv. Mater.*, **2005**, *17*, 1878.

[4] P. Mansky, T. P. Russell, C. J. Hawker, M. Pitsikalis, and J. Mays. "Ordered diblock copolymer films on random copolymer brushes" *Macromolecules*, **1997**, *30*, 6810.

[5] R. D. Peters, X. M. Yang, and P. F. Nealey. "Morphology of thin films of diblock copolymers on surfaces micropatterned with regions of different interfacial energy" *Macromolecules*, **2002**, *35*, 1822.

[6] E. Huang, T. P. Russell, C. Harrison, P. M Chaikin, R. A. Register, C. Hawker, and J. Mays. "Using surface active random copolymers to control the domain orientation in diblock copolymer thin films" *Macromolecules*, **1998**, *31*, 7641.

[7] X. M. Yang, R. D. Peters, P. F. Nealey, H. H. Solak, and F. Cerrina. "Guided self-assembly of symmetric diblock copolymer films on chemically nanopatterned substrates" *Macromolecules*, **2000**, *33*, 9575.

[8] P. Muller-Buschbaum, J. S. Gutmann, M. Wolkenhauer, J. Kraus, M. Stamm, D. Smilgies, and W. Petry. "Solvent-induced surface morphology of thin polymer films" *Macromolecules*, **2001**, *34*, 1369.

[9] G. Krausch and R. Magerle. "Nanostructured thin films via self-assembly of block copolymers" *Advanced Materials*, **2002**, *14*, 1579.

[10] T. Thurn-Albrecht, J. Schotter, C. A. Kastle, N. Emley, T. Shibauchi, L. Krusin-Elbaum, K. Guarini, C. T. Black, M. T. Tuominen, and T. P. Russell. "Ultrahigh-density nanowire arrays grown in self-assembled diblock copolymer templates" *Science*, **2000**, *290*, 2126.

[11] A. Urbas, R. Sharp, Y. Fink, E. L. Thomas, M. Xenidou, and L. J. Fetters. "Tunable block copolymer/homopolymer photonic crystals" *Advanced Materials*, **2000**, *12*, 812.

[12] K. Asakawa, T. Hiraoka, H. Hieda, M. Sakurai, and Y. Kamata. "Nano-patterning for patterned media using block-copolymer" *Journal of Photopolymer Science and Technology*, **2002**, *15*, 465.

[13] P. Du, J. S. Gutmann, P. F. W. Simon, C. B. W. Garcia, K. Guarini, C. T. Black, and U. Wiesner. "Nanostructured organic-inorganic hybrid thin films" *Polymer Preprints*, **2002**, 43, 438.

CHAPTER 2

ADDITIVE DRIVEN PHASE SELECTIVE CHEMISTRY IN BLOCK COPOLYMER THIN FILMS: THE CONVERGENCE OF TOP-DOWN AND BOTTOM-UP APPROACHES

Introduction

The routine formation of nm-size structures remains a challenge that limits advances in many fields of nanotechnology. Increasingly "bottom-up" self-assembly approaches for the nanometer scale patterning of surfaces are competing with traditional "top-down" lithographic processes such as scanned probe lithography or high-resolution e-beam lithography. Block copolymer thin films ($<$100 nm) are among the more promising materials being examined as they offer ease of processing combined with phase separation induced structure formation on the nm-scale.

Recent work in block copolymer thin film pattern formation has included the use of poly(styrene–b–isoprene) to form periodic structures combined with ozonolysis to remove the isoprene phase thereby creating arrays of holes in the polymer thin film [1]. In another case, poly(styrene–b–methyl methacrylate) has been processed in electric fields to align a cylinder phase perpendicular to the film surface, and subsequently exposed to UV light to both mildly crosslink the styrene phase and degrade the methyl methacrylate domains [2]. Similar strategies have been employed to process other block copolymer systems that contain a variety of chemical structures and architectures [3–6]. Examples of desirable target applications of such porous thin films include photonic band gap materials, structures to serve as molecular sieves, or templates for magnetic structures [7–9].

A typical means for improving the processing of bulk polymers is through the use

of small molecule additives [10]. While such additives in bulk polymer structures are ubiquitous, their application in block copolymer thin film processing has not been substantially explored to date. Given the enormous numbers of property variations possible this is surprising. Here we will show several strategies for the use of additive-driven chemistries that take place in only one type of the nanosized domains of the block copolymer thin films. We then use such an approach to examine the convergence of "top down" with "bottom up" fabrication through light driven processes.

Experimental

Polymer synthesis

(PαMS–b–HOST): Block copolymers of poly(α-methylstyrene–b–4-tert-butoxy styrene), PαMS–b–PtBuOS, were synthesized by sequential anionic polymerization in THF at -78°C with sec-butyl lithium as the initiator. The α-methylstyrene monomer was polymerized first for 12 hours and an aliquot of poly(α-methyl styryl lithium) was isolated for analysis after termination with degassed methanol. The 4-tert-butoxystyrene monomer was then introduced into the reactor and the reaction was terminated with degassed methanol after 12 hours. The PαMS-b-tBuOS was converted to poly(α-methylstyrene–b–4-hydroxystyrene), PαMS–b–HOST, by a hydrolysis reaction. The block copolymer was first dissolved in dioxane, and a 10 fold amount of hydrochloric acid was added. The mixture was reacted at 80°C under an atmosphere of nitrogen overnight and then precipitated into water. After neutralization with a 5 wt% NaOH solution to a pH value of 6-7, the resulting polymer was filtered and dried under vacuum at room temperature. The resulting polymer underwent a dissolution-precipitate cycle from a THF solution to methanol/water (v/v=1/1) mixture twice and finally freeze-dried

from dioxane. Characterization by GPC and 1H-NMR revealed a composition of 28.5% PαMS by weight and molecular weight of 45,400 g/mol (PDI 1.1).

P(αMS–b–I): The asymmetric diblock copolymer poly(α-methyl styrene–b–isoprene) was kindly provided by Lewis Fetters, then at Exxon. Characterization by GPC and ^{1}H-NMR revealed a composition of 25% PαMS by weight and molecular weight of 64,000g/mol (PDI 1.1).

P(I-b-EO): The block copolymer P(I-b-EO) was synthesized using anionic polymerization as described in J. Allgaier, A. Poppe, L. Willner, D. Richter, Macromolecules 1997, 30, 1582. Characterization by GPC and ^{1}H-NMR revealed a composition of 32% PEO by weight and molecular weight of 38,700g/mol (PDI $<$1.1).

(PαMS–b–HOST): A sample of the PαMS–b–HOST block copolymer was dissolved with a small amount of tetramethoxymethyl glycouril (4 wt%) as a crosslinker (CL) and triphenylsulfonium trifluorosulfonate (1.6 wt%) as a photoacid generator (PAG) in propylene glycol methyl ether acetate (PGMEA). Spin-coating of the mixture onto a silicon substrate produced vertically aligned cylinder nanodomains over the entire substrate. By irradiation through conventional photomasks and subsequent mixed solvent development, a high resolution photopattern was generated. Subsequent strong UV irradiation on the developed pattern activated the depolymerization process of the PαMS building block, forming nano-sized holes in spatially controlled micron-sized patterns. Photoimaging experiments were performed using a Nikon 248 nm stepper (NA = 0.42 and σ = 0.5) equipped with a KrF excimer laser (Cymer CX-2LS) in the Cornell Nanofabrication Facility for the first exposure. Subsequent exposure with a JBA 1000 DUV Resist Cure Ramp (450 mJ/cm^2 at 250 nm) followed by heating (115°C for 60 sec) was used to crosslink the PHOST matrix. A mixed solvent (cyclohexanone/isopropanol = 1/2 in volume) was used as a developer to form the negative-tone photoresist patterns.

The thickness of the polymer films was examined with a P-10 profilometer. A second irradiation step (70 J/cm^2 at 365 nm) was carried out to remove the PαMS block at 80°C under high vacuum (9*10^{-5} torr).

Nanofabrication

(PαMS-b-I): Poly(α-methyl styrene-b-isoprene) was mixed with 3 wt-% photoinitiator 2,4,6-trimethylbenzoyldiphenylphosphine oxide, provided by BASF (Product: Lucirin TPO) to crosslink the poly(isoprene) matrix before the degradation of the cylindrical α-methyl styrene phase. This phosphine oxide is ideal because it has two main advantages over other types of photoinitiators: high light absorbance and fast photobleaching. A UV source (model SCU 110B from UVEX corporation) was used to crosslink the isoprene block using a peak intensity of λ = 365 nm during exposure of 3 minutes. A film of the polymer was spin coated from a solution of block copolymer and TPO in PGMEA. Subsequent strong UV irradiation on the polymer film activated the depolymerization process of the PαMS building block, forming nano-sized holes in spatially controlled micron-sized patterns.

P(I–b–EO): samples were prepared by spin coating (CEE Model 100CB, velocity: 2000 RPM, duration: 53 seconds) onto silicon wafers from a 0.5 wt% PI–b–PEO polymer solution of equal weight THF/chloroform with a specific amount of added inorganic species (GLYMO/Al(OBu)$_3$). Cross-linking of the film was achieved in a vacuum oven at 130°C for 1 hour. Subsequent calcination was carried out in a furnace at 500°C (temperature ramp: 5°C/min) to remove the organic components.

Characterization

AFM data for Figure 2.2A, B were captured using a Veeco Dimension 3100 Scanning Probe Microscope operated in TappingMode with Olympus TappingMode Etched Silicon probes (resonant frequency = 300kHz, force constant = 42 N/m, tip radius of curvature = 10 nm; all values nominal) under ambient conditions. AFM data for Figure 2.2C was captured using a Veeco Nanoscope III MultiMode Scanning Probe Microscope operated in TappingMode with TappingMode Etched Silicon probes (resonant frequency = 325 kHz, force constant = 37 N/m, tip radius of curvature = 10 nm; all values nominal) under ambient conditions. SEM data for Figure 2.2D was captured using a Hitachi S4500 Field Emission Scanning Electron Microscope operated under conditions of acceleration voltage of 5kV and working distance of 10 mm. GISAXS data of System 3 samples were collected with a 2D area detector (X-ray energy: 8 keV, sample-to-detector distance: 165 cm, angle: $<1^{\circ}$, exposure time: 1-10 seconds).

Results and discussion

In Figure 2.1, the structures of the three polymer systems and their respective phase selective additives are introduced. They are: (System 1) poly(α-methyl styrene–b–4–hydroxystyrene) P(MS–b–HOST), and TMMU with photoacid generator; (System 2) poly(αmethyl styrene–b–isoprene), P(αMS–b–I) and TPO; & (System 3) poly(isoprene-b–ethylene oxide), P(I–b–EO) and GLYMO/Al(OBu)$_3$. While the first two systems are all-organic, in the case of P(I–b–EO) inorganic additives were used. All polymers were produced using living anionic polymerization, because of its excellent control of architecture and molecular weight [See Figure 2.1]. Films of various controlled thicknesses down to monolayer behavior (see below) were obtained by spin coating from dilute

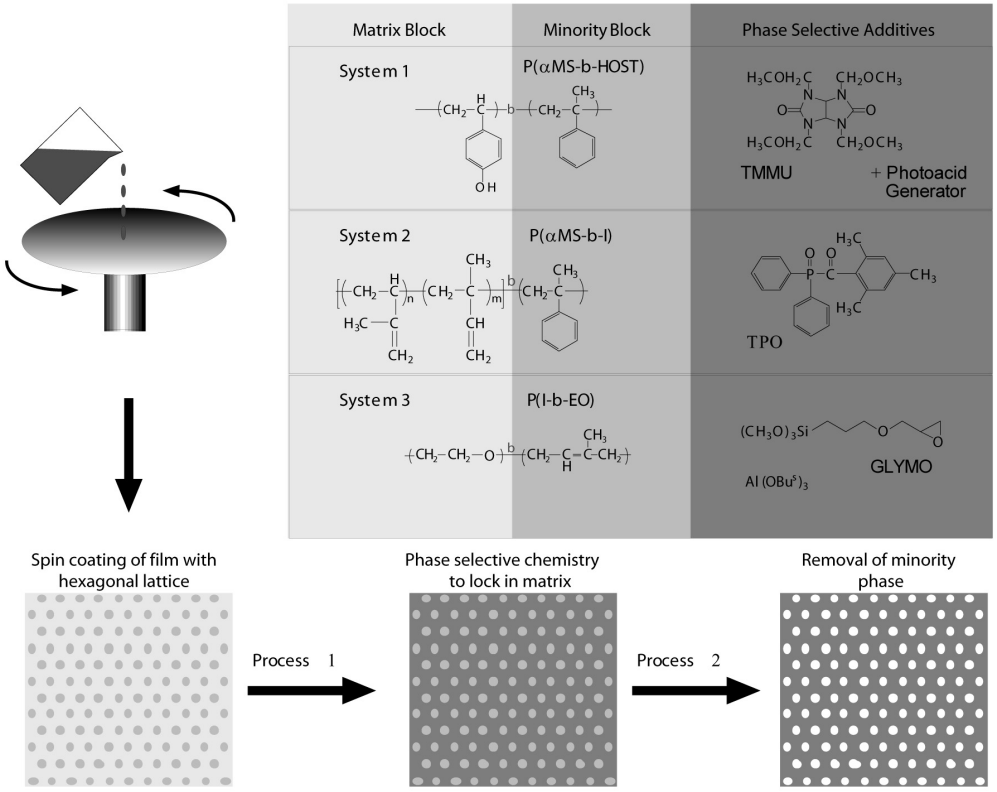

Figure 2.1: The figure shows the three polymer systems examined in this study: (System 1) poly(αmethyl styrene–b–4-hydroxystyrene), P(αMS–b–HOST), contains a 4-hydroxystyrene matrix block which is photocrosslinked with TMMU and photoacid generator; (System 2) poly(αmethyl styrene–b–isoprene), P(αMS–b–I), is photocrosslinked with TPO. Both Systems 1 and 2 have removable α-methyl styrene blocks; in (System 3) poly(isoprene–b–ethylene oxide), P(I–b–EO), the PEO block serves as the site for reaction with GLYMO/Al(OBu)$_3$ and is eventually removed with all other organic components. As shown in the schematic, all systems share processing via spin coating, which ultimately leads to pores penetrating from the top to the bottom of the films, see Figure 2.2. Subsequent processing locks in the matrix and removal of the minority phase leads to porous thin films.

solution onto silicon wafers.

Selection of the appropriate chemistry makes it possible to tailor the role of each block. In the P(αMS–b–HOST) System 1, the 4-hydroxy styrene (HOST) is rendered insoluble by photoacid induced crosslinking with TMMU [11] and the MS block is removed through UV/vacuum treatment. The P(αMS–b–HOST) polymer was combined with both TMMU (4 wt%) and a photoacid generator, triphenylsulfonium trifluoromethyl sulfonate (1.6 wt%) and deposited from solution on a silicon wafer. Exposure to low levels of 248 nm UV radiation ($\sim$10 mJ/cm^2) leads to efficient crosslinking of the HOST phase. UV light triggers the generation of acid by the photoacid generator that in turn catalyzes the reaction of the TMMU with the hydroxy group to crosslink the HOST block. Regardless of the local distribution of the reactants, this chemistry only takes place in the HOST phase. In the case of the P(αMS–b–I) block copolymer (System 2) the isoprene domain is radically crosslinked by the TPO [12] photoradical generator while the αMS block is removed during subsequent UV photolysis. Crosslinking under mild UV exposure ($\sim$100 mJ/cm^2) renders the continuous isoprene phase stable enough that when further UV exposure ($>$300 mJ/cm^2) with vacuum is used to degrade the MS phase, matrix phase collapse does not occur. By the appropriate selection of additive chemistry, the isoprene block can serve as either the retained block as in System 2 or a removable component as in System 3. In the latter, the ethylene oxide microphase of the P(I–b–EO) block copolymer is swollen by the inorganic precursors serving as host for the sol-gel derived aluminosilicate products [13]. Subsequent high temperature oxidation removes all organic components leaving a pure oxide film. Going over from all-organic Systems 1 and 2 to a system with inorganic additives (System 3) opens additional opportunities such as high temperature processing or extended etching capabilities unavailable for all-organic thin films.

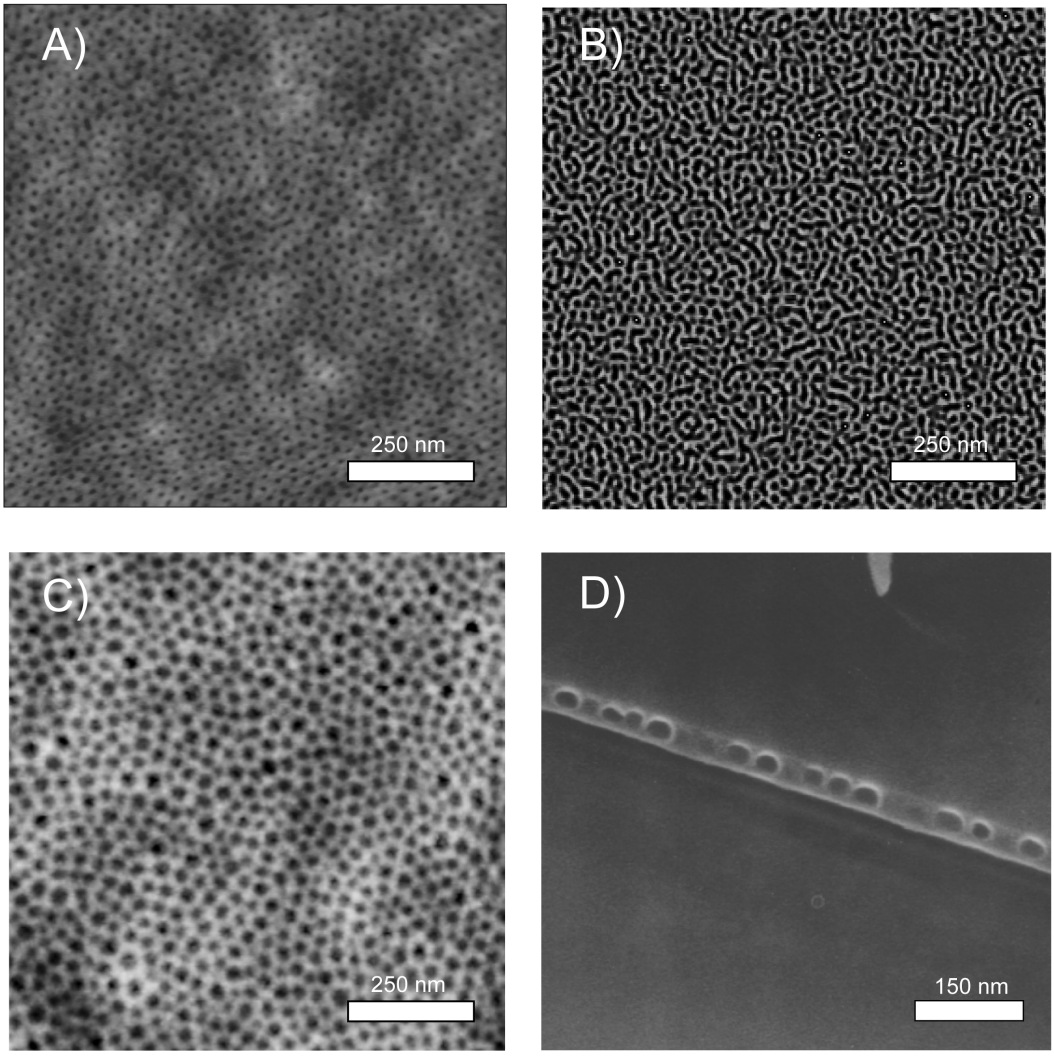

Figure 2.2: AFM height images of porous thin films produced from (A) (System 1) P(αMS–b–HOST), (B) (System 2) P(αMS–b–I) and (C) (System 3) P(I–b–EO). In each system porous structures are produced using phase specific chemistry. The pore dimensions are consistent with the size of the starting film microstructures. (D) A SEM micrograph of System 3 shows the arrangement of the microstructure prior to calcination demonstrating monolayer control.

Figure 2.3: (A) Experimental GISAXS scattering pattern from a monolayer-type calcined film as shown in Figure 2.2. (B) Comparison of experimental (left) and simulated scattering patterns. Q values are in nm^{-1}, with q_x parallel, and q_z perpendicular to the plane of the polymer film. Two scattering object geometries were employed in the simulation, namely cylinders and ellipsoids as indicated below the respective images. Input parameters for the simulations were: pore-pore spacing (34.6 nm), film thickness (14 nm), and aspect ratio (height/radius = 1). These values were consistent with those obtained from the other characterization techniques (AFM and SEM). A Gaussian probability distribution was applied to input parameters to better simulate experimental conditions. X-rays of wavelength λ=0.155 nm incident at 0.2075°to the film surface were used. The scattering objects (representing the pores) were distributed on a regular hexagonal lattice. Application of cumulative disorder, as described in the IsGISAXS simulation package, resulted in a loss of long range order, consistent with AFM data (see Figure 2.2). The IsGISAXS simulation package is available from ESRF [14]

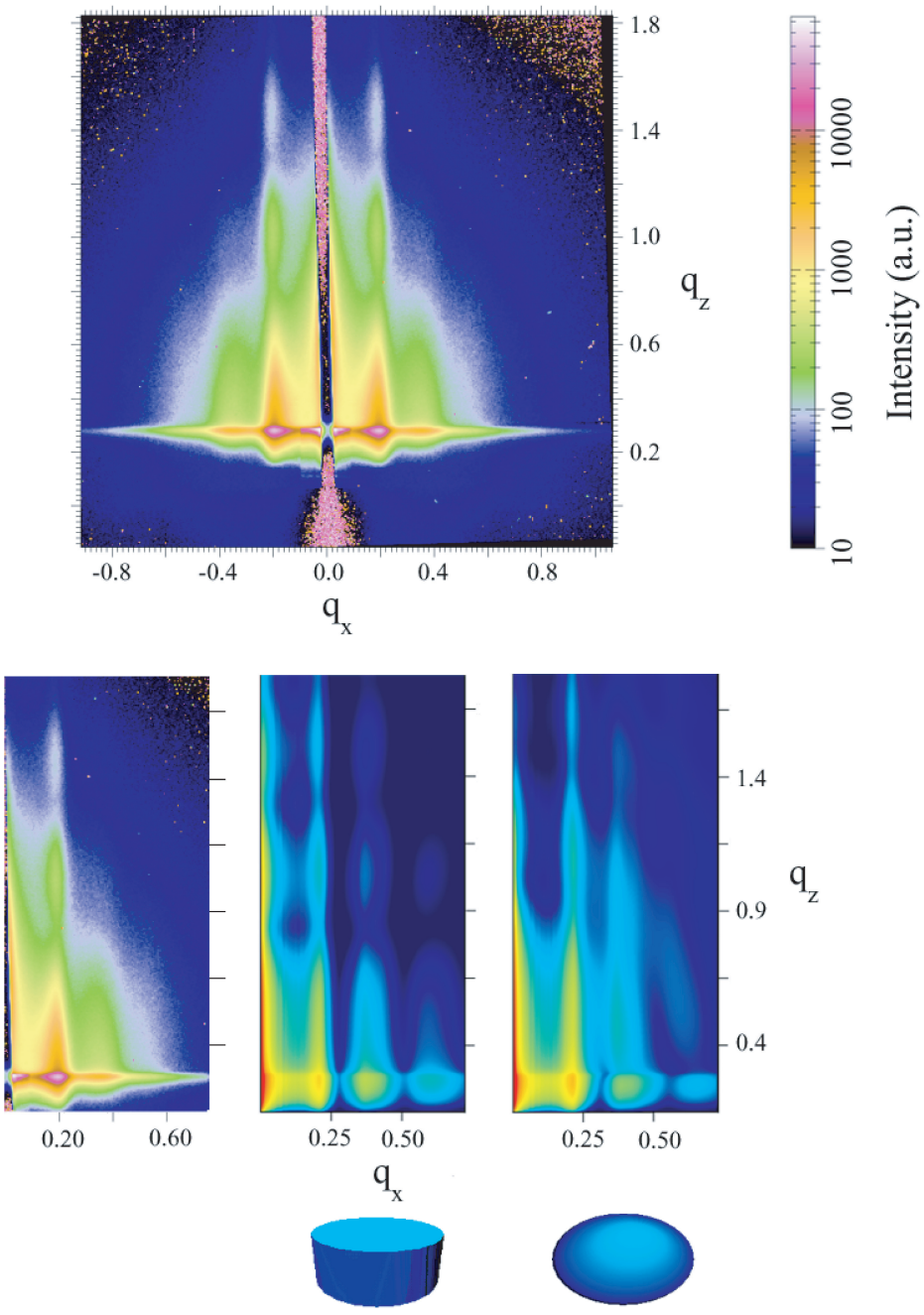
1.8
1.4
1.0
0.6
0.2
q_z
-0.8
-0.4
0.0
0.4
0.8
q_x
10000
1000
100
10
Intensity (a.u.)
1.4
0.9
0.4
q_z
0.20
0.60
0.25
0.50
0.25
0.50
q_x

Thin film morphologies of these three systems as observed by atomic force microscopy after processing is shown in Figure 2.2A, B and C (height mode images). In all cases a hexagonal arrangement of pores can be observed. Please note that while the chemistries in each case are quite different, we were able to achieve similar microstructures without special surface treatment. Although not shown, the arrangement and size of these pores corresponds very well to those of the as made, unprocessed block copolymer thin film microstructures. Figure 2.2D shows a cross-section of the same film depicted in Figure 2.2C, System 3, but before high temperature oxidation. The cross section image shows the monolayer upside down, i.e., the silicon substrate is pointing upwards and the surface revealed in Figure 2.2C is pointing downwards (the hexagonal pore arrangement is thus not visible). Figure 2.2D clearly demonstrates that monolayer control can be achieved in these thin films.

In order to test the thin film structures on macroscopic length scales and to demonstrate that the AFM images of Figure 2.2 are representative, we employed grazing incidence small angle x-ray scattering (GISAXS) [15] on all samples. Measurements were performed at the CHESS D-line featuring a multilayer monochromator and an area detector. Here we will only discuss results of System 3. In Figure 2.3 a GISAXS pattern is shown for the calcined state (after removal of all volatile components). In these experiments lateral correlations within the film plane and structural information along the film normal are documented through scattering intensity in the q_x and q_z directions of the two-dimensional scattering patterns, respectively. As expected the scattering intensity is significant due to strong electron density contrast between the pores and the inorganic phase. Scattering intensity along q_x is observed up to higher orders. In addition the calcined film shows a distinct scattering intensity modulation along the q_z direction. Since the film is a monolayer as evidenced by the SEM image in Figure 2.2D, this modulation

can only be attributed to the form factor of the scattering objects, i.e., the pore geometry.

The 2D GISAXS results were simulated employing the software package IsGISAXS [14]. Simulation results for the calcined film for two different pore geometries, i.e., cylinder and ellipsoid, are shown in the bottom of Figure 2.3. Overall the observed intensity distribution in the 2D plane is very well reproduced. For the ellipsoidal pore structure simulation, curvature towards the main beam reflection occurs, in particular for the higher order peaks. This is not observed in the experimental data. Since the effect is most pronounced for high q-values, additional experiments were performed, in which the low q-range was blocked and data only for the high q-range was acquired. No curvature could be observed in these experiments either. Rather, the results are better represented through the cylindrical pore model for which the intensity distribution along q_z is a straight line, consistent with the data. Pore structure dimensions obtained from all simulations are in good agreement with experimental results from AFM and SEM.

The preceding results show that additive driven phase selective chemistry can be used to create nanostructured thin films. These films are interesting in their own right, but here we would like to go one step further towards an application of this concept that combines this "bottom-up" approach with a lithographic "top-down" approach. This combination enables hierarchical structure formation in thin films from the macro down to the nanoscale. In order to explore the prospects for the use of phase selective chemistry in lithography, the P(αMS–b–HOST) block copolymer was investigated as a photoresist. Random copolymers based on PHOST are the workhorse of the semiconductor industry and are the basis for many chemically amplified, high resolution resists. Figures 2.4A and B show both the chemistry of the lithographic process and an AFM of the surface of the polymer mixture before (A) and after (B) exposure to UV radiation. A comparison of the AFM images in Figure 2.4 shows that the microstructure of the block

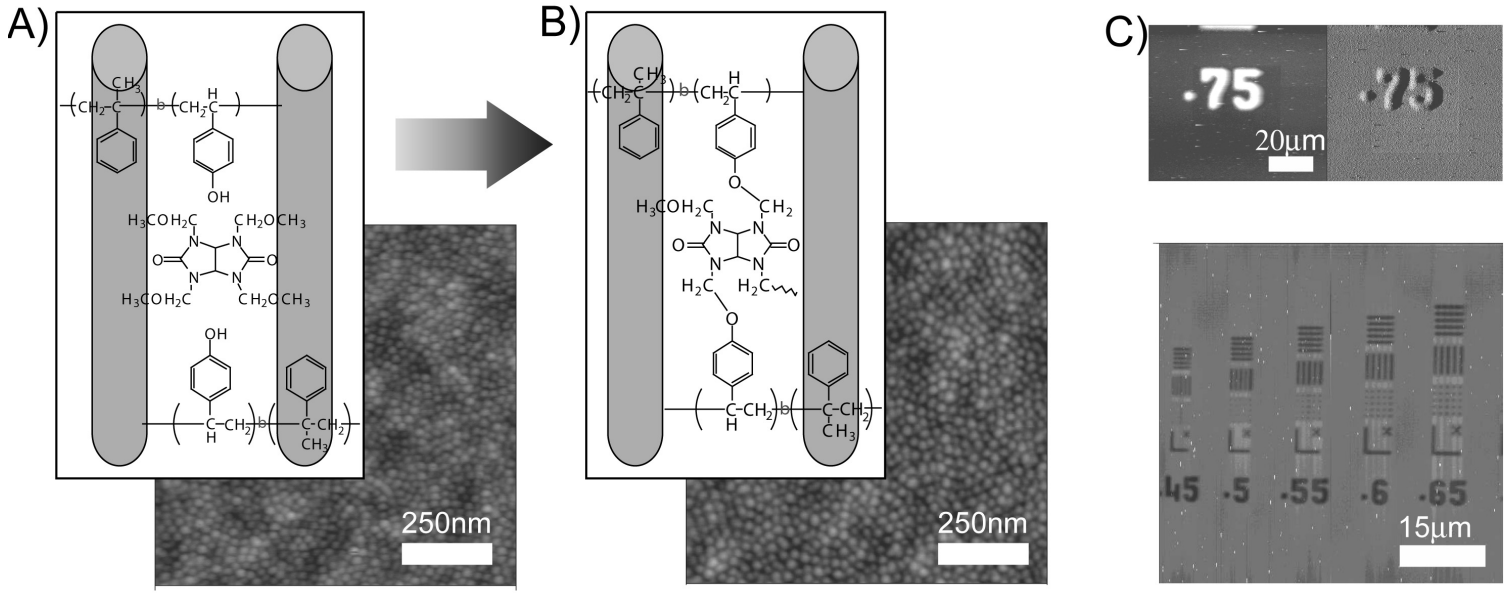

Figure 2.4: The process for patterning the P(αMS-b-HOST) block copolymer involves photochemical crosslinking with TMMU in combination with photoacid generator. Prior to crosslinking (A) the block microstructure shows hexagonal order as revealed by phase contrast AFM. Subsequent to photocrosslinking (B) further AFM studies show the microstructure and its orientation are retained. By development in aqueous base, the unexposed regions can be easily dissolved to form patterned sub-micron images. The upper portion of C shows a test pattern in which pores have been formed during subsequent processing. A more detailed image of a nanoporous film is shown in Figure 2.2. The lower portion of C shows a lithographic image with features as small as 450 nm.

copolymer thin film is not altered by the lithographic process. The same low levels of 248 nm UV radiation that lead to crosslinking of the PHOST phase also permit patterning of this polymer as a very efficient negative resist system as shown in Figure‘2.4C. In the unexposed regions, the PHOST block remains soluble in aqueous base (0.26N TMAH) whereas the exposed region is crosslinked and insoluble. A range of exposure doses and test patterns were examined and Figure 2.4C demonstrates that this polymer system can produce patterns on the order of 400 nm making this material a high resolution resist in its own right. A subsequent, longer exposure to UV radiation in a modest vacuum leads to removal of the PαMS phase with formation of vacant pores that lie within the patterned regions as in Figure 2.2A.

Conclusion

This report demonstrates that the use of additive-driven thin film phase selective chemistry permits direct coupling of a well-established “top-down” lithographic approach to “bottoms-up” self-assembly of block copolymers. These materials are presently being explored as supported porous thin films to separate proteins of selected molecular weight ranges. One can also envisage such materials for template formation for a variety of uses.

Acknowledgments

We gratefully thank Dr. Kathryn W. Guarini and Dr. Charles T. Black for helpful discussions, Dr. Jochen S. Gutmann for simulating discussions about GISAXS data collection and interpretation, and Dr. Ernest Fontes for his help with the CHESS experimental setup and support. The financial support by the Cornell Center for Materials Research

(CCMR), a Materials Research Science and Engineering Center of the National Science Foundation (DMR-0079992), the NSF-funded Cornell NIRT (ECS-0103297-NIRT), the National Science Foundation (Grant DMR-0072009), the IBM Faculty Partnership Program, and JSR Corporation is acknowledged. CHESS is a national user facility supported by NSF/NIH-NIGHM grant DMR-9713424. This work was supported in part by the Nanobiotechnology Center (NBTC), and STC Program of the National Science Foundation under Agreement No. ECS-9876771.

Bibliography

[1] M. Park, C. Harrison, P. M. Chaikin, R. A. Register, and D. H. Adamson. "Block copolymer lithography: Periodic arrays of similar to 10(11) holes in 1 square centimeter" *Science*, **1997**, *276*, 1401-1404.

[2] T. Thurn-Albrecht, R. Steiner, J. DeRouchey, C. M. Stafford, E. Huang, M. Bal, M. Tuominen, C. J. Hawker, and T. P. Russell. "Nanoscopic templates from oriented block copolymer films" *Advanced Materials*, **2000**, *12*, 787-791.

[3] M.A. Hartney, A.E. Novembre, and F.S. Bates. "Block copolymers as bilevel resists" *Journal of Vacuum Science & Technology B (Microelectronics Processing and Phenomena)*, **1985**, *3*, 1346-51.

[4] D. Zhao, P. Yang, N. Melosh, J. Feng, B. F. Chmelka, and G. D. Stucky. "Continuous mesoporous silica films with highly ordered large pore structures" *Advanced Materials*, **1998**, *10*, 1380-+.

[5] V. Z. H. Chan, J. Hoffman, V. Y. Lee, H. Iatrou, A. Avgeropoulos, N. Hadjichristidis, R. D. Miller, and E. L. Thomas. "Ordered bicontinuous nanoporous and nanorelief ceramic films from self assembling polymer precursors" *Science*, **1999**, *286*, 1716-1719.

[6] K. Yu, B. Smarsly, and C. J. Brinker. "Self-assembly and characterization of mesostructured silica films with a 3d arrangement of isolated spherical mesopores" *Advanced Functional Materials*, **2003**, *13*, 47-52.

[7] T. Thurn-Albrecht, J. Schotter, C. A. Kastle, N. Emley, T. Shibauchi, L. Krusin-Elbaum, K. Guarini, C. T. Black, M. T. Tuominen, and T. P. Russell. "Ultrahigh-density nanowire arrays grown in self-assembled diblock copolymer templates" *Science*, **2000**, *290*, 2126-2129.

[8] A. Urbas, R. Sharp, Y. Fink, E. L. Thomas, M. Xenidou, and L. J. Fetters. "Tunable block copolymer/homopolymer photonic crystals" *Advanced Materials*, **2000**, *12*, 812-814.

[9] K. Asakawa, T. Hiraoka, H. Hieda, M. Sakurai, and Y. Kamata. "Nano-patterning for patterned media using block-copolymer" *Journal of Photopolymer Science and Technology*, **2002**, *15*, 465-470.

[10] K. Yurekli, R. Krishnamoorti, M. F. Tse, K. O. Mcelrath, A. H. Tsou, and H. C. Wang. "Structure and dynamics of carbon black-filled elastomers" *Journal of Polymer Science Part B-Polymer Physics*, **2001**, *39*, 256-275.

[11] J. M. Shaw, J. D. Gelorme, N. C. LaBianca, W. E. Conley, and S. J. Holmes. "Negative photoresists for optical lithography" *IBM Journal of Research and Development*, **1997**, *41*, 81-94.

[12] C. Decker, K. Zahouily, D. Decker, T. Nguyen, and T. Viet. "Performance analysis of acylphosphine oxides in photoinitiated polymerization" *Polymer*, **2001**, *42*, 7551-7560.

[13] P. F. W. Simon, R. Ulrich, H. W. Spiess, and U. Wiesner. "Block copolymer-ceramic hybrid materials from organically modified ceramic precursors" *Chemistry of Materials*, **2001**, *13*, 3464-3486.

[14] R. Lazzari. "Isgisaxs: a program for grazing-incidence small-angle x-ray scattering analysis of supported islands" *Journal of Applied Crystallography*, **2002**, 35, 406-421.

[15] D.-M. Smilgies, P. Busch, C M. Papadakis, and D. Posselt*Synchrotron Radiation News*, **2002**, page 35.

CHAPTER 3

BLOCK COPOLYMER DERIVED NANOSTRUCTURED HYBRID ORGANIC-INORGANIC THIN FILMS: COMPLEMENTARY LOCAL AND GLOBAL ORDERING ANALYSIS

Abstract

The fabrication of mesostructured silica-type thin films through the use of poly(isoprene–block–ethylene oxide)(PI–b–PEO) and poly(ethylene propylene–block–ethylene oxide) (PEP–b–PEO) block copolymers as structure directing agents for sol-gel silica precursors was examined through a variety of characterization techniques. Films were generated from block copolymers with varying molecular weights and block fractions, different amounts of inorganic loading, and varied from mono- to multilayer assemblies. Local inspection (micron scale) of sample topography with atomic force microscopy and scanning electron microscopy provide insight into the quality of the mesoporous samples as they evolve through optimization of processing and compositional parameters. A quantitative image analysis package was created to extract relevant statistical data for pore density, nearest neighbor distribution, and angular distribution. Voronoi analysis was employed creating easy-to-read diagrams to identify grain size and defect density and location. Radial and bond orientation distribution analysis was used to differentiate between different regimes of ordering, namely crystalline, hexatic, and liquid-like disorder. Global characterization (centimeter scale) was accomplished with grazing incidence small angle x-ray scattering showing good agreement with local data, such as pore-pore spacing, correlation length, and aspect ratio, thereby confirming AFM and SEM analysis is representative of the entire film.

Introduction

Spurred by recent advances in the fields of microelectronics, biosensors, media storage, and catalytic/separation science [1–5], materials science has developed a keen interest in controlling feature sizes on surfaces in the range of tens to hundreds of nanometers. Block copolymer thin films are one of the more promising routes being examined for this task as they offer ease of processing and phase separation induced structure formation on the nanometer length scale [6, 7]. To further their utility, small molecule-type additives enhance and/or introduce new materials properties, such as mechanical and thermal strength, beyond those found in the parent block copolymer systems [8]. Applications developed from these nanostructured surfaces demand user-controlled precision and accuracy which remains a challenging aspect of these systems [9–15]. Here, we discuss the use of such a block copolymer system with inorganic silica-type sol additives and examine the control over its film characteristics, such as pore-pore spacing, defect density, and grain size.

Poly(isoprene-block-ethylene oxide) is used as a structure directing agent for the inorganic hydrolysis products (sol) of 3-glycidyloxypropyltrimethoxysilane and aluminum-tri-sec-butoxide to form mesostructured silica-type thin films on a silicon substrate via spin coating. The inorganic additives are only soluble within the ethylene oxide block of the copolymer and co-assemble into well-defined morphologies through enthalpic and entropic optimization. This hybrid system has been well-studied in the bulk [5, 16], but beyond proof-of-principle experiments [8, 17], has not yet been systematically explored as a thin film. Thin films were created through the simple process of spin coating (Figure 3.1), for which the creation of good-quality (well-ordered) films is not a trivial development. Some of the very first thin films were very poorly ordered, likely to be caused by a combination of factors including, but not limited to: rapid solvent evaporation, non-

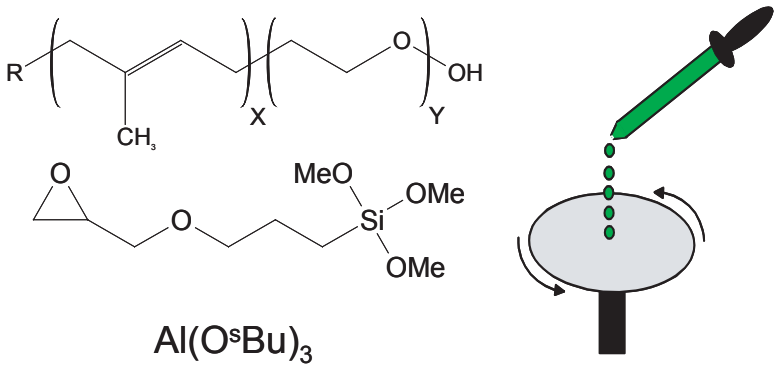

Figure 3.1: Molecular structures of polymer and inorganic additives. Spin coating schematic.

nominal spin coating speed and acceleration, and harsh calcination procedures. We call these factors processing parameters to distinguish them from composition parameters such as neat copolymer block fraction and amount of inorganic loading. There was a very large parameter space to explore, addressed first through processing then through compositional variation. Film characterization and analysis were carried out through a variety of techniques including Atomic Force Microscopy (AFM), Scanning Electron Microscopy (SEM), Grazing Incidence Small-Angle X-ray Scattering (GISAXS), simulations, and statistical methods. Links between spin coating parameters, materials composition, and thermal treatments to the final film quality and characteristics (mentioned above) are demonstrated. Control over these characteristics is an important step toward functional nanostructured materials for applications.

Experimental

Materials

Different poly(isoprene–b–ethylene oxide)(PI–b–PEO) and poly(ethylene propylene-b–ethylene oxide) (PEP–b–PEO) amphiphilic diblock copolymers were synthesized via

Table 3.1: Polymers characteristics

Polymer	M.W.	wt% PEO	λ (nm)	PDI
PEP–b–PEO–A	3640	20	20	1.05
PI–b–PEO–A	16210	12.5	29	1.04
PI–b–PEO–B	31250	18	34	$<$1.1
PI–b–PEO–C	38700	32	37	$<$1.1
PI–b–PEO–D	95550	16	55	1.07

polymerization techniques as described elsewhere [18–20]. Characterization by gel permeation chromatography and ^{1}H nuclear magnetic resonance determined polymer molecular weight, polydispersity, and relative weight fraction (see Table 3.1). Thin films were created by dissolving a specific amount of the diblock copolymer in equal weight tetrahydrofuran and chloroform and then adding 3-6x (by weight) prehydrolyzed sol-gel precursors (aluminum-tri-sec-butoxide and 3-glycidyloxypropyltrimethoxysilane). At this stage silica-type nanoparticles are mixed with the block copolymer. For a detailed description off the co-assembly mechanisms the interested reader is referred to an earlier publication [21]. Concentrations of 0.7 wt% and 3.5 wt% were used for monolayer and multilayer films, respectively. Spin coating was done on silicon wafers by pipetting the hybrid solution onto the substrate then starting the spin cycle. Samples were accelerated ca. 250-5000 RPM/s up to final speeds of 1000-5000 RPM for a total of one minute. Treatment for one hour in a vacuum oven at 130 °C fully condensed the sol-gel and removed any residual solvents. Calcination was carried out in a box furnace (to 500 °C at 5 °C min^{-1}, soak time = 1 hour) to remove the organics and sinter the inorganic components leaving behind a ceramic aluminosilicate film. Inorganic precursors and solvents

were used as purchased from Alrich. Silicon wafers were used as purchased from the Cornell Nanofabrication Facility.

Characterization techniques

Atomic force microscopy data was obtained using a Veeco Nanoscope III Multi-Mode Scanning Probe Microscope operated in tapping mode with TappingMode Etched Silicon probes (resonant frequency = 325 kHz, force constant 37 Nm^{-1}, tip radius of curvature = 10nm; all values nominal) under ambient conditions. Scanning electron microscopy data was obtained using a Hitachi S4500 Field Emission Scanning Electron Microscope with an acceleration voltage of 5 kV and working distance of 10 mm. Grazing incidence small angle x-ray scattering data was collected with a 2D area detector (X-ray energy: 8 keV, sample-to-detector distance: 106 cm, angle: $\sim 0.2^{\circ}$, exposure time: 1-10s) at the Cornell High Energy Synchrotron Source (CHESS).

Image analysis package

A program in the Interactive Data Language (IDL) was coded to read AFM data for further analysis. The program segments an AFM image of porous films into individual regions through a simple watershed function [22] (i.e. identified individual pores). The pore centers are then determined through a weighted average of the lower 10% of each pore. The set of centers is then subjected to a Delaunay triangulation [23] algorithm to determine their nearest neighbors. The algorithm constructs triangles between all center points, only keeping those with a circumscribing circle (the circle containing the vertices) that do not contain another center point. Figure 3.2a shows an AFM close up scan within the IDL program. Figure 3.2b shows examples of a successful triangulation for points 012 and a rejection for points 017 due to the containment of other points

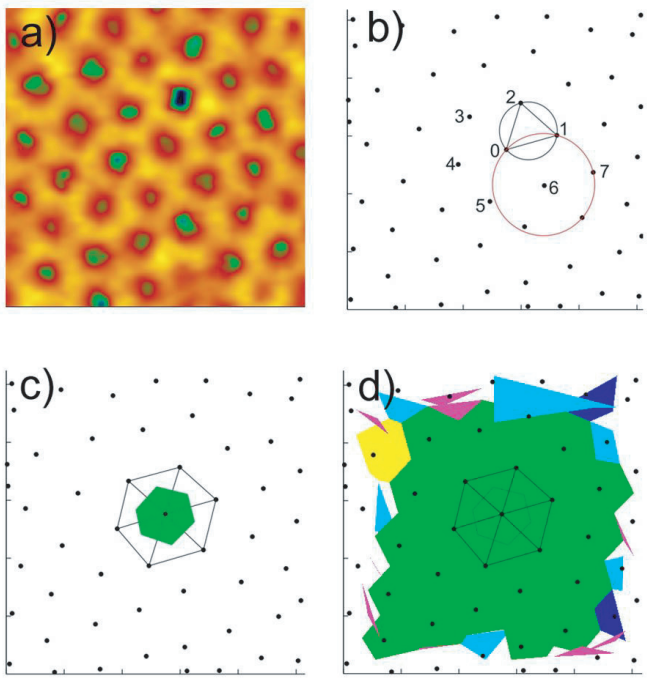

Figure 3.2: IDL analysis of a) bard AFM image. b) Delaunay triangulation of point 0. c) nearest neighbors and Voronoi polygon of point 0. d) Tessellation of entire image

within the red circumscribing circle. Figure 3.2c shows the complete triangulation for center point 0, represented by the black triangles. The algorithm runs on the set until all center points are connected. This triangulation serves as the starting point for further analysis.

From the Delaunay triangulation, perpendicular bisectors can be calculated and the area enclosed by their intersection is defined as a Voronoi polygon [23, 24]. Figure 3.2c shows a complete Voronoi polygon for center point 0. Each point within a Voronoi polygon is closer to the parent center than any other center. In a sense, a Voronoi polygon defines a center point's neighborhood, and is color-coded according to its number of sides (*i.e.* its number of nearest neighbors). Tessellation of a bare AFM image with Voronoi polygons generates an easy-to-read Voronoi diagram to help determine grain

Table 3.2: Film Statistics

Film	Number of centers	Voronoi-6 ratio	FWHM
Bh1a	796	0.34	40.5°
Bh1b	1655	0.49	27.2°
Bh1c	2306	0.53	27.6°
Ch1a	3527	0.67	22.2°
Ch2a	3435	0.74	21.5°
Ch2b	3413	0.54	29.9°

size, defect location, and film ordering. Figure 3.2d is an example of complete coverage of the original AFM image with Voronoi polygons. Note that points near the boundaries of the image are rejected for Voronoi construction to minimize artifacts introduced by the edges. Grains are composed of areas containing center points with six-fold coordination, while defects contain fewer/more neighbors.

Also from the Delaunay triangulation, angular measurements can be made between nearest neighbors. The vectors connecting center point to nearest neighbors can be substituted into a simple dot product equation:

$$\vec{A} \cdot \vec{B} = |\vec{A}||\vec{B}| \cos\theta \tag{3.1}$$

to extract their angular relationship. The ideal hexagonal ordering of the film should produce an angular distribution centered at 60°that narrows with better ordering. Fitting of the experimental data to a Gaussian distribution and extracting the standard deviation (σ) yields the full-width-at-half-maximum (FWHM, Γ) according to the relation: $\Gamma = 2.345 * \sigma$. Data for all films are tabulated in Table 3.2.

Radial and bond orientation distribution function analysis.

The positional order of thin films can be analyzed by calculating the radial distribution function (RDF) through the simple relation:

$$g(r) = \sum_i \sum_{i \neq j} \delta(r - r_{ij}) \tag{3.2}$$

The RDF contains the probability of finding a particle at distance r from another particle at the origin. Decay analysis of the RDF envelope will determine the type of positional order. Algebraic and exponential decay represent quasi-long range and short range positional order, respectively. The RDF alone is only sufficient to distinguish the crystalline from the liquid-like or hexatic states (see Results and discussion section). Help comes from the bond orientation distribution function. The orientational order parameter is defined as:

$$\Psi_6(r) = \sum_i^m exp(6i\theta_{ij}) \tag{3.3}$$

where θ_{ij} is the angle between the bond connecting center i with nearest neighbor j and an arbitrary fixed reference axis (the x-axis for simplicity), and m is the total number of nearest neighbors of i. The bond orientational distribution function (BODF) is then calculated as:

$$g_6(r) \equiv \langle \Psi_6^*(0)\Psi_6(r) \rangle / g(r) \tag{3.4}$$

The BODF is a bit less intuitive than the RDF. Although similar to the RDF, containing the probability of finding a particle at distance r, it is modified by the product of the angles associated with the nearest neighbors. Computationally, the nearest neighbors list is approximated by applying a cutoff radius r_c, where only neighbors at distance $r < r_c$ are included in the calculation. This cutoff radius is easily extracted from the first minimum of the RDF. Decay analysis of the BODF envelope will determine the type of

bond orientation order. Algebraic and exponential decay represent quasi-long range and short range bond orientation order, respectively.

GISAXS simulations

GISAXS simulations were computed with the IsGISAXS program available online [25]. Thin film characteristics such as pore-pore spacing, pore radius, film thickness, and domain size were extracted from AFM and cross-section SEM data and used as initial values for the simulation. X-ray energies and incident angles were taken from the experimental GISAXS setup (see above). A monolayer of different shapes (cylinders and ellipsoids) were distributed onto a variably distorted lattice and simulated GISAXS patterns were obtained using the Distorted Wave Born Approximation.

Results and discussion

Local characterization

Overview

Figure 3.3 shows some typical hybrid thin films obtained from the PI–b–PEO-B block copolymer with the Bh1 composition, see Tables 3.1 and 3.3. Both single and multilayer films can be visualized through cross-section SEM both in the as-made and calcined states (Figures 3.3a and c and Figure 3.3b and d, respectively). Combined with AFM topography data (Figure 3.3e), these images suggest that the as-made internal structure of PI spheres ordered within a matrix of PEO/aluminosilicate is reduced to empty circular pores within a completely inorganic matrix after calcination. The significant volume change associated with the calcination process is mainly expressed as a decrease in the film thickness with minimal changes to any lateral dimensions. This

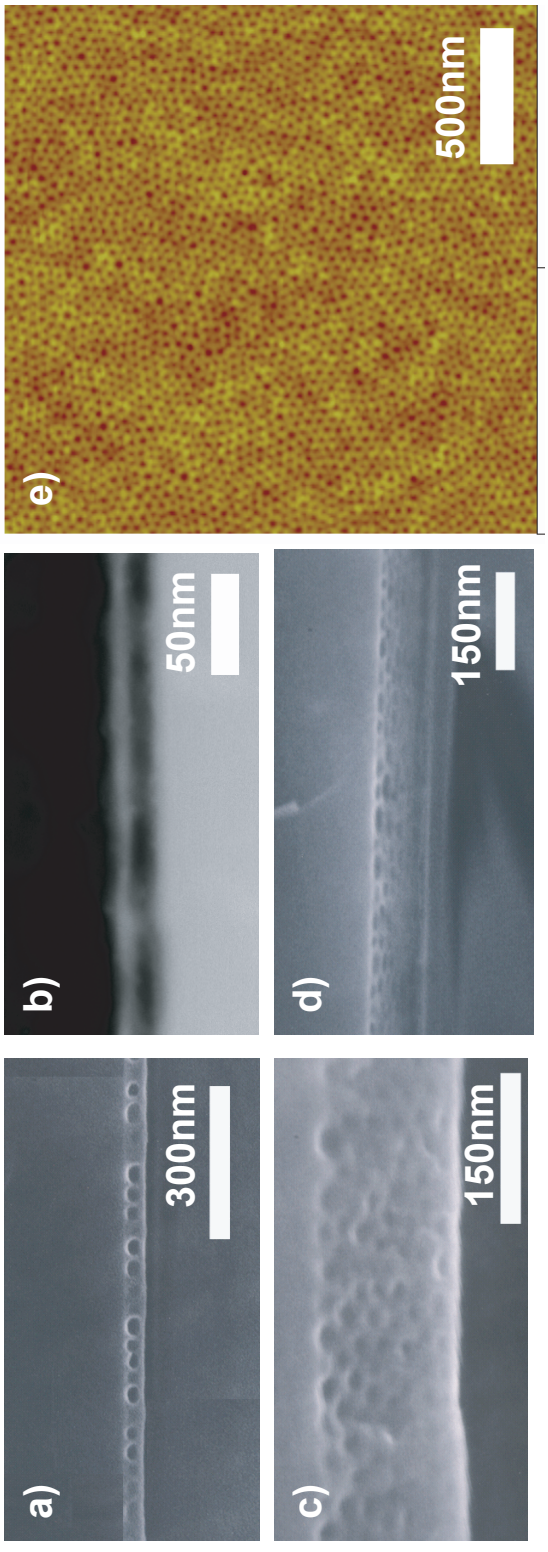

Figure 3.3: Cross section SEM images of as-made a) monolayer and c) multilayer films. Respective calcined films are shown in b) and d). Plane view AFM image of calcined monolayer film.

Table 3.3: Hybrid samples characteristics

Sample	wt% PEO + inorganic
PI–b–PEO-Bh1	74.4
PI–b–PEO-Ch1	78.7
PI–b–PEO-Ah1	80.0
PI–b–PEO-Ch2	84.1
PEP–b–PEO-Ah1	81.4
PI–b–PEO-Dh1	82.4

anisotropic shrinkage greatly affects the shape of the pores in the calcined films and has important ramifications on x-ray scattering from these samples.

In the following we will look at a series of thin films structured directed by various PI–b–PEO block copolymers under varying processing conditions (see Figures 3.4 and 3.5). From a qualitative standpoint, the general improvements seen in the series of AFM images (Figures 3.4, 3.5, Row 1) are evident: pore size dispersity and hexagonal ordering improve significantly. Improvements between the films in Figures 3.4a and b are easy to distinguish, while films in Figures 3.4c and 3.5a and b look very similar. To characterize differences in their order, quantitative analysis tools are necessary.

To this end we applied an IDL program (see Experimental Section) to the AFM data. Results of this analysis are displayed in Figures 3.4 and 3.5, Rows 2 and 3. Moving from left to right across Figure 3.4 and 3.5, Row 2 Voronoi diagrams, we see that there is an increase in grain size accompanied with a decrease in defect density. It is also obvious from Figure 3.4 and 3.5, Row 3 that there are significant improvements in the angular distribution. Although these general improvements are obvious, there are more subtle changes that only become clear with more careful analysis. Analysis of nearest

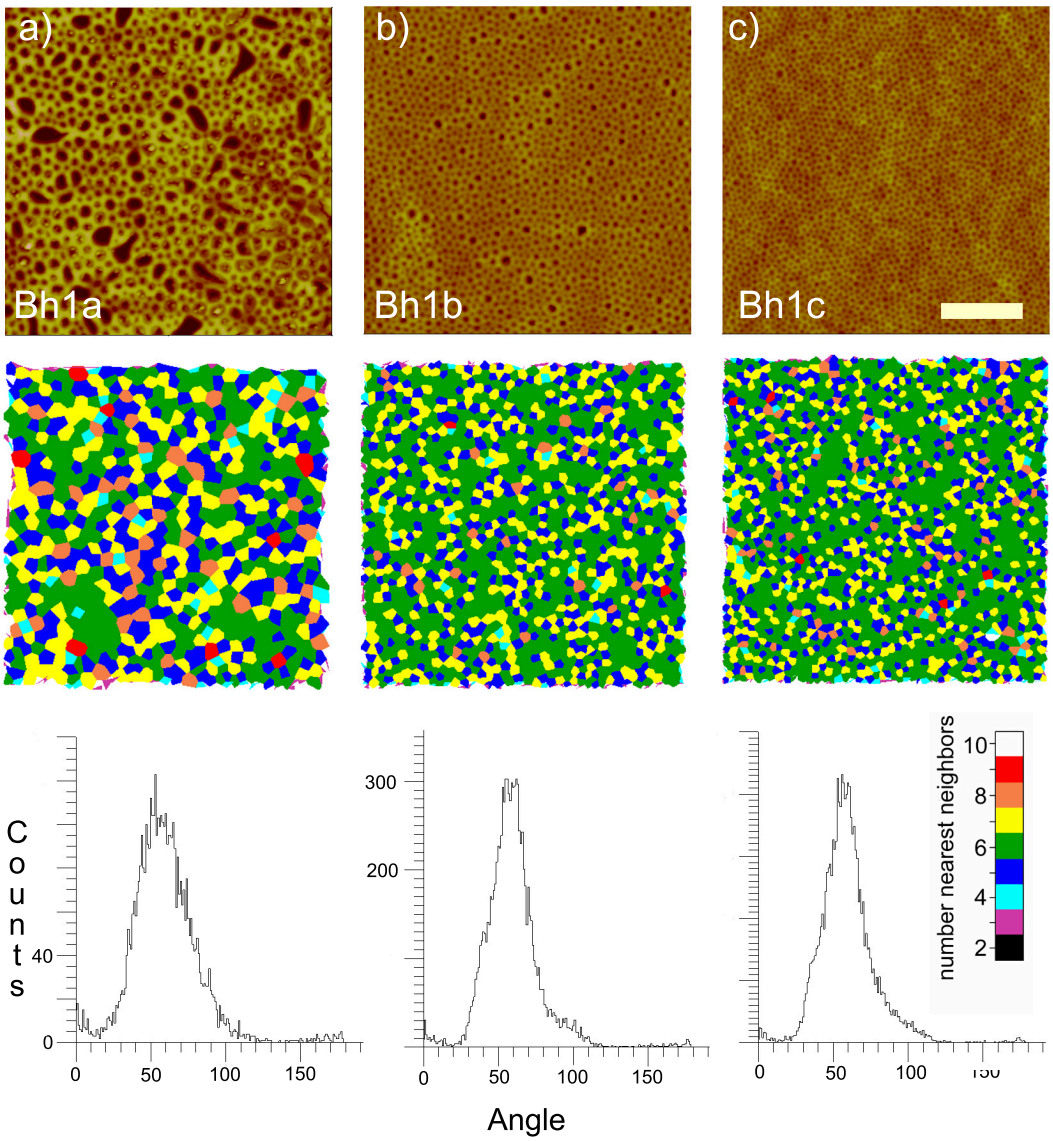

Figure 3.4: Processing parameter optimization. (Row1) AFM images of calcined thin films were analyzed with the IDL program to create easy to read (Row 2) Voronoi diagrams and (Row 3) bond angle distribution. From left to right, the series of images depict improvements in film quality through optimization of processing parameters such as spin coating speed/acceleration and thermal treatment to remove the organic components. Scale bar = 500nm

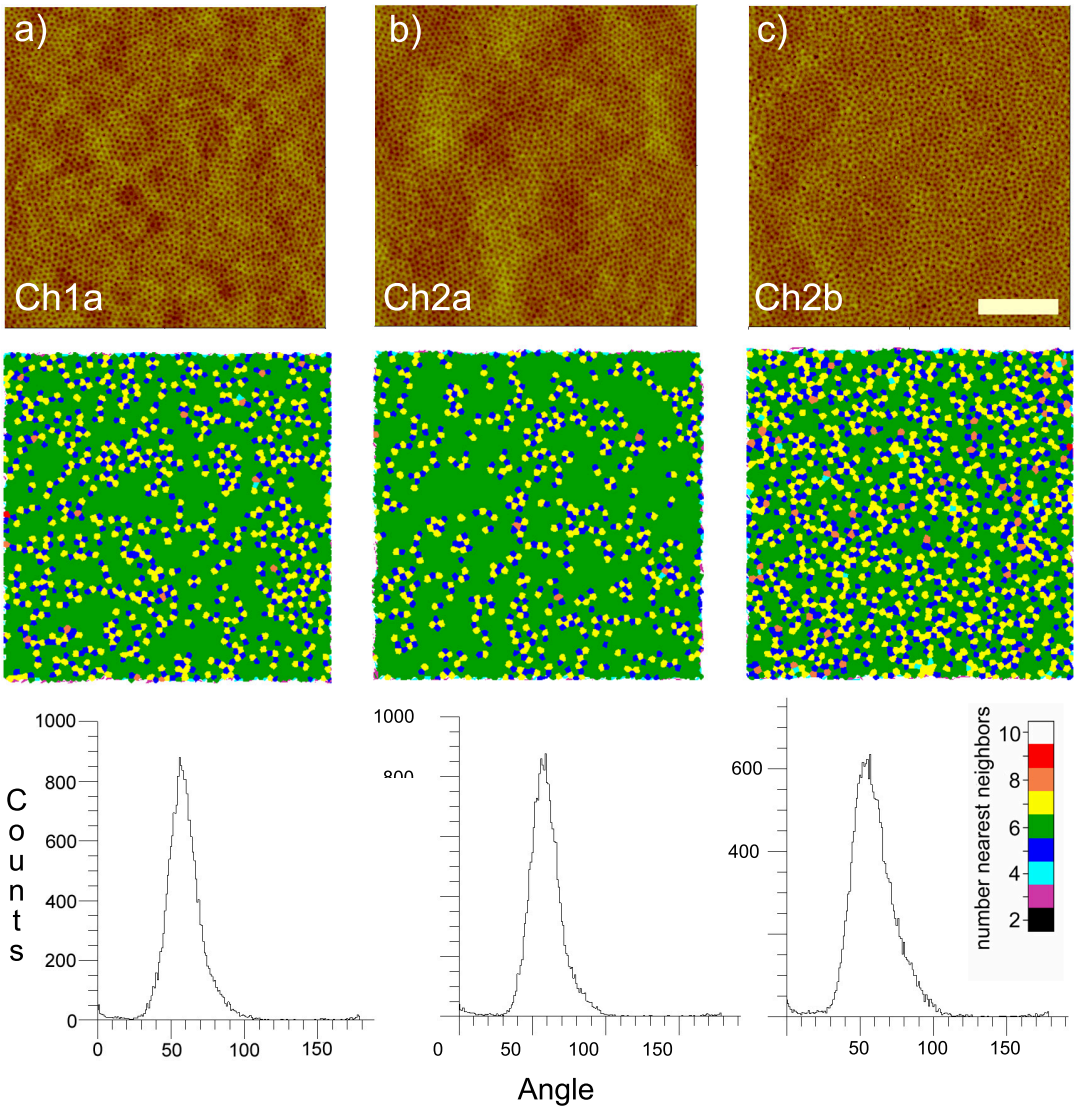

Figure 3.5: Composition parameter optimization. (Row1) AFM images of calcined thin films were analyzed with the IDL program to create easy to read Voronoi diagrams (Row 2) and bond angle distribution (Row 3). From left to right, the series of images depict improvements in film quality through optimization of composition parameters such as amount of inorganic loading and neat copolymer weight fraction. c) monolayer assembly of same composition as b). Scale bar = 500nm

neighbor histograms (see Table 3.2 for results) provides additional insights into film optimization details. There is an overall increase in the number of centers within a fixed image size (2μm) of over 300%, which can be attributed to a combination of factors (to be discussed). Another significant value is the Voronoi-6 ratio which we define here as the number of six nearest neighbor centers divided by total centers. The films start with a minority Voronoi-6 contribution of 1/3 and improve to a nearly 3/4 majority, see Table 3.2. Lastly, the angular distribution of nearest neighbors decrease significantly by nearly 50%. The improved numbers between these thin films are attributed to different mechanisms that fall into the two categories previously described: processing and composition.

Processing

All the films in Figure 3.4 were created with the hybrid composition PI–b–PEO-Bh1 from a 3.5 wt% solution. (see Table 3.3). The only variables that were changed for this series were the processing parameters. The large initial jumps (100% number increase, 44% Voronoi-6 ratio increase, Figure 3.4a to 3.4b) are mainly due to improvements in the thermal processing for organic removal from the films. Early processing involved heating the sample up to 500 °C on a ceramic heater in a very short time span (c.a. 5 minutes). This rapid decomposition, and expulsion, of the polymeric components distorts the original state of the film (sample Bh1a, Figure 3.4a). More careful organic removal perturbs the matrix to a lesser degree and leaves a mesoporous film closer to its initial starting state (sample Bh1b, Figure 3.4b). This was achieved through calcination in a box furnace up to 500 °C but at the slower rate of 5 °C per minute.

Further improvements in film structure control were achieved through optimization of spin casting parameters and materials composition. Moving from AFM image in

Figure 3.4b to that in 3.4c reveals a refinement in the pore size distribution. Changes to the acceleration and spin speed contributed to the obvious changes between the two samples. Early samples (sample Bh1b, Figure 3.4b) were fabricated by adding the polymer/inorganic solution to the silicon wafer *after* it was brought up to its final spin velocity (5000 RPM), resulting in a very large acceleration rate. The solution experiences large changes in force upon contact with the wafer and this is the likely source of disorder in the final film. To minimized this source of disorder, the sequence was changed such that the solution was added to the substrate *before* the start of the spin cycle (velocity = 5000 RPM, acceleration = 500 RPM/s). Further optimization was obtained through reduction of the final velocity to 2000 RPM at an acceleration rate of 250 RPM/s for better ordering (sample Bh1c, Figure 3.4c). In the AFM image in Figure 3.4c, there are much fewer anomalous large-sized pores, a smaller mean pore diameter, and its Voronoi diagram consists of finer polygons. The fact that the increase in number of centers is accompanied by very small changes in the Voronoi-6 ratio and the Γ value is a strong indicator that size refinement is occurring without changing the angular relationship between pores.

Composition

Further improvements in film quality were becoming more difficult to accomplish through optimization of spin coating parameters and thermal calcination conditions. We therefore next explored how composition affects the quality of the film. Thin films shown in Figure 3.5 were made from PI–b–PEO-C whose molecular weight and PEO fraction are slightly larger than those of PI–b–PEO-B (see Table 3.1). Initial films from this new copolymer were tuned to match the composition of films Bh1 (Figure 3.4) to insure reproducibility across different neat polymer compositions. However, it is already

obvious from the AFM image that there are improvements in film characteristics with the slight 4.3% increase of the PEO+inorganic weight fraction compared to films Bh1 (see Table 3.3). Film Ch1a shows improvements across all values. The pore number and Voronoi-6 ratio increase by 53% and 26%, respectively, while the FWHM decreases by 20% from film Bh1c. Taking cue from the improved numbers associated with the larger PEO+inorganic content, films with an even larger inorganic weight fraction (84.1%) were fabricated. The resulting film Ch2a shows slightly improved numbers over film Ch1a (10% Voronoi-6 increase, minimal changes for centers and FWHM). While differences in the bare AFM images are difficult to discern, Voronoi analysis of these two films shows that the slight increase in the Voronoi-6 ratio has a rather strong impact on the film order, namely generating larger grains with a smaller defect density. Thus, the increases in the Voronoi-6 ratio combined with the decreases in FWHM over the B1 samples result in much better ordered films, sometimes made obvious only through Voronoi analysis.

Monolayer films

The previously optimized spin coating parameters applied to a more dilute 0.7 wt% polymer/inorganic solution generated single layer (monolayer-type) films as shown on sample Ch2b in Figure 3.5c. This film is of the same composition as film Ch2a, differing only in its thickness. The AFM image and Voronoi analysis look quite different from those of film Ch2a, however, and are rather similar to film Bh1c. This departure from the general trend of improved order with increasing inorganic loading can be attributed to material-substrate and material-air interfaces. The substrate-film and film-air interfaces are much more dominant in monolayer films as compared to multilayer samples. The substrate can pin down defects in the film preventing the formation of large grains in

monolayer samples. Multilayer samples suffer from this influence to a lesser degree because they can heal these defects due to the nature of their structure. Although defects in the layer nearest to the substrate are pinned, subsequent overlayers may freely move around to eliminate these defects [26]. Since these defects are high energy, the film would naturally strive to eliminate them through rearrangement of the aluminosilicate matrix.

RDF and BODF analysis

AFM images, pore statistics, and Voronoi analysis provide valuable insight into how film ordering is improving in response to changes in processing and composition parameters. Although these methods already help distinguish film order more quantitatively, it is desirable to further analyze whether they fall under any of the three regimes associated with two dimensional ordering: crystalline, hexatic, and liquid-like disorder [27–29]. These regimes are characterized according to the behavior of two parameters: the positional order and bond orientation order [30, 31]. Crystalline materials possess quasi-long range positional order and long range bond orientation order, while liquid-like disordered materials possess both short range positional and bond orientation order. A new phase during the transition from crystalline to liquid-like disorder, known as the hexatic phase, is characterized by short-range positional order but a quasi-long range bond orientation order.

By analyzing the Voronoi diagrams of a material, some qualitative statements can be made about the ordering regimes. Crystalline ordering is characterized by a nearest neighbor distribution that strongly favors 6-fold coordination, while liquid-like disorder displays a more uniform distribution. Again, hexatic ordering would posses a mixture between these two states. From the Voronoi diagrams and pore statistics, it is clear

that the samples evolve from a liquid-like to a more crystalline state. The first Voronoi diagram (Figure 3.4a, Row 2) exhibits a uniform distribution of n-nearest neighbors, showing no bias toward 6-fold coordination (colored green). Improvements led to the Voronoi diagram in Figure 3.5b showing not only a strong 6-fold coordination but also a significant decrease in the number of higher order defects, i.e. $>$7-fold or $<$5-fold, (non-blue and non-yellow). It is important to note that the absolute size of Voronoi grains can be deceiving, as similar sized green grains in latter films are composed of many more individual pores due to size refinement. Stringent criteria are required to make a quantitative determination of the ordering behavior of these samples.

Combining both the RDF and BODF analyses (discussed in the Experimental Section), enables a clear order determination. Figure 3.6 is a compilation of the RDFs and BODFs of the thin films from Figures 3.4 and 3.5. Functions are vertically displaced for clarity. The Bh1a radial distribution function shows very little structure, even lacking a clear primary peak, due to the large distribution of pore sizes and the general disorder of the film. Subsequent RDFs improve dramatically starting with the appearance of a well-defined characteristic pore spacing (in Bh1b) to the growth of additional higher order peaks (in Ch2a). The peaks that persist for many higher orders are a direct result of larger grains. Also, as the primary peak grows larger and narrower, it shifts toward smaller r values, representing the shift to a shorter characteristic length, an increase in

Table 3.4: Ordering summary

ordering regime	RDF	BODF
crystalline	algebraic decay	constant
hexatic	exponential decay	algebraic decay
liquid-like disorder	exponential decay	exponential decay

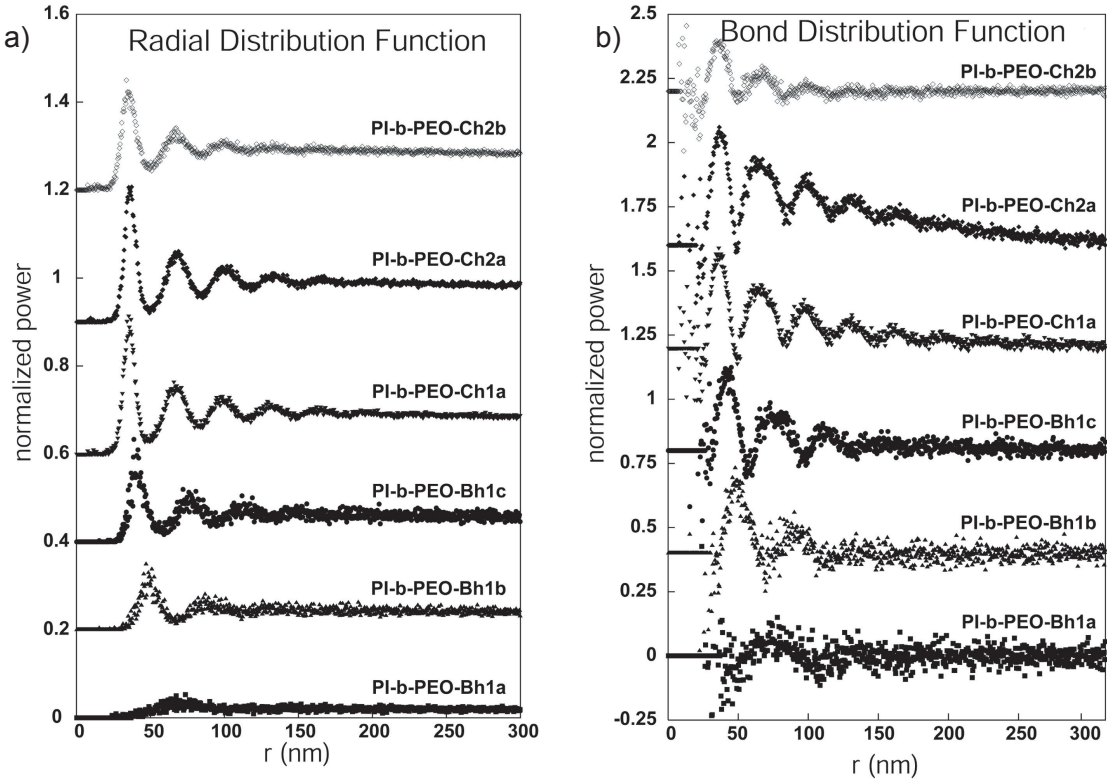

Figure 3.6: a) Radial and b) bond orientation distribution functions. These functions help determine the ordering regime of the films shown in Figures 3.4 and 3.5.

pore numbers, and the refinement of pore size.

Ideally, envelope fitting of the RDF and BODF would help determine the nature of the decay but in the present case, even the better ordered films have up to only five well defined maxima thus limiting the available data points for good quality fits and proper quantitative analysis. However, qualitative statements about the improvements in order from the strongly liquid-like to the nearly hexatic state can be made and do offer insight into the development of the thin films. The RDF decay of all films occur rapidly, corresponding to an exponential decrease, as to be expected from the Voronoi diagrams. With each film iteration, the decay becomes lees severe due to the appearance of higher *r* value peaks, but it never becomes algebraic. This suggests that the ordering regime then has to be either liquid-like or hexatic in nature [30]. The BODFs also display the

rapid decrease associated with exponential decay, which also becomes less severe with each film iteration. Sample Ch2 especially, with its gentle sloping, suggests a transition over to the algebraic decay (*i.e.* hexatic state).

A possible simple explanation for the persistence of this relative disorder in the present thin films is the kinetics of the film/structure formation with contributions from the crosslinking of the inorganic components and the mobility of the macromolecules. Both of these processes are strongly temperature dependent. Increasing the fabrication temperature, commonly used in all-organic systems, thus providing greater polymer mobility to anneal away defects, also speeds up the crosslinking rate and thus determine how fast the thin film sets permanently. These two competing mechanisms in the present block copolymer/silica-type hybrid thin films make it challenging to optimize thin film ordering toward large scale, defect-free structures.

Global Analysis

GISAXS

Analysis of AFM data provides a thorough picture of the ordering of the thin films on the local scale. Although images captured at different areas of these films show similar results in terms of pore numbers, spacing, and orientational correlation, we also explored x-ray scattering techniques to obtain a more complete characterization over larger length scales. Traditional transmission small angle x-ray scattering is insufficient to investigate these thin film samples due to a small scattering volume resulting in insufficient signal. A modified method known as grazing incidence small angle x-ray scattering [32, 33] (GISAXS) is a surface sensitive technique that takes advantage of the total external reflection phenomenon associated with x-ray photons. For x-rays, a solid material is optically less dense than air, thus total reflection is achieved when the

incident angle is less than a materials-dependent critical angle (*i.e.* when Snell's Law can no longer be satisfied with real angles). Under these conditions, the reflectivity is nearly at unity and the x-ray penetration depth can be controlled by varying the incident angle, thus determining how deep we probe into the film. Any variations in the electron density of the film will result in off-specular scattering that can be collected and analyzed. The grazing angles ($<0.5°$) of this setup result in a large footprint (c.a. 1-2 cm) providing a more accurate representation of the film across macroscopic dimensions and insuring significant scattering from a nanoscale thick film. Scattering experiments were performed on both mono- and multilayer samples, but only results for the former will be discussed. Proof-of-principle experiments have already been described in a previous publication [8]. Here a full account of the results will be presented.

Figure 3.7a is a scattering pattern of an as-made monolayer film obtained from a sample with identical composition and processing condition as the sample characterized by AFM in Figure 3.5c. A vertical beam stop blocks the main beam and its strong specular reflection. Scattering intensity in the q_x and q_z provides information about the film in the lateral and normal directions, respectively. The first order peak is clearly visible and supports the AFM data of a well-defined nearest neighbor correlation. Figure 3.7b is a scattering pattern from a calcined monolayer film. Calcination of an as-made film not only removes the organic components, but also sinters and densifies the inorganic network. This significantly increases the electron density contrast and sharpens the interface in the calcined films, moving from a polymer/inorganic-polymer to an inorganic-air interface, and results in a richer scattering pattern. A significant increase in the scattering intensity is also accompanied by the appearance of additional features not visible in the as-made diffractogram. There are now two very prominent diffraction peaks, and a developing third, in the scattering intensity along the q_x direction. Diffractograms

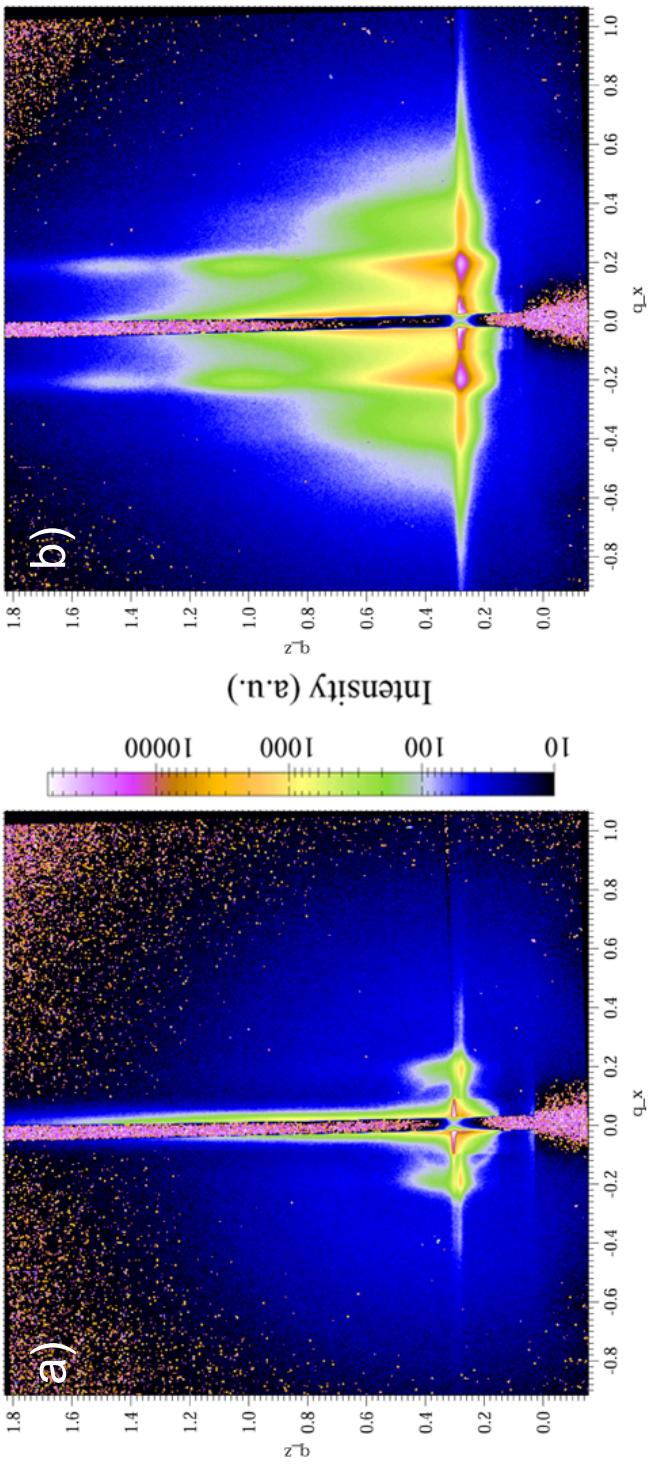

Figure 3.7: GISAXS diffractograms from monolayer films in the a) as-made state, and b) calcined state. Units are in nm^{-1}.

collected for longer times with blockage of the low q values display even higher order scattering (data not shown). This is a direct result of the sharpened interface together with good order and is in qualitative agreement with the decay analysis of the AFM data (see Figure 3.6) and suggests that local data taken with AFM may be a sufficient representation of the film as a whole. The first diffraction rod also displays an interesting intensity modulation in the q_z direction (Figure 3.7b). Three distinct peaks can be distinguished within the first order rod, with more continuing beyond the detector. Since this sample is sufficiently thin to contain only one layer of pores, this effect cannot be a constructive phenomenon associated with scattering from multiple layers. It must then be solely the form factor of the scattering object that is responsible for generating these modulations.

Recall that as-made films, both mono- and multilayer, are composed of polymeric spheres hexagonally packed within an inorganic network (Figures 3.3a and c). Calcination of the film causes shrinkage mainly in the direction normal to the substrate. Good adhesion between the film and substrate, and between subsequent layers, limits shrinkage in the lateral direction [34]. The images of calcined films, especially Figure 3.3d, depict a very pronounced contraction in the film normal direction resulting in "barrel" shaped objects. Furthermore, analysis of the as-made and calcined GISAXS scattering patterns shows no discernible shift of the first order peak. Simulations were generated (IsGISAXS) [35] with parameters such as pore-pore spacing and correlation length extracted from AFM data. Variables such as scattering object geometry (i.e. form factor) and film thickness were varied to obtain the best fit to the experimental diffractogram (Figure 3.8a). Simulated scattering diffractograms from cylinders (straight-walled) and ellipsoids (curved-walled) (Figures 3.8d and e, respectively) are very distinct but do share some characteristics, as expected, associated with lateral correlations such as the

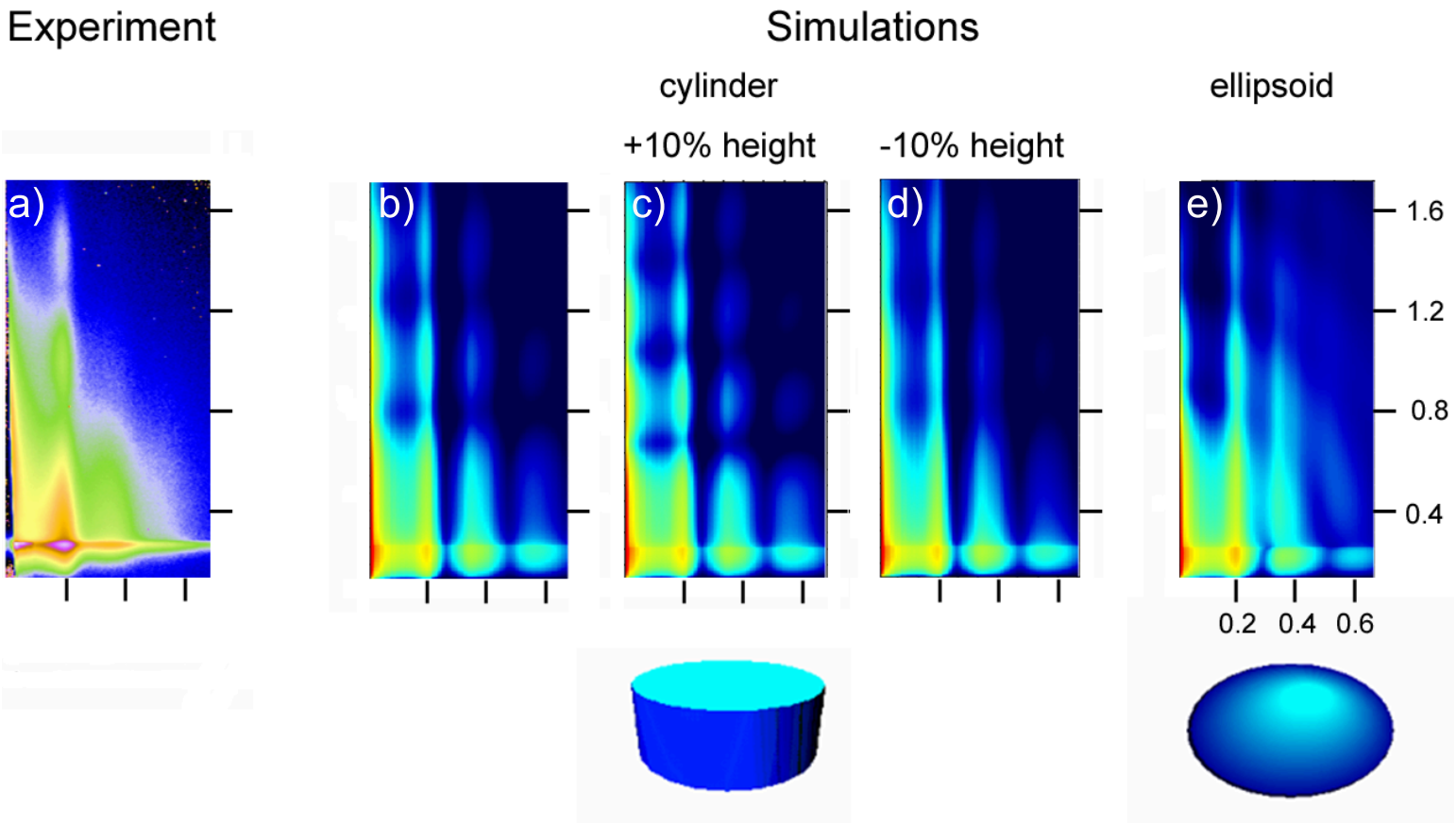

Figure 3.8: Comparison of experimental and simulated GISAXS diffractograms. The experimental scattering pattern shown in a) is simulated by varying parameters ranging from film thickness (b,c,d) to scattering object geometry (e). Units are in nm^{-1} and are consistent across all images.

location of the rods along the q_x direction. The obvious difference between the two simulations is the curvature of the scattering intensity toward the specular beam seen with the ellipsoidal form factor. This curvature is especially prominent at the higher q values and is not observed in the experimental data, even with the higher q collection previously described. The intensity profile of a cut along the first order rod in the experimental data is compared to cuts from cylindrical and ellipsoidal form factor simulations (see Figure 3.9). Data from experiment and both simulations agree modestly well at low q values, but start to diverge quickly and become distinctly different at large q. The experimental (red) and cylinder profiles (green) agree well in the location of their minima and maxima while the ellipsoid profile (blue) exhibits a mismatch with its shifted second minimum and maximum. The experimental data is simply better reproduced with the cylindrical form factor in that the scattering intensity exists as lines along the q_z direction and its profile of minima and maxima shows better registry. Another important variable is the aspect ratio of the scattering object because this directly dictates the spacing of the intensity modulations in the q_z direction. Since the lateral dimension of the film is fixed and well-known from the AFM data, simulations are fitted by varying the film thickness (see Figures 3.8b, c, and d). Note that these modulations exist for both the cylindrical and ellipsoidal simulations (although distorted by the curvature in the ellipsoidal case) and best fitting is obtained with a film thickness about equal to the pore radius, *i.e.* an aspect ratio of about 1. The scattering pattern is very sensitive to this parameter, such that the confidence is within 10% of the best-fit value obtained from the simulations (compare Figures 3.8b, c, and d). It is also important to note that with the GISAXS setup possessing a very long sampling footprint, the existence of these intensity modulations in the diffractogram requires that the film thickness and pore size be extremely uniform across macroscopic dimensions. Any wide distribution of either parameter would smear

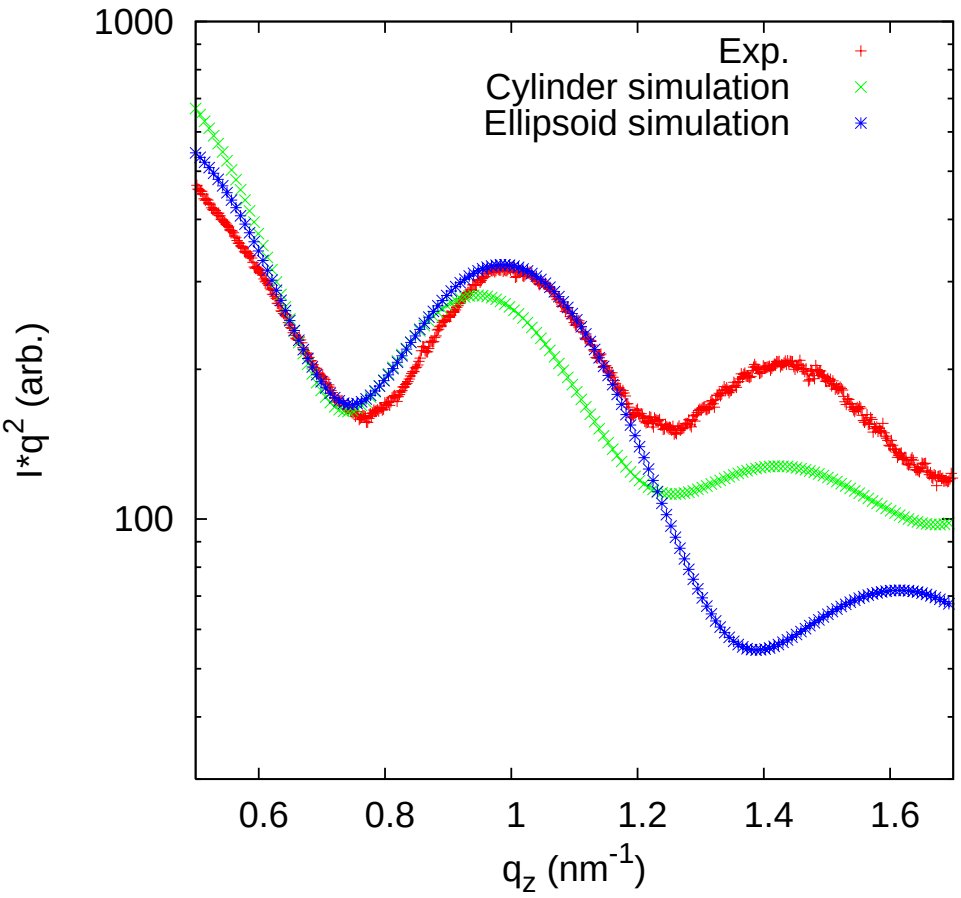

Figure 3.9: Comparison of experimental and simulated GISAXS diffractograms along the first order cut. The experimental data shown is red is better reproduced by the cylinder simulation (green) than the ellipsoid simulation (blue) especially the registry of the second peak: the experimental and cylinder profiles both show a maximum while the ellipsoid profile shows a minimum.

Table 3.5: Local and global comparison

technique	pore-pore spacing	pore diameter	film thickness	domain size
AFM/SEM	34.6 nm	25.8 nm	16.0±1.6 nm	$\sim$ 100 nm
GISAXS	34.6 nm	26.0±2.6 nm	14.0±1.0 nm	100±20 nm

out the modulations resulting in a solid rod of scattering intensity.

The values obtained for the different thin film parameters (pore-to-pore spacing, pore radius, film thickness, and domain size) from local data analysis are consistent with the values obtained from global data analysis, see Table 3.5. The pore-to-pore spacing extracted directly from the AFM and experimental GISAXS data show extremely good agreement. The other three thin film parameters were extracted from AFM/SEM/IDL data and agree well with simulated GISAXS spectra. The consistency of these local and global characterization techniques suggest that these thin films are extremely uniform over macroscopic dimensions and characterization over limited length scales, ca. microns, is sufficient to describe the entire sample.

Pore shape changes

From cross-sectional SEM (Figures 3.3a and c), it is evident that in contrast to calcined samples, as-made films posses ellipsoidal pores. These curved pores thus must undergo straightening when subjected to the calcination process as scattering data suggest. This shape change can be rationalized through a simple consideration of surface energy and the drive to straighten any high energy (e.g. curved) surfaces (Figure 3.10). Calculations of the two extreme cases, spherical and cylindrical pores, show that there is a small decrease in surface energy when converting from the former to the latter shape.

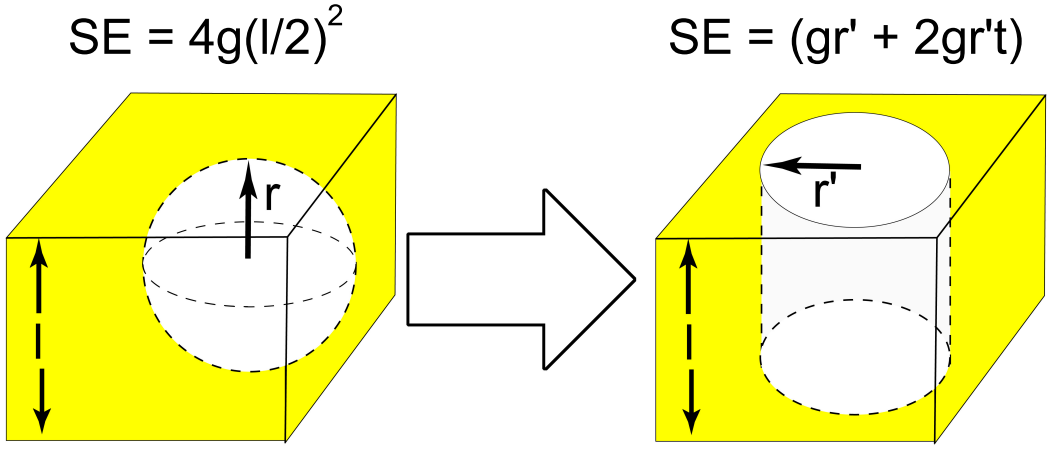

Figure 3.10: Conversion of spherical/ellipsoidal to cylindrical pores. There is a small decrease in surface energy driving the conversion due to the loss of the cylinder top.

The surface energy, S.E., for a spherical void is calculated as follows:

$$S.E._{sphere} = \gamma 4\pi r^2 \tag{3.5}$$

where γ is the surface energy per unit length and r is the radius of the spherical void. From Figure 3.10, the radius is simply half the film thickness, l. Equation 3.5 then reduces down to:

$$S.E._{sphere} = \gamma \pi l^2 \tag{3.6}$$

For a cylindrical void (without a top surface), the surface energy is given by:

$$S.E._{cylinder} = \gamma(\pi r'^2 + 2\pi r' l) \tag{3.7}$$

where the first term derives from the cylinder bottom, the second term from the cylinder sidewalls, and r' is a reduced radius that can be calculated from volume conservation considerations and is given by $r' = l/\sqrt{6}$. Equation 3.7 reduces to:

$$S.E._{cylinder} = \left(\frac{1+2\sqrt{6}}{6}\right)\gamma\pi l^2 \approx 0.98\gamma\pi l^2 \tag{3.8}$$

Comparison of Equations 3.6 and 3.8 shows that there is a slight gain in surface energy converting a spherical void into a cylinder. AFM data confirm these voids are accessible from the top, thus the assumption of open cylinders in the calculation is valid. Rather than any extreme the real shape of the scattering object (pore) is expected to be a mixture of a cylinder and ellipsoid but heavily skewed toward the former, due in part to the anisotropic film shrinkage, resulting in a barrel shape. This minor curvature does not manifest itself as a broad bending of scattering intensity but rather as a uniform intensity in higher order peaks.

Scaling relations from pore parameters

In the present study we have shown that the process of hybrid thin film formation is robust and can accommodate changes in block copolymer composition and inorganic loading. Control over pore size and spacing was achieved mainly through modifying processing parameters such as thermal treatments and spin coating settings. To access a larger range of feature sizes, in particular pore diameters and pore–to–pore distance, and exert tighter control, block copolymers of different molecular weights were used. Since the pore spacing is defined by macromolecular length, characteristic film dimensions are now controlled by a parameter inherent to the material instead of external processing variables. Different sized features can now be accessed by using the natural dimension of the polymer material instead of distorting films away from their equilibrium. Table 3.1 lists the different PI–b–PEO copolymers A-D employed that range from 16-100 kDa in molecular weight and form thin films with characteristic dimensions (pore-to-pore distance, λ) as measured by AFM in the range of 29-55 nm. Below a critical molecular weight, PI–b–PEO/glymo/Al(O^sBu)$_3$ hybrids do not form microphase separated thin films simply because there is not enough gain in free energy to drive the

assembly. Thus a different polymer choice is necessary. By selecting a different block copolymer as the structure directing agent, two things are achieved: 1) a polymer with a larger interaction parameter, χ, will insure that microphase separation will occur at lower molecular weights thus achieving smaller feature sizes, and 2) by generalizing this methodology of hybrid thin film formation to other block copolymer systems we further demonstrate its robustness. To this end, small molecular weight poly(ethylene propylene–block–ethylene oxide) (PEP–b–PEO–B, see Table 3.1) was successfully used to create films with feature sizes down to 20 nm without the need to change any processing or compositional parameters. AFM characterization of a sampling of different molecular weight derived thin films is shown in Figure 3.11. Film quality and ordering is maintained across two different copolymer types and a wide range of molecular weights, with a bit of order degradation at the higher end as expected from the increased polymer viscosity. The characteristic pore-to-pore spacing of thin multilayer films are plotted against the molecular weight of their parent copolymers (PI–b–PEO only) in Figure 3.12. Note that only samples that were fully optimized (similar composition to Ch2, spin coating at 2000 RPM at 250 RPM/s, calcination to 500 °C at 5 °C min^{-1}; see Table 3.3 and Experimental section) were used in this analysis. A linear function can be fitted to this data on a log-log plot to extract the exponent, ν, of the power-law dependence of feature size on molecular weight (ν_{film} = 0.34). The low value of ν and comparison to all-organic block copolymer bulk data analysis [36] (ν_{bulk} = 0.66) suggest that there are additional contributions to the structure formation process than what is observed in the bulk. Several factors may contribute to the unphysically low exponent, but the most important ones can be expected to include the thin film nature of the samples (*i.e.* contributions from interfaces) and the competing polymer mobility versus the inorganic crosslinking rate previously discussed (see Monolayer films and RDF and

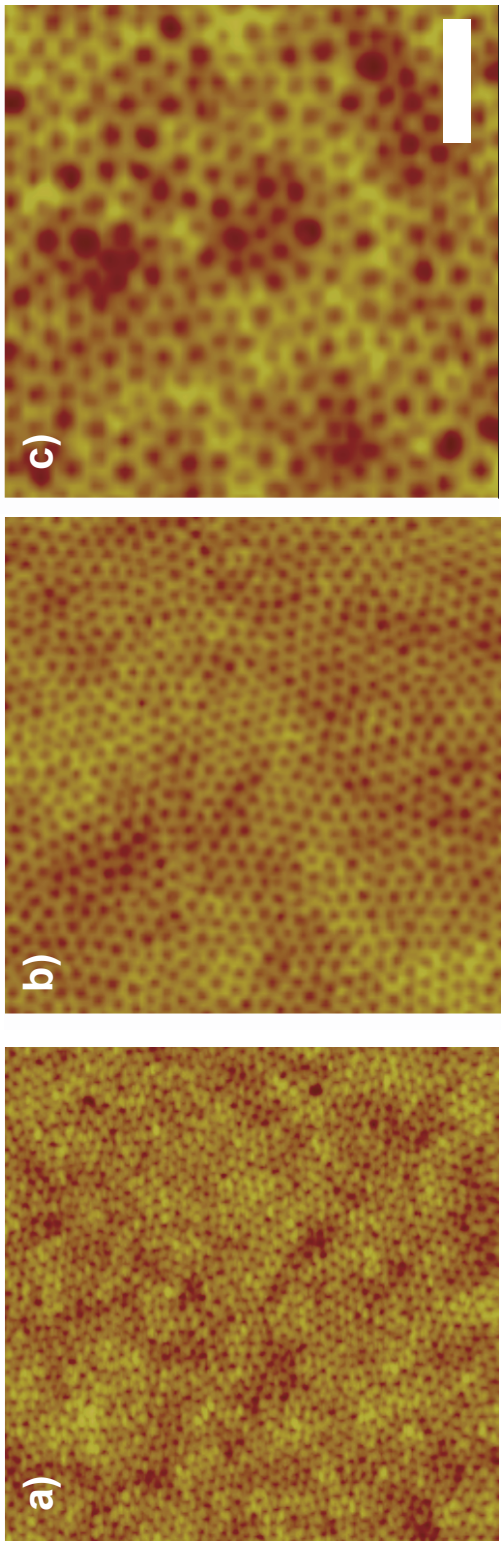

Figure 3.11: Feature size scaling through selection of different molecular weight parent block copolymer: a) from the 3.6kDa PEP–b–PEO copolymer, b) from a 38.7 kDa PI–b–PEO copolymer, c) from a 95.5 kDa PI–b–PEO copolymer. Scale bar = 250 nm

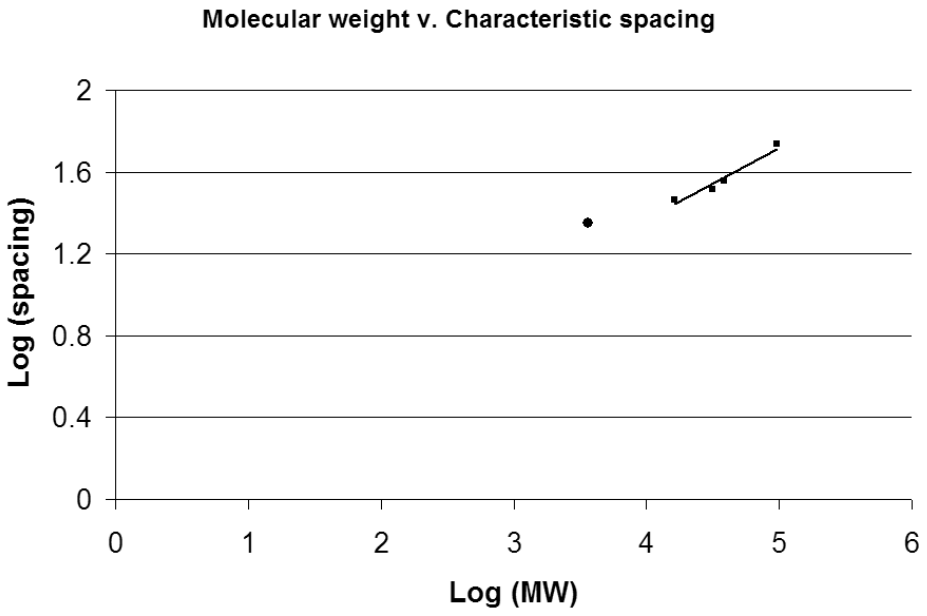

Figure 3.12: Molecular weight scaling of feature size plotted on a log-log plot. The power law exponent, $\nu = 0.34$, is obtained from fitting the PI–b–PEO hybrid samples (squares). The inclusion of the PEP–b–PEO hybrid sample shows that smaller feature sizes are accessible (circle).

BODF analysis sections, respectively). A kinetically trapped state is consistent with the current disorder found within the samples in this study but also suggest improvements to the ordering is still possible. In any case for the specific processing condition used, this predictive model allows for the effective selection of the proper molecular weight polymer for a targeted feature size.

Conclusion

We have made mesostructured hybrid organic-inorganic thin films ($<$100 nm) using diblock copolymers as structure directing agents for aluminosilicate precursors. Films were optimized through variables such as thermal treatments, spin coating settings, and inorganic loading, that fall under two categories: processing and composition. Thin films were characterized through a variety of methods, both on the local and global scale, with the various techniques providing complimentary data. Quantitative analysis helped identify grain size, defect density, type and location, angular distribution, film thickness, scattering object geometry, aspect ratio, and ordering regime. This type of analysis not only enables the monitoring of film development, but also links processing/composition parameters to final film quality and ordering. The robustness of film formation was exemplified by its success with monolayer and multilayer assemblies, various neat copolymer block fractions and inorganic loadings, and across different types of block copolymers. A predictive model facilitates making the proper decision for targeted film dimensions and ordering specifically tailored to meet the end needs.

Bibliography

[1] T. Thurn-Albrecht, J. Schotter, C. A. Kastle, N. Emley, T. Shibauchi, L. Krusin-Elbaum, K. Guarini, C. T. Black, M. T. Tuominen, and T. P. Russell. "Ultrahigh-density nanowire arrays grown in self-assembled diblock copolymer templates" *Science*, **2000**, *290*, 2126.

[2] A. Urbas, R. Sharp, Y. Fink, E. L. Thomas, M. Xenidou, and L. J. Fetters. "Tunable block copolymer/homopolymer photonic crystals" *Advanced Materials*, **2000**, *12*, 812.

[3] K. Asakawa, T. Hiraoka, H. Hieda, M. Sakurai, and Y. Kamata. "Nano-patterning for patterned media using block-copolymer" *J Photopolym Sci Tec*, **2002**, *15*, 465.

[4] F. P. Mathew and E. C. Alocilja. "Porous silicon-based biosensor for pathogen detection" *Biosensors & Bioelectronics*, **2005**, *20*, 1656.

[5] P. F. W. Simon, R. Ulrich, H. W. Spiess, and U. Wiesner. "Block copolymer-ceramic hybrid materials from organically modified ceramic precursors" *Chem. Mat.*, **2001**, *13*, 3464.

[6] F. S. Bates and G. H. Fredrickson. "Block copolymer thermodynamics: theory and experiment" *Annual Review of Physical Chemistry*, **1990**, 41, 525.

[7] R. A. Segalman. "Patterning with block copolymer thin films" *Materials Science & Engineering R-Reports*, **2005**, *48*, 191.

[8] P. Du, M. Q. Li, K. Douki, X. F. Li, C. R. W. Garcia, A. Jain, D. M. Smilgies, L. J. Fetters, S. M. Gruner, U. Wiesner, and C. K. Ober. "Additive-driven phase-selective chemistry in block copolymer thin films: The convergence of top-down and bottom-up approaches" *Advanced Materials*, **2004**, *16*, 953.

[9] P. Mansky, J. DeRouchey, T. P. Russell, J. Mays, M. Pitsikalis, T. Morkved, and H. Jaeger. "Large-area domain alignment in block copolymer thin films using electric fields" *Macromolecules*, **1998**, *31*, 4399.

[10] W. H. Tang. "Confinement of symmetric diblock copolymer thin films" *Macromolecules*, **2000**, *33*, 1370.

[11] P. Muller-Buschbaum, J. S. Gutmann, C. Lorenz-Haas, B. Mahltig, M. Stamm, and W. Petry. "Early stages of film creation in thin diblock copolymer films" *Macromolecules*, **2001**, *34*, 7463.

[12] K. W. Guarini, C. T. Black, and S. H. I. Yeung. "Optimization of diblock copolymer thin film self assembly" *Advanced Materials*, **2002**, *14*, 1290.

[13] R. D. Peters, X. M. Yang, and P. F. Nealey. "Morphology of thin films of diblock copolymers on surfaces micropatterned with regions of different interfacial energy" *Macromolecules*, **2002**, *35*, 1822.

[14] G. Krausch and R. Magerle. "Nanostructured thin films via self-assembly of block copolymers" *Advanced Materials*, **2002**, *14*, 1579.

[15] R. A. Segalman, A. Hexemer, and E. J. Kramer. "Effects of lateral confinement on order in spherical domain block copolymer thin films" *Macromolecules*, **2003**, *36*, 6831.

[16] M. Templin, A. Franck, A. DuChesne, H. Leist, Y. M. Zhang, R. Ulrich, V. Schadler, and U. Wiesner. "Organically modified aluminosilicate mesostructures from block copolymer phases" *Science*, **1997**, *278*, 1795.

[17] P. Du, J. S. Gutmann, P. F. W. Simon, C. B. W. Garcia, K. Guarini, C. T. Black, and U. Wiesner. "Nanostructured organic-inorganic hybrid thin films" *Polymer Preprints*, **2002**, 43, 438.

[18] J. Allgaier, A. Poppe, L. Willner, and D. Richter. "Synthesis and characterization of poly[1,4-isoprene-b-(ethylene oxide)] and poly[ethylene-co-propylene-b-(ethylene oxide)] block copolymers" *Macromolecules*, **1997**, *30*, 1582.

[19] M. A. Hillmyer and F. S. Bates. "Synthesis and characterization of model polyalkane-poly(ethylene oxide) block copolymers" *Macromolecules*, **1996**, *29*, 6994.

[20] S. C. Schmidt and M. A. Hillmyer. "Morphological behavior of model poly(ethylene-alt-propylene)-b-polylactide diblock copolymers" *J. Polym. Sci. Pt. B-Polym. Phys.*, **2002**, *40*, 2354.

[21] A. Jain and U. Wiesner. "Silica-type mesostructures from block copolymer phases: Formation mechanism and generalization to the dense nanoparticle regime" *Macromolecules*, **2004**, *37*, 5665.

[22] P. Salembier and M. Pardas. "Hiercarchical morphological segmentation for image sequence coding" *IEEE Transactions on Image Processing*, **1994**, *3*, 639.

[23] M. Berg. *Computational geometry: algorithm and applications*. Springer, New York, 2000.

[24] N. Tokita, M. Hirabayashi, C. Azuma, and T. Dotera. "Voronoi space division of a polymer: topological effects, free volume, and surface end segragation" *J. Chem. Phys.*, **2004**, *120*, 496.

[25] http://www.esrf.fr/computing/scientific/joint_projects/IsGISAXS/isgisaxs.htm.

[26] D. E. Angelescu, J. H. Waller, R. A. Register, and P. M. Chaikin. "Shear-induced alignment in thin films of spherical nanodomains" *Adv. Mater.*, **2005**, *17*, 1878.

[27] B. I. Halperin and D. R. Nelson. "Theory of two-dimensional melting" *Phys. Rev. Lett.*, **1978**, *41*, 121.

[28] D. R. Nelson and B. I. Halperin. "Dislocation-mediated melting in two dimensions" *Phys. Rev. B*, **1979**, *19*, 2457.

[29] D. Frenkel and J. P. McTague. "Evidence for an orientationally ordered two-dimensional fluid phase from molecular dynamics calculations" *Phys. Rev. Lett.*, **1979**, *42*, 1632.

[30] A. H. Marcus and S. A. Rice. "Observations of first-order liquid-to-hexatic and hexactic-to-solid phase transitions in a confined colloid suspension" *Phys. Rev. Lett.*, **1996**, *77*, 2577.

[31] R. P. A. Dullens and W. K. Kegel. "Reentrant surface melting of colloidal hard spheres" *Phys. Rev. Lett.*, **2004**, *92*, 195702.

[32] J. R. Levine, J. B. Cohen, Y. W. Chung, and P. Georgopoulos. "Grazing-incidence small angle x-ray scattering: new tool for studying thin film growth" *J. Appl. Cryst.*, **1989**, 22, 528.

[33] D.-M. Smilgies, P. Busch, C M. Papadakis, and D. Posselt. "Characterization of polymer thin films with small-angle x-ray scattering under grazing incidence (GISAXS)" *Synchrotron Radiation News*, **2002**, *15*, 35.

[34] A. C. Finnefrock, R. Ulrich, G. E. S. Toombes, S. M. Gruner, and U. Wiesner. "The plumber's nightmare: A new morphology in block copolymer-ceramic nanocomposites and mesoporous aluminosilicates" *J. Am. Chem. Soc.*, **2003**, *125*, 13084.

[35] R. Lazzari. "Isgisaxs: a program for grazing-incidence small-angle x-ray scattering analysis of supported islands" *J Appl Crystallogr*, **2002**, 35, 406.

[36] T. Hashimoto, M. Fujimura, and H. Kawai. "Domain-boundary structure of styrene-isoprene block copolymer films cast from solution. 5. molecular-weight dependence of spherical microdomains" *Macromolecules*, **1980**, *13*, 1660.

CHAPTER 4

NANOPILLAR ARRAYS FROM LASER INDUCED CAPILLARY FILLING OF MESOSTRUCTURED BLOCK COPOLYMER HYBRID THIN FILM TEMPLATES

Abstract

Photolithography is traditionally used to structure silicon, but is currently limited to the $\sim$50 nm regime and requires expensive and time consuming processes. Here we present an inexpensive and facile route for patterning silicon on two length scales; 1) the nanometer length scale through the use of a block copolymer derived inorganic thin film and 2) the micron scale through the use of a mask. The mesostructured inorganic film is used as a template for a transient ($<$50 ns) laser melt. Capillary driven filling of the template leads to an array of nanopillars. The placement of these arrays can be controlled by defining the laser exposure with a simple mask. Characterization of the surface before and after laser melt confirms high pattern transfer efficiency and registry.

Nanostructuring of silicon-type surfaces employing organic molecule self-assembly is generally limited to low temperature processing [1]. Ordered nanostructures tolerating high temperatures have require, in contrast, conventional and expensive lithographic patterning methods [2]. Recent techniques have extended polymer self-assembly in the bulk to form inorganic silica-type nanostructures, which can be varied by engineering the precursor macromolecules [3]. This chapter demonstrates that such techniques can be employed to create high temperature stable monolayer-type porous structures on Si that can serve as templates for a laser-induced capillarity-driven filling process to form Si nanopillars. This leads to an extremely efficient method for generating large arrays of nanostructured surfaces, with control of the surface structure geometry and feature sizes down to the molecular level. Since this process may be extended to materials other than Si and to gallery-type structures, it offers enormous scientific and technological promise in a wide range of fields including nanofluidics, biosensors and nanoelectronics.

The nanopillar array fabrication is schematically shown in Fig. 4.1A. Bare silicon wafers (Fig. 4.1Ai) that underwent an RCA clean and HF final dip were spun coat with a mixture of metal alkoxides [(3-glycidyloxypropyl-) trimethoxysilane and aluminum sec-butoxide] and poly(isoprene–b–ethylene oxide) (PI–b–PEO) block copolymer. This formed a phase-separated inverse hexagonal mesophase monolayer [4], with one phase inorganic-rich (PEO+inorganic) and the other purely organic (PI). The organic components were subsequently removed by slow heating to 500°C, leaving the ordered mesoporous hexagonal array (Fig. 4.1Aii). Control of the film thickness to near-monolayer levels was achieved through a combination of solution concentration, acceleration rate and spin speed [5]. The nanopore lattice spacing was 32 nm with a physical thickness after calcination of 18 nm, as determined by a combination of scanning electron microscopy and X-ray diffraction [5]. This nanoporous oxide structure in itself has po-

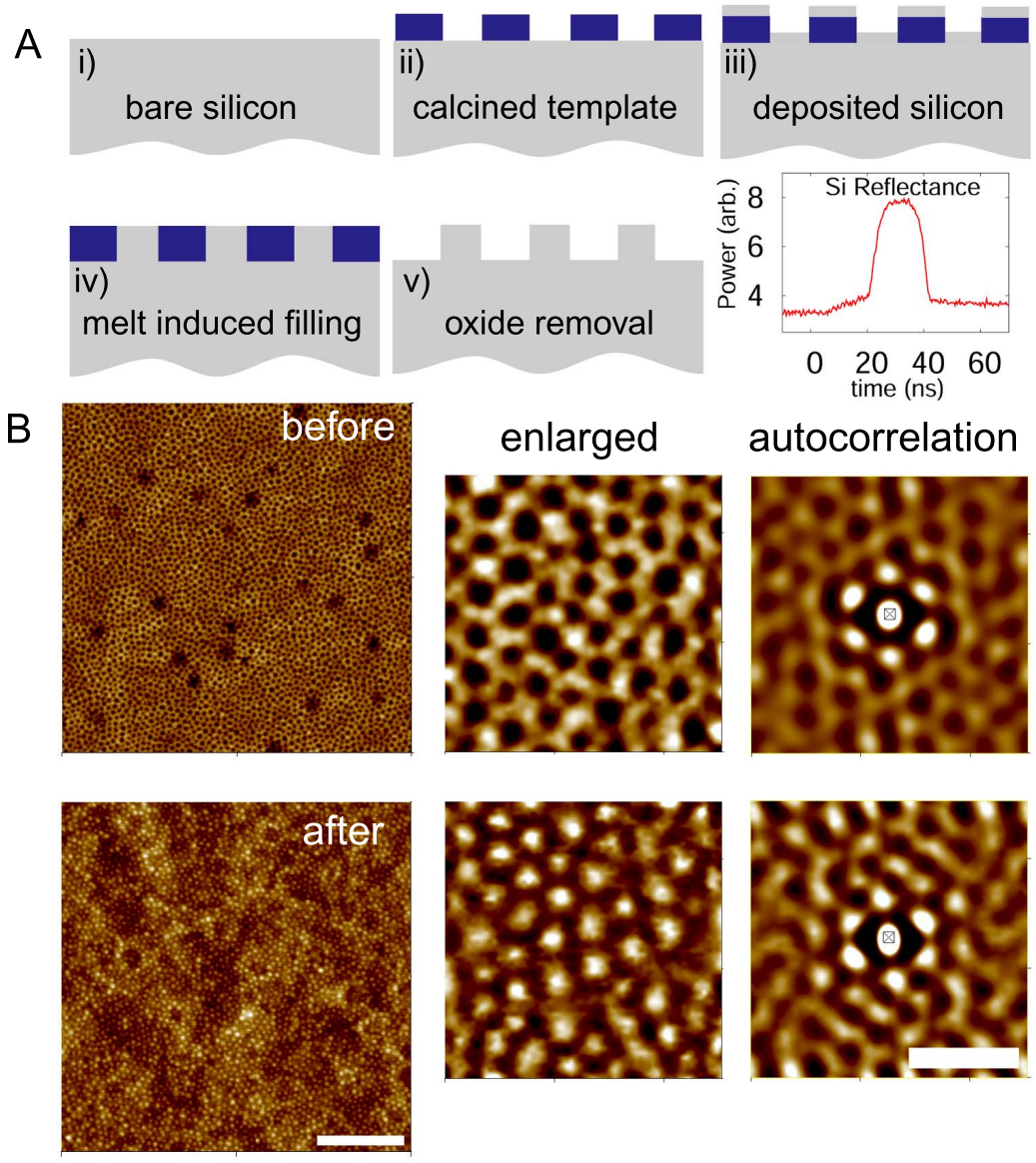

Figure 4.1: A) Schematic for fabrication of a nanopillar array. Starting with a i) bare silicon wafer, a ii) thin (∼20 nm) aluminosilicate film is constructed by spin coating a polymer/sol nanoparticle solution. Optional deposition of amorphous silicon iii) onto the template and substrate is followed by iv) exposure to an excimer laser for capillary driven pore filling. v) A HF etch removes the aluminosilicate film and exposes the nanopillars. vi) The reflectance profile of the silicon measured in-situ during the excimer laser exposure showing a melt duration of ∼20 ns. B) AFM images of the aluminosilicate film before and after laser exposure and HF strip depicting the nanopillars. The enlarged AFM images show good registry between the template and nanopillars with the autocorrelation confirming the strong six-fold orientation. Scale bars = 500 nm and 100 nm for the standard and enlarged AFM scans, respectively.

tential applications in numerous areas, such as magnetic data storage [6].

This structure was subsequently used as a template for forming nanopillars with predetermined size and shape, using a nanosecond laser-induced transient melt and solidification process (step iv in Fig.4.1A) where capillary forces fill the pores with liquid Si. On the time-scale of pulsed laser-induced melts (∼20–100 ns), sintering collapse of the pores is avoided. Samples were irradiated with a 30 ns pulse from a XeCl excimer laser (λ=308 nm) at a fluence sufficient to melt the underlying Si substrate. Varying fluences, both below and above the Si single-crystal melt threshold (E_{melt} = 600 mJ/cm^2), for several (1-15) pulses were required to melt the underlying crystal Si, break through the native oxide, and fill the nanopores (Fig. 4.1Aiv). The duration of the melt was determined in situ using a probe CW laser monitoring the surface reflectance; the high reflectivity period corresponds to a surface melt (see Fig. 4.1Aiv). With typical duration of 20 ns, this corresponds to a "filling" velocity of order 0.5-1.0 m/s and, despite the low viscosity of liquid Si (0.34 centistokes), should still result in laminar flow through the pores. With adequate control, it may be possible to grow these pillars epitaxial from the substrate. After laser irradiation, the aluminosilicate template is etched away using a 48% HF solution to expose the nanopillar array (Fig. 4.1Av). Fig. 4.1B shows an AFM image of a sample before and after irradiation with five laser pulses (and removal of the skeletal aluminosilicate). Following laser treatment, the regular array of dots change from dark to bright in color, confirming the conversion of the nanopores to nanopillars. Auger spectroscopic measurements confirm no residual oxides with the remaining structures being pure Si. The template of the nanopores is replicated in the nanopillars, as demonstrated by corresponding FFT autocorrelations showing similar hexagonal symmetry (Fig. 4.1B, enlarged portion).

These AFM results were characterized further using a quantitative analysis software

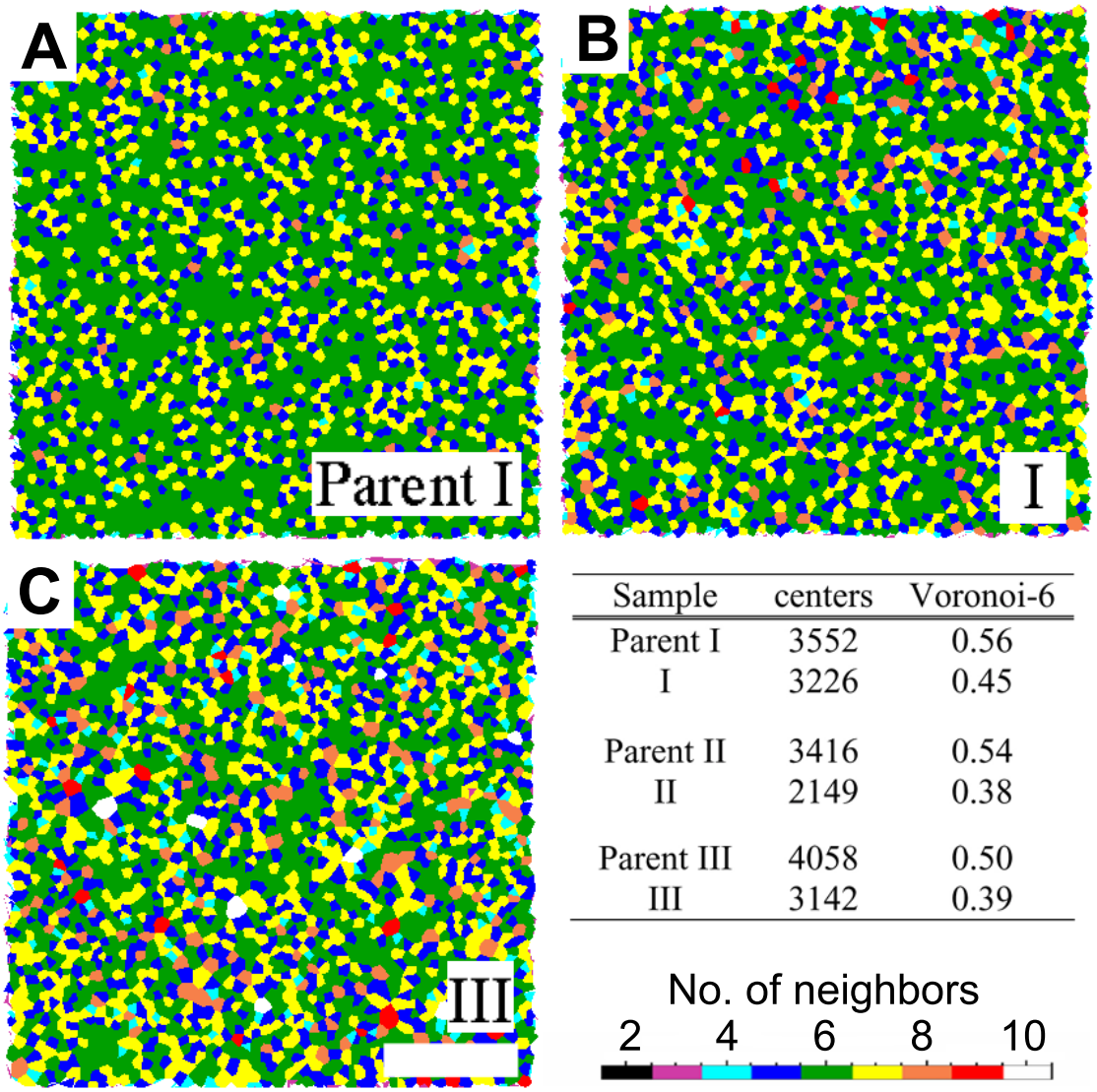

Sample	centers	Voronoi-6
Parent I	3552	0.56
I	3226	0.45
Parent II	3416	0.54
II	2149	0.38
Parent III	4058	0.50
III	3142	0.39

Figure 4.2: Voronoi diagrams for A) template, B) short nanopillars formed on bare Si, and C) tall nanopillars formed from 5 nm deposited a-Si films. The ordering degrades slightly with laser irradiation as represented by the increase in the number of defects (non-six nearest neighbor sites, non-green polygons). The color bar depicting the number of nearest neighbors is in the lower right corner. The statistics for three nanopillar samples, I-III, and their parent templates with number of pores/pillars and the Voronoi-6 ratio (fraction of six-fold sites) are shown in the lower right.

program described elsewhere [5]. Fig. 4.2 shows representative Voronoi diagrams of the template skeletal aluminosilicate and the subsequent nanopillars (Figs. 4.2A and B). The Voronoi diagram represents the number of nearest neighbors of a pore (pillar) and is color-coded to facilitate identification of grain size and location of defects. The Voronoi-6 ratio, defined as the fraction of pores (pillars) with 6-fold hexagonal nearest neighbor symmetry, provides a simple metric for sample comparison. As indicated by the increased number of defects in the Voronoi diagram, the transformation from pores to pillars introduces some disorder into the system. However, transfer of the template into silicon pillars is accomplished at a high efficiency, with a greater than 90% number of pores to pillars conversion and only a 20% decrease in the Voronoi-6 ratio (table in Fig. 4.2D, sample I).

Although the transfer fidelity was good on the lateral dimensions, cross sectional AFM analysis showed the pillars to be only 1–2 nm high, possibly due to the poor wetting of silica by molten silicon [7] (Fig. 4.3A, inset). This motivated the development of a modified process to improve the filling of the pores and form taller pillars. An amorphous silicon (a-Si) (Fig. 4.1Aiii) overlayer was deposited to help fill the pores from the top and circumvent the need to wet silica. The deposited silicon will melt, flow into the pores from above and below, and solidify from the substrate following the laser irradiation process. Five nm of amorphous silicon was thermally evaporated onto the calcined template followed by laser exposure and an HF etch. A representative AFM height image of such a nanopillar array is shown in Fig. 4.3B. The pillar height increased to $\sim$15 nm, an order of magnitude increase over bare Si wafer results (Fig. 4.3B, inset). Voronoi analysis shows a low transfer efficiency of 63% during the pore to pillar conversion and a Voronoi-6 ratio decrease of 30%, see table in Fig. 4.2, sample II. These arrays also show slightly more disorder with a greater number of defects compared to

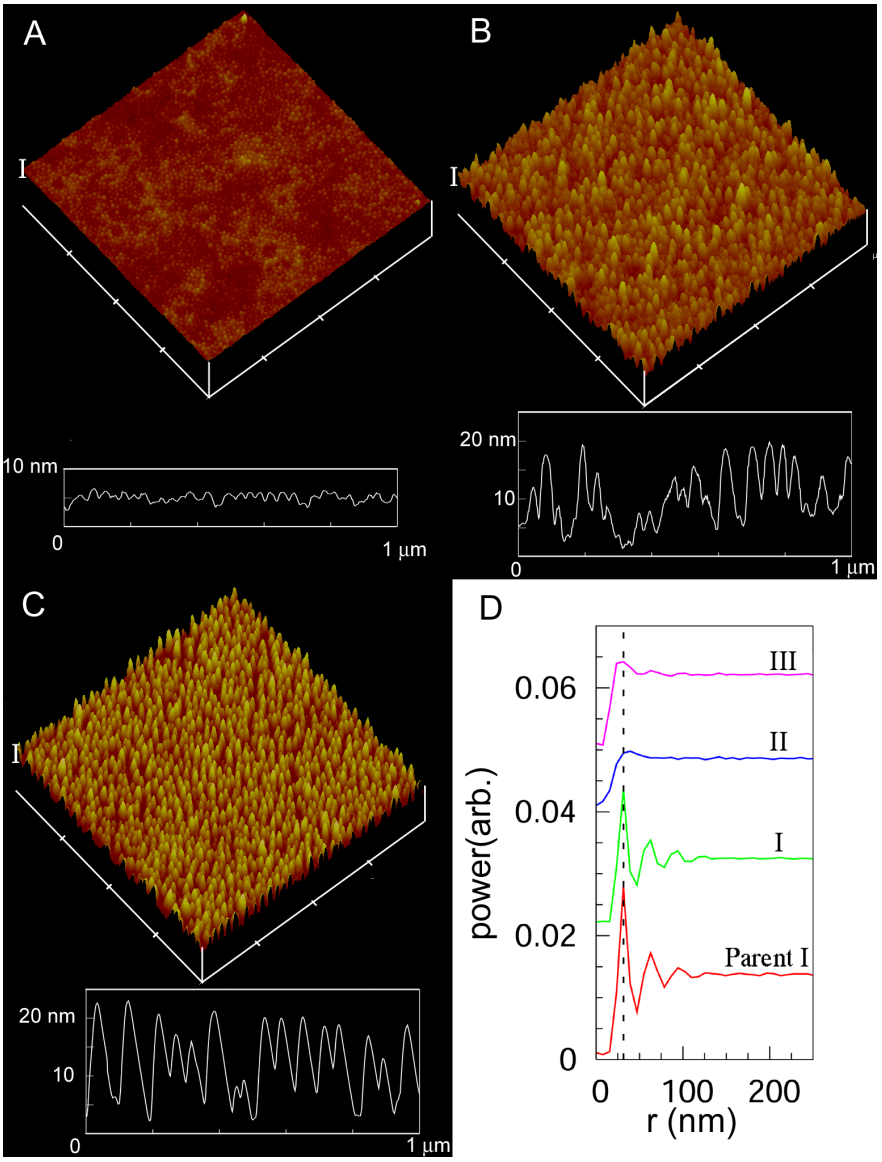

Figure 4.3: 3D AFM images and line scans of the A) short nanopillars formed from bare Si, B) tall nanopillars formed from 5 nm deposited a-Si, and C) tall, uniform nanopillars formed from 12 nm deposited a-Si films. Each scan is 2μm x 2μm and the I–bar along the z-axis depicts 20 nm. D) Radial distribution functions of the parent template (Parent I), short nanopillars (I), tall nanopillars (II), and tall, uniform nanopillars (III). Only one Parent RDF is shown for clarity. Curves from the parent template and pillar array (I) show very good agreement with only a slight loss of correlation at larger r values for the pillar array. Curve II depicts the shift of the first order maximum to a higher r value and loss of long range ordering in tall nanopillar arrays with 5 nm a-Si. Curve III shows that the uniform nanopillar arrays made from $\sim$12 nm deposited silicon templates regain the proper first order spacing and higher order correlations.

short nanopillar results from bare Si samples (compare Figs 4.2B and C). The quality of the pillars improved when a thicker layer ($\sim$12 nm) of amorphous silicon was deposited on samples (step iii in Fig. 4.1A). After laser irradiation and HF etch, Voronoi analysis shows a more efficient pattern transfer (compared to the $\sim$5 nm deposited samples) with a 77% pore to pillar conversion and only a 22% Voronoi-6 decrease (see table in Fig. 4.2, compare samples II and III).

To understand the structure development with deposited overlayers, the radial distribution functions (RDF, Fig. 4.3D) of the AFM images were computed. The RDF of the unirradiated template (Parent I) exhibits a narrow first order maximum and multiple higher order peaks, consistent with previous work [5]. Without deposited silicon, the short nanopillar array RDF (I) shows very similar characteristics with only slightly less power in each peak due to the slightly increased disorder. The RDF's of films from 5 and 12 nm deposited Si behave quite differently. Both exhibit a first order maximum shifted to larger distances, r = 39 nm, compared to the template (r = 31 nm) and a quick decay without additional higher order peaks. Since no simple mechanism could explain this, the AFM images were examined on a local scale. Locally there were sequences of pillars with the expected nearest neighbor distance, surrounded by neighbors with distances closer to the expected second nearest neighbor value. This suggests that a significant number of pores simply did not get filled—consistent with the 37% loss of centers from the Voronoi analysis. The corresponding RDF maximum indeed lies in between the nearest and second nearest neighbor radii and may be caused by a slight deformation of the template toward the empty space upon melting. RDF analysis from the 12 nm deposited Si films shows the spacing of the parent template (Fig. 4.3D, RDF III) and clear evidence of a second order peak. This result strongly supports a template mediated nanopillar formation mechanism.

The "bottom-up" fabrication approach for arrays of silicon nanopillars can be combined with "top-down" lithographic approaches to define specific areas of pillar formation. The ability to pattern silicon nanopillars into arbitrarily complex shapes would open up possible applications in nanofluidics, nanobiotechnology and photonics. Progress with localization of active complementary ligands through photolithography at the $\sim$500 nm length has helped elucidate the roles of compartmentalization, targeting, and membrane domains in cellular response processes [8]. Patterned areas of silicon nanopillar arrays would allow access to a length scale ($\sim$30 nm) an order of magnitude smaller than currently available and may enable a more detailed study of receptor-mediated cellular signaling. As a proof-of-principle experiment, a TEM grid was used as a simple mask during the laser irradiation process to pattern the silicon on a micron scale (see Fig. 4.4A). The grid was placed in contact with the sample surface to minimize loss of fidelity from the divergence of the homogenized incident laser (an f/4 optical system). The resulting pattern in silicon (Fig. 4.4B) after irradiation through the TEM grid indicates remarkable transfer. HF etching and subsequent AFM imaging shows distinct squares of patterned material (Fig. 4.4C). Close-up images (Fig 4.4D) of the squares confirm nanopillars in the irradiated area and smooth flat Si areas under the mask. As the image in Fig. 4.4C suggests and the AFM cross section analysis confirms (Fig. 4.4D), the pattern edges of the irradiated areas are significantly higher than the interior of the areas. Despite the poorly controlled edge effects, this simple proof-of-principle experiment does however demonstrates that the placement of nanopillar arrays can be controlled through simple imaging methods. Arbitrarily complex shapes can be thus formed by leveraging the wealth of patterning techniques currently available.

These preliminary results give clear evidence that inorganic nanopores can be transformed into nanopillars of various materials—currently demonstrated for Si, but likely

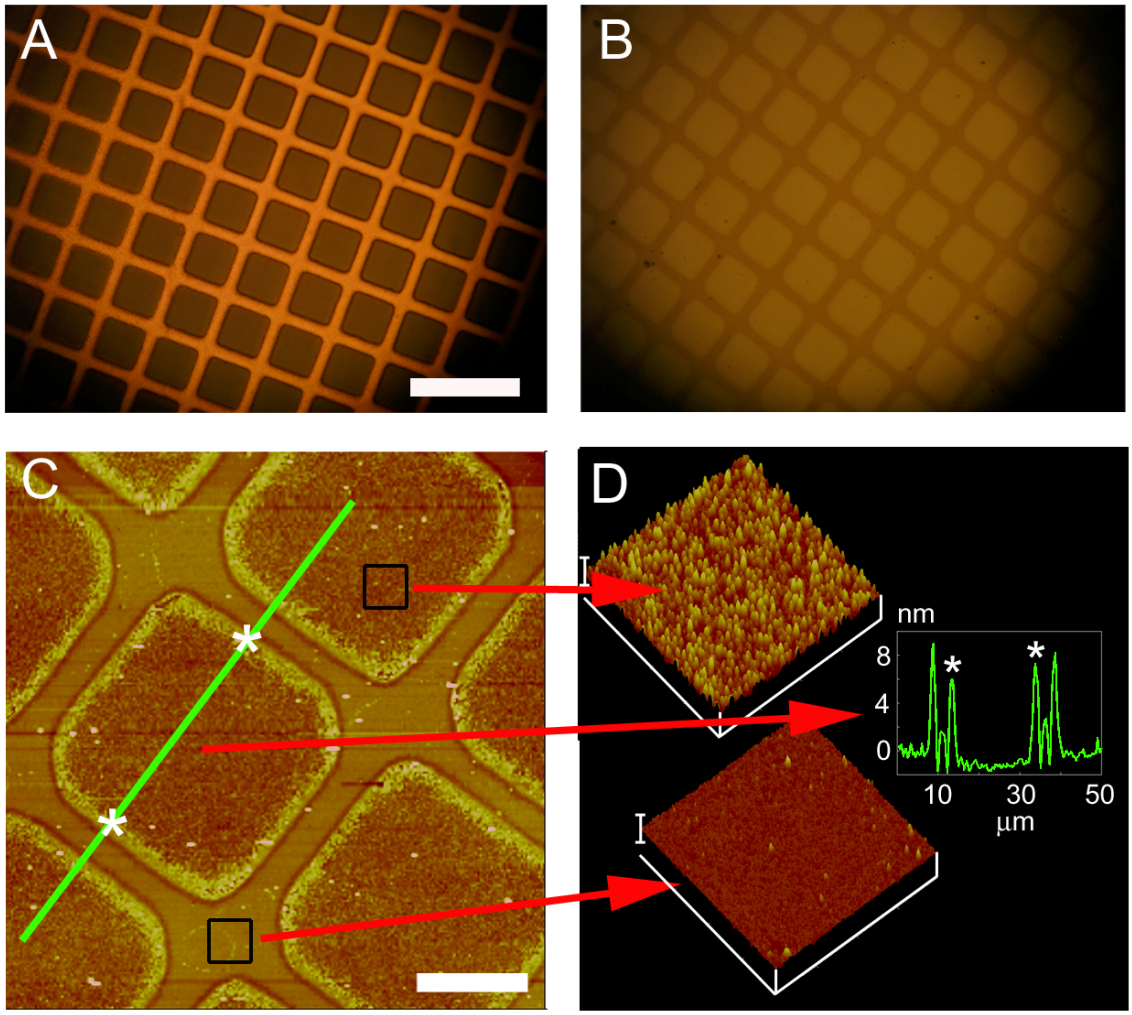

Figure 4.4: Patterning of the nanopillar array on a micron scale demonstrated by irradiating film through a mask. A) an optical micrograph of a copper TEM grid (1000 mesh) used as a mask. B) The resultant pattern on a silicon sample (with deposited amorphous silicon over the template) after laser exposure; the pattern transfer fidelity is excellent. C) After HF etching to remove the template, AFM imaging of the sample shows patterned squares of nanopillars separated by areas of flat silicon. D) Enlarged AFM scans of the boxed areas in C) clearly depict nanopillars only in the exposed regions. Cross sectional analysis, sampled along the green line in C), showing the exposed squares ringed by taller edges (marked by $*$). Optical scale bar is 50 μm for A and B. AFM scale bar is 10 μm in C. Scan size is 2μm x 2μm and the I–bar along the z-axis is 40 nm in D.

to be extensible to any material with a reasonable melting temperature and liquid viscosity. Large areas of such nanostructures can thus be fabricated in an extremely inexpensive, rapid and flexible manner without the use of traditional nanofabrication methods such as photo- or e-beam lithography. In addition, use of the polymer precursors offers tremendous variability in structural parameters, such as pore size, pore-to-pore correlation, pore wall thickness, etc. The symmetry of the phase is not restricted to hexagonal ordering since various structures are known to exist in the phase diagram of diblock copolymers, including simple cubic, lamellar, and cubic bicontinuous [10]. Furthermore, an additional level of control on the micron length scale enables placement of these nanopillar arrays at predefined locations and in arbitrary shapes. This approach opens up a wide range of novel processing technologies for various applications, which remain compatible with traditional Si device fabrication. For example, pores can be completely filled by deposition and melting of a surface film, enabling the formation of single layer nanoscale gallery-type structures, or extended 3D galleries by repeated processing. Such galleries, etched of their silica skeletons, could form the basis for integrated nanofluidic systems on a chip. Hierarchical patterning enables integration with biological systems whose interaction can be probed at multiple length scales simultaneously. Oxidation of the Si nanopillars could equally form the basis of high performance on-chip capacitors [11], or wrap-around gate MOSFETs for nanoelectronics.

Bibliography

[1] G. M. Whitesides and B. Grzybowski. "Self-assembly at all scales" *Science*, **2002**, *295*, 2418.

[2] S. Y. Chou, C. Keimel, and J. Gu. "Ultrafast and direct imprint of nanostructures in silicon" *Nature*, **2002**, *417*, 835.

[3] P. F. W. Simon, R. Ulrich, H. W. Spiess, and U. Wiesner. "Block copolymer-ceramic hybrid materials from organically modified ceramic precursors" *Chemistry of Materials*, **2001**, *13*, 3464.

[4] P. Du, M. Q. Li, K. Douki, X. F. Li, C. R. W. Garcia, A. Jain, D. M. Smilgies, L. J. Fetters, S. M. Gruner, U. Wiesner, and C. K. Ober. "Additive-driven phase-selective chemistry in block copolymer thin films: The convergence of top-down and bottom-up approaches" *Advanced Materials*, **2004**, *16*, 953.

[5] P. Du, J. S. Gutmann, S. M. Gruner, and U. Wiesner. "Block copolymer derived mesostructured silica-type thin films: complementary local and global ordering analysis" *Macromolecules, submitted*.

[6] T. Thurn-Albrecht, J. Schotter, C. A. Kastle, N. Emley, T. Shibauchi, L. Krusin-Elbaum, K. Guarini, C. T. Black, M. T. Tuominen, and T. P. Russell. "Ultrahigh-density nanowire arrays grown in self-assembled diblock copolymer templates" *Science*, **2000**, *290*, 2126.

[7] J. G. Li and H. Hausner. "Wetting and adhesion in liquid silicon ceramic systems" *Materials Letters*, **1992**, *14*, 329.

[8] W. Senaratne, P. Sengupta, C. Harnett, H. G. Craighead, B. Baird, and C. K. Ober. "Molecular templates for bio-specific recognition by low-energy electron beam lithography" *NanoBiotechnology*, **2005**, *1*, 23.

[9] The TEM grid was taped onto the silicon sample to insure good contact. Interactions between the molten silicon and the copper grid may be the cause of the unusual edges. This effect may be eliminated through the incorporation of the TEM grid into the optical line of of the excimer laser setup instead of affixing it directly onto the sample.

[10] I. W. Hamley. *The physics of block copolymers*. Oxford University Press, New York, 1998.

[11] C. T. Black, K. W. Guarini, K. R. Milkove, S. M. Baker, T. P. Russell, and M. T. Tuominen. "Integration of self-assembled diblock copolymers for semiconductor capacitor fabrication" *Applied Physics Letters*, **2001**, *79*, 409.

CHAPTER 5

ORDERED MESOSTRUCTURED HIGH TEMPERATURE CERAMICS USING BLOCK COPOLYMER MESOPHASES

Introduction

Ordered nanostructured ceramic materials have a wide variety of potential applications ranging from fuel cell membranes to molecular filtration to catalyst supports. However, the ability to form nanostructured ceramics by conventional ceramic processing is limited by the inherent brittleness of the ceramic materials. To overcome these challenges Mobil Corp. pioneered the field of using molecular surfactants to template inorganic precursors to make ordered mesoporous aluminosilicates [1]. Similarly, amphiphilic block copolymers have been shown to direct the structure of metal oxides into a variety of mesophases by using the interactions between the inorganic precursors and the organic amphiphile thereby extending the accessible pore diameters to tens of nanometers [2–4]. The inorganic components are selectively added to one of the blocks thereby swelling it. Different mesophases are observed by systematically increasing the inorganic to block copolymer weight fraction. In the meantime, this approach has been extended towards several blocked macromolecular amphiphiles [5], towards co-assembly of more than one type of inorganic particles [6, 7] and towards thin films [8].

Beyond producing mesostructured oxides, it is an interesting challenge to generalize the block copolymer approach towards high temperature polymer derived ceramics because of their excellent thermal and mechanical properties [9, 10]. As the name suggests these materials start out as a polymer, which can be easily shaped into complex structures. Heat treatment transforms the polymeric precursors into ceramic materials, while retaining the original (complex) shape. Thus these materials have a polymer-

derived structure and ceramic-like properties. In this way, unconventional structures such as fibers, coatings and microelectronic mechanical systems (MEMS) can be produced [11–13]. Since the start of the development of polymer derived ceramics in the 1980s, a wide variety of silicon-containing compounds have been examined of which the silicon-based non-oxides (Si_3N_4, SiC, SiN_xC_y, or Si_3N_4-SiC compounds) received the most attention because of their materials properties. More recently polymer derived ceramics were used for the synthesis of porous SiC and SiN_xC_y materials, using a polystyrene or silica template [14, 15].

The combination of the two initially separate research areas of block copolymer mesophase formation and polymer derived ceramics enables the synthesis of ordered mesoporous high temperature ceramics. Earlier we showed that the amphiphilic diblock copolymer poly(isoprene–*block*–ethylene oxide) (PI–*b*–PEO) can serve as structure directing agent for polyureamethylvinylsilazane (PUMVS) commercially known as Ceraset [16]. In 2004 we demonstrated for the first time that mesoporous high temperature ceramic materials stable up to 1500 °C can be made based on a related approach using poly(isoprene–*block*–dimethylamino ethylmethacrylate) (PI–*b*–PDMAEMA) as the structure directing agent for PUMVS [17]. Both the molecular structure of the block copolymer and the preceramic polymer, as well as details of the heat treatment to convert the liquid polysilazane precursor to a ceramic are shown in Figure 5.1. In the meantime similar results have been produced with polybutadiene-*block*-poly(ethylene oxide) (PB-*b*-PEO) as the structure directing agent [18].

In this paper a full account of the results on PI–*b*–PDMAEMA is given. We show that various morphologies are accessible for composites with PUMVS including the inverse hexagonal morphology from which mesoporous non-oxide type ceramics stable up to 1500° C are obtained. We provide a detailed description of the synthesis of the hybrid

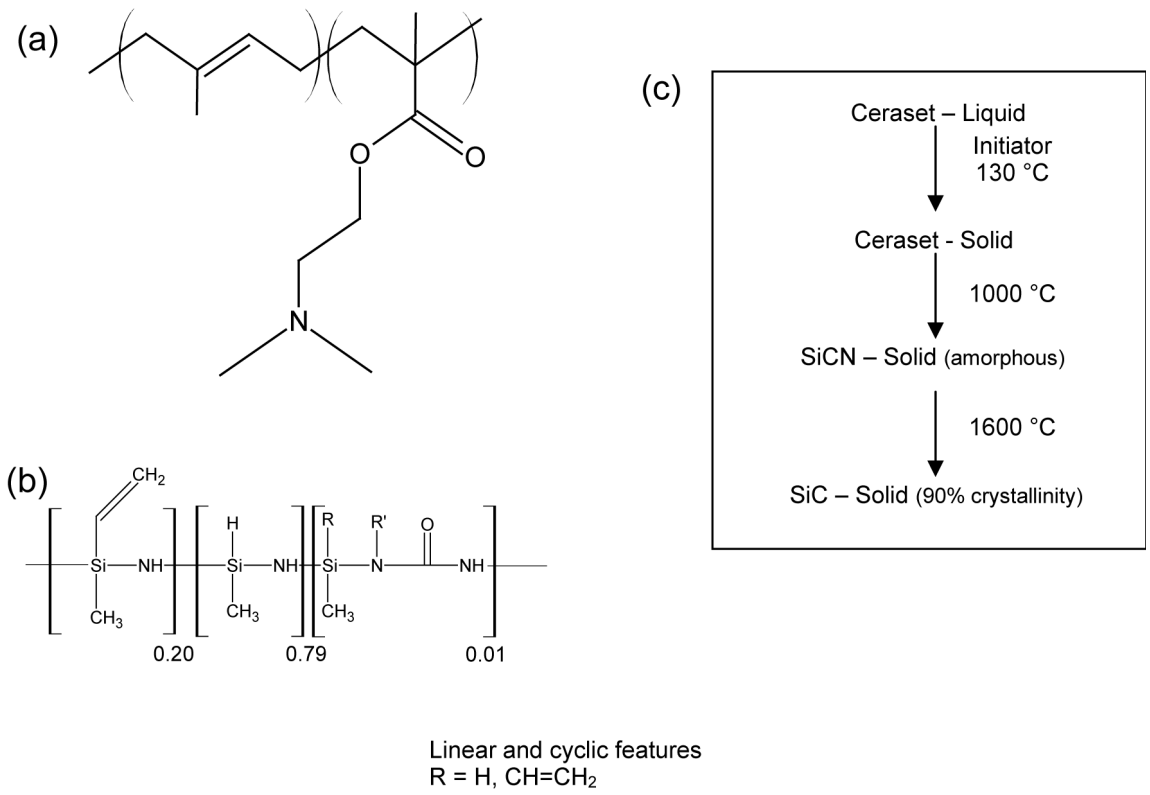

Figure 5.1: Chemical structure of (a) poly(isoprene–block–dimethylamino ethyl methacrylate) and (b) Poly(ureamethylvinyl)silazane (PUMVS). No information is available about the R'. (c) Details of the heat treatment of PUMVS resulting in amorphous SiCN or crystalline SiC [9].

materials as well as their conversion into ordered ceramic materials. We describe that in order to obtain non-oxide type ceramics the polysilazane, which reacts with water, must be kept away from all sources of moisture. The compositional changes are investigated with solid state NMR and Rutherford Back Scattering (RBS). The morphology of the samples is characterized with Small Angle X-ray Scattering (SAXS) and with Transmission Electron Microscopy (TEM). We also show that calcination under different atmospheres leads to different compositions. This is investigated with Microprobe and Wide Angle X-ray Scattering (WAXS).

Experimental Section

Materials Preparation

The block copolymer PI$-b-$PDMAEMA was polymerized by anionic polymerization [19, 20]. Gel permeation chromatography (GPC) was used to determine the molecular weight of the first block (polyisoprene, PI) and the polydispersity of the block copolymer. ^{1}H NMR was used to determine the microstructure of the PI block and the chemical composition of the block copolymer. The results were used to determine the overall molecular weight of the block copolymer. The resulting polymers had molecular weights in the range of 19 – 89 kg/mol and 10 – 33 wt% PDMAEMA with a polydispersity below 1.2, see Table 5.1.

The synthesis of the mesostructured hybrids was performed by a one-pot synthesis, in which the ceramic precursor swells the PDMAEMA block. The ceramic precursor, Ceraset (KiON Corp.) and the radical initiator, dicumyl peroxide (Aldrich) were used as received. The chemical structures of block copolymer and the polyureasilazane are shown in Figure 5.1. In a typical synthesis under dry conditions, a 5 wt% block copolymer solution in anhydrous toluene was mixed with the ceramic precursor and the radical initiator (1 wt% with respect to the mass of polyureasilazane added) and stirred inside the glove box for 1h. The solution was poured into a Petri dish under dry conditions and a film cast by solvent evaporation in an oven at 50 °C followed by annealing for 24 h under vacuum. Care was taken to insure the previous steps were performed under a nitrogen atmosphere. The temperature was increased to 130 °C for 3 h to crosslink the polyureasilazane. The composite was heat treated using 1 °C/min ramps under argon(95%)/hydrogen(5%) up to temperatures as high as 1500 °C for conversion into the high-temperature ceramic material.

Table 5.1: Characterization of PI–b–PDMAEMA block copolymers.

block copolymer	MW PI–b–PDMAEMA (g/mol)	polydispersity	wt% PDMAEMA
A	88,900	1.18	10
B	19.100	1.09	26
C	31,100	1.05	33

Gel Permeation Chromatography

Measurements were performed in 98% tetrahydrofuran (THF) and 2% N,N-dimethylacetamide at room temperature using 5 μm Waters Styragel columns (103, 104, 105, 106 Å, 30 cm each; Waters Corporation, Milford, MA) at a flow rate of 1.0 mL/min. A Waters 490 programmable multi-wavelength UV diode array detector (operated at λ = 260 nm) and a Waters 410 RI detector operated at 25 °C were used. Raw data were processed using PSS-Win GPC V6.2 (Polymer Standards Service, Mainz, Germany) software.

^{1}H, ^{13}C and ^{29}Si Nuclear Magnetic Resonance (NMR)

^{1}H, ^{13}C and ^{29}Si NMR (400 MHz or 500 MHz) spectra were recorded on a Varian INOVA 400 or 500 spectrometer using $CDCl_3$ signal as an internal standard for ^{1}H (δ = 7.27 ppm) and ^{13}C (δ = 77 ppm). TMS was used as an external standard for ^{29}Si NMR (δ = 0 ppm). ^{29}Si and ^{13}C solid state magic angle spinning (MAS) NMR studies were performed on a Bruker Advance NMR spectrometer with a 16.45 Tesla. For the 29Si NMR spectra the samples were spun in rotors with 4mm diameter at 10 kHz. The ^{29}Si NMR were acquired with cross-polarization and spinal-64 decoupling [21] using 5ms contact times and 2s recycle delay for typically 3600 scans. The ^{29}Si chemical shift scale was referenced against the Kaolin resonance at -91.3 ppm. For ^{13}C NMR measurements the samples were spun in rotors of 2.5mm diameter at 10 kHz and at 12 kHz to identify spinning sidebands. The carbonyl resonance of glycine at 176.03 ppm served as external chemical shift reference. Cross-polarization with 4ms contact times, spinal-64 decoupling and 5s recycle delays were used to acquire typically 2880 scans.

Rutherford Backscattering(RBS)

Silicon wafers were used as purchased from the Cornell Nanofabrication Facility. Thin films were fabricated by combining an amount of copolymer with 2X (by weight) PUMVS and 0.5 wt% (w.r.t. PUMVS) dicumyl peroxide in THF or toluene (4 wt% total solution) and spin coated onto silicon wafers at 2000 RPM at 250 RPM/s for a total of 1 minute in ambient atmosphere. Samples fabricated in the nitrogen glovebox (from a similar solution) were done on a makeshift spin coater (made from a 12V cooling fan motor) at 4000 RPM (uncontrolled acceleration) for a total of 1 minute. Glovebox samples were mounted onto a RBS holder and sealed in a media bottle before removal into the ambient atmosphere. All samples were annealed in a vacuum oven at 130 $^\circ$ C for 1 h to crosslink the PUMVS and permanently set the thin films. RBS measurements were taken with a 1.96 MeV He^{++} beam, 163.9° detection angle, 40μC dosage. Energy calibration was accomplished through the use of a TaSi standard.

Small Angle X-Ray Scattering (SAXS)

Experiments were performed on a Bruker-AXS NanoSTAR and at the Cornell High Energy Synchrotron Source (CHESS). The Bruker-AXS NanoSTAR setup consisted of an X-ray source (CuKα, 1.54 Å) operated at 40 kV, 40 mA in transmission mode. Göebbel mirrors were used to focus the beam. A 2-D Hi-Star area detector at a sample-to-detector distance of 62.5 cm was used to record the scattering images. 2D images were integrated over the azimuthal angle (μ) to obtain one-dimensional intensity vs scattering plots. The SAXS data obtained at CHESS was collected with a CCD 2-D detector operating at X-ray energy of 1.242 Å, sample-to-detector distance of 145.5 cm and exposure times of 1-20 sec.

Transmission Electron Microscopy (TEM)

Samples were sectioned ultrathin with a Leica Ultracut UCT microtome at -60 °C for composites and at room temperature for ceramics. Bright field TEM micrographs were taken on a LEO 922 EFTEM operating at 200 kV.

Results and discussion

We report on the preparation of mesoporous high temperature ceramic materials using PI–*b*–PDMAEMA as a structure directing agent for a polymeric ceramic precursor, polyureamethylvinylsilazane (PUMVS). Blending PUMVS with the block copolymer is expected to lead to preferential segregation of the PUMVS within the PDMAEMA domains primarily due to the polar nature of the molecule (see Figure 5.1). This increases the effective volume fraction of the PDMAEMA domains. Different mesophases similar to those in block copolymer/ homopolymer mixtures should thus be accessible by systematically increasing the polysilazane to block copolymer weight fraction. This situation can be compared to that encountered in studies of an epoxy resin embedded in one phase of a block copolymer [22, 23]. The structure is permanently set by crosslinking the polyureasilazane with a radical initiator.

Initially the hybrid samples were prepared by dissolving all the components in THF followed by casting the film in a Petri dish placed on a hotplate in ambient atmosphere. Preliminary results showed, however, that the chemical composition of the hybrid material was drastically altered during the preparation. Instead of materials composed of mainly Si, H, C, and N atoms, as expected from the starting materials, hybrids with a composition of Si, H, C, and O atoms were obtained. There are two obvious possible sources for the additional oxygen within the hybrid sample: reaction with water or

molecular oxygen. Literature suggests that the Si–N bond within the PUMVS is susceptible to attack by water, whereas molecular oxygen is not mentioned [24]. Hypothetically, the Si–N bond is attacked by water forming Si–OH bonds. The hydroxy groups can subsequently condense to form Si–O–Si bridges evolving a molecule of ammonia. In light of this mechanism, the hygroscopic nature of THF renders it as an unsuitable solvent for this system. To prove this hypothesis a series of experiments were performed. First, ^{1}H, ^{13}C and ^{29}Si NMR spectra were obtained on the PUMVS polymer, to verify the molecular structure provided by the company and to make sure that it had not degraded or reacted in any way. The NMR spectra of PUMVS as well as the ^{1}H NMR spectra of the block copolymer, PI–*b*–PDMAEMA, are shown in Figure 5.2. $CDCl_3$ was used as a solvent to obtain all the spectra. The ^{1}H NMR spectrum shows four groups of peaks. These can be assigned to Si-CH_3 (0.09 ppm), N-H (0.70 ppm), Si-H (4.24–4.80 ppm) and SiCH=CH_2 (5.54–6.14 ppm) [14]. The ratios of the CH_2=CHSi, H-Si, and CH_3-Si units were determined from the respective peak intensities to be 1:1.3:4.3, which is in reasonable agreement with the molecular structure provided by the Kion company corresponding to a ratio of 1:1.3:5. The ^{13}C NMR spectrum shows two groups of peaks, which were assigned to Si-CH_3 groups (-2.5–4.7 ppm) and CH_2=CH (137.2–141.8 and 130.3–133.1 ppm) [14]. There was no signal from the C=O groups detected, presumably because these groups are part of the repeating unit that only constitutes 1% of the PUMVS molecule and therefore this signal is too weak to be detected. The ^{29}Si NMR spectrum shows one broad group of peaks (-15– -25 ppm), which are assigned to CH_3HSiN_2 and CH_3CH_2=$CHSiN_2$ [14]. All NMR results are thus consistent with the molecular structure provided by Kion. Furthermore, the ^{1}H NMR spectrum of the block copolymer is also consistent with expectations as shown in Figure 5.2(d) [19].

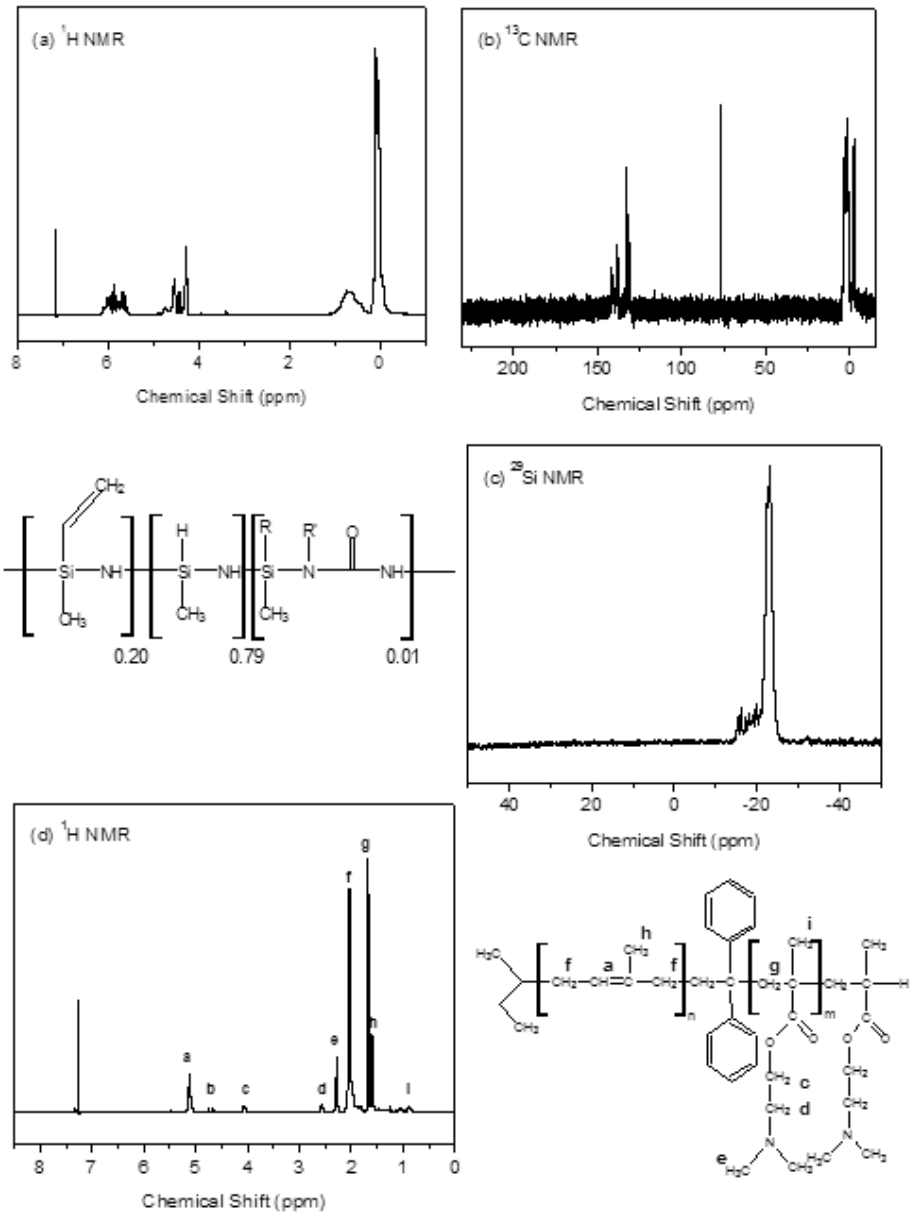

Figure 5.2: (a) ^{1}H, (b) ^{13}C and (c) ^{29}Si NMR spectra of the PUMVS polymer. $CDCl_3$ is used as a solvent for all the spectra. Note: different batches of the polyureasilazane from the supplier don't show any differences in any of the spectra. (d) ^{1}H NMR spectra of PI–b–PDMAEMA in $CDCl_3$.

Thin films

RBS experiments were performed to determine the source of the water and at which step it reacts with the hybrid sample. Thin films were created by spin coating various solutions of PI–*b*–PDMAEMA, PUMVS, and dicumyl peroxide initiator on silicon substrates, see Table 5.2. Several different methods of elemental analysis were explored, but RBS was chosen due to ease of sample preparation and straightforward interpretation of the data. Most importantly, the depth profiling nature of RBS allows for the study of elemental concentrations as a function of film depth, an especially powerful tool when dealing with reactions at interfaces and surfaces.

The RBS spectrum obtained from sample I, which contains the block copolymer and initiator but lacks the ceramic precursor in THF, is shown in Figure 5.3a. The spectrum has the characteristic profile of an organic thin film on a silicon wafer, namely light element peaks on a plateau from a heavier element substrate. This particular sample establishes the baseline for comparison to later samples with the PUMVS, in particular the amount of lighter elements (C, N, and O) contained within the hybrid material. The single peak on the silicon substrate confirms that carbon is the major component in thin film sample I. Next, hybrid materials fabricated from the inorganic precursor were characterized. The RBS spectrum for hybrid sample II (polymer, initiator, and PUMVS) in THF is shown in Figure 5.3b.

The shoulder starting at channel 420 represents the silicon contribution from the PUMVS in the thin film. The two lower energy peaks represent carbon and oxygen at channels 180 and 270, respectively. Comparison of the RBS spectra of samples I and II suggest that these new features result from the PUMVS in the polymer solution. Theoretical calculation of the chemical composition for this hybrid material based on the composition of the starting materials is shown in Table 5.3. Inspection of the RBS spec-

Table 5.2: Details of hybrid material fabrication conditions.

sample	materials	geometry	atmosphere
I	PI–b–PDMAEMA, dicumyl peroxide, THF	thin film	ambient
II	PI–b–PDMAEMA, dicumyl peroxide, PUMVS, THF	thin film	ambient
III	PI–b–PDMAEMA, dicumyl peroxide, PUMVS, toluene	thin film	ambient
IV	PI–b–PDMAEMA, dicumyl peroxide, PUMVS, toluene	thin film	nitrogen
V	PUMVS, dicumyl peroxide	bulk	nitrogen
VI	PUMVS, dicumyl peroxide, THF	bulk	ambient
VII	PI–b–PDMAEMA, dicumyl peroxide, PUMVS, toluene	bulk	nitrogen
VIII	PI–b–PDMAEMA, dicumyl peroxide, PUMVS, THF	bulk	ambient

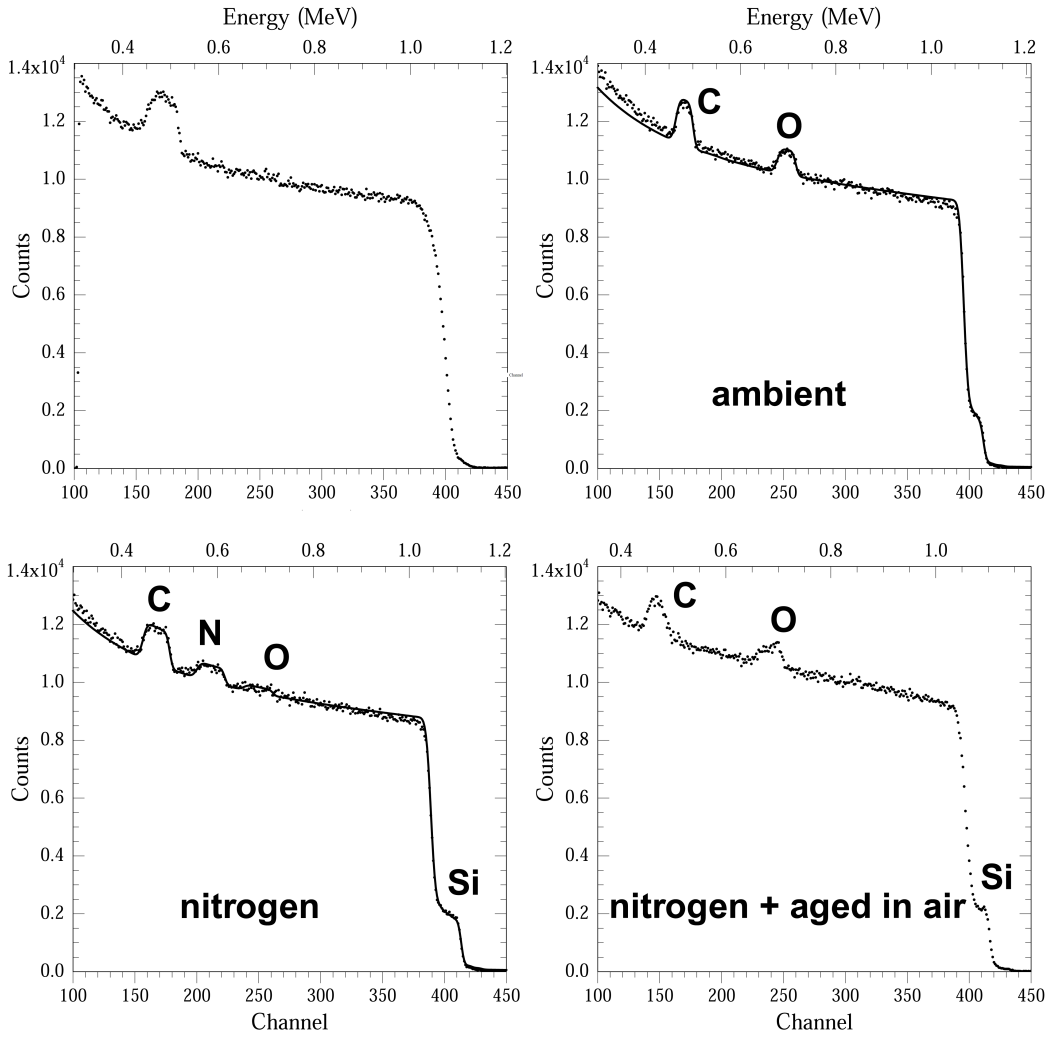

Figure 5.3: RBS spectra of for thin films. The shoulder and peaks are indexed with their elemental abbreviations. a) Sample I (polymer, initiator, THF), b) Sample II (polymer, initiator, PUMVS, THF), c) Sample IV (polymer, initiator, PUMVS, toluene), and d) from a sample similar to IV, but aged in air. Simulations from the RUMP software are overlaid in solid black for Samples II and IV

Table 5.3: Elemental characteristics in weight percentage. Sample II was fabricated in ambient atmosphere and Sample IV was done in a glovebox to protect the material from moisture.

sample	Si	O	N	C
theoretical	32.50	2.24	15.00	50.26
II	25.40	21.64	–	52.95
IV	27.08	4.60	18.14	50.18

trum shows the silicon signal as expected, but the absence of nitrogen and abundance of oxygen suggest chemical conversion occurring during hybrid mixture processing.

The relative chemical stability of the different components suggests that the chemical conversion should not occur within the PI–*b*–PDMAEMA copolymer. This is supported by the lack of an oxygen signal in the RBS spectrum of sample I, even after aging of the thin film (data not shown). Although a chemical conversion most likely occurs with the PUMVS, the source of the excess oxygen and the mechanism of its introduction required further experiments. The synthesis of hybrid sample III was carried out in toluene in an attempt to limit the amount of water introduced through the solvent. The RBS spectrum of sample III (data not shown) contains the silicon shoulder and carbon and oxygen peaks similar to spectrum II, and there is still a conspicuous absence of any nitrogen signal. Due to the low solubility of water in toluene, this result suggests that the PUMVS in the thin film is reacting with moisture from the atmosphere.

To isolate the thin film from atmospheric moisture, synthesis of sample IV was carried out in a nitrogen glovebox (see Experimental Section and Table 5.2). The sample was sealed in a media bottle prior to removal from the glovebox and loaded into the RBS chamber with minimal exposure to the atmosphere. The RBS spectrum of sample IV is shown in Figure 5.3c. The silicon shoulder and carbon peak are similar to all other spectra from PUMVS-containing samples (see Figure 5.3b). The obvious differ-

ences are the appearance of a nitrogen peak and the suppressed oxygen signal. This is in agreement with the suggested mechanism of the Si–N to Si–O conversion, by way of hydrolysis and condensation. Furthermore, the spectrum of sample IV converts to one that is similar to that of sample III with aging of the film under ambient atmosphere (see Figure 5.3d), suggesting that moisture in the air is indeed responsible for the reaction of the Si–N bond. Further supporting data comes from the RBS spectrum of a pure PUMVS/initiator film fabricated in the glovebox and transferred via sealed media bottle. This spectrum shows an enrichment of oxygen at the surface of the film (data not shown), strongly suggesting that the attack starts at the film-air interface.

The qualitative data interpretation is corroborated by quantitative analysis. Simulations of RBS spectra were created with RUMP [25] software to help determine the chemical composition of these hybrid thin film samples, see Table 5.3. The simulated spectra (solid line) are overlaid on the experimental data (circles) shown for sample II and IV in Figures 5.3b and c, respectively. Simulated spectra for the films fabricated under ambient atmosphere, samples II and III, contain the expected amount of silicon and carbon, but elevated amounts of oxygen (see Figure 5.3b). However, the complete replacement of the nitrogen accounts for this excess oxygen. This further supports the mechanism of oxidation of the Si–N bond. The simulation for sample IV provides a composition that reasonably matches with the theoretical composition (see Figure 5.3c).

Bulk

^{1}H, ^{13}C and ^{29}Si solid state NMR experiments were performed on two bulk samples of crosslinked PUMVS to gain insight in the compositional changes in the bulk due to moisture. Sample V was prepared by crosslinking a mixture of PUMVS and radical initiator inside a nitrogen glovebox and sample VI was prepared by dissolving PUMVS

and the radical initiator in THF (used as received), casting a thick film and crosslinking the sample on a hotplate under ambient atmosphere. The NMR results on these samples are shown in Figure 5.4 and are summarized in Table 5.4. The results show that only the silicon spectra are significantly different for the two samples. The ^{1}H NMR spectra for both samples show the same peaks and have some peaks in common with the ^{1}H NMR spectrum for the non-crosslinked PUMVS (see Figure 5.2). This is expected, because crosslinking is due to vinyl group polymerization leaving the Si–CH_3 (0 ppm), N–H (0.8 ppm) and the Si-H groups (4.5 ppm) unreacted and therefore the same for all spectra.

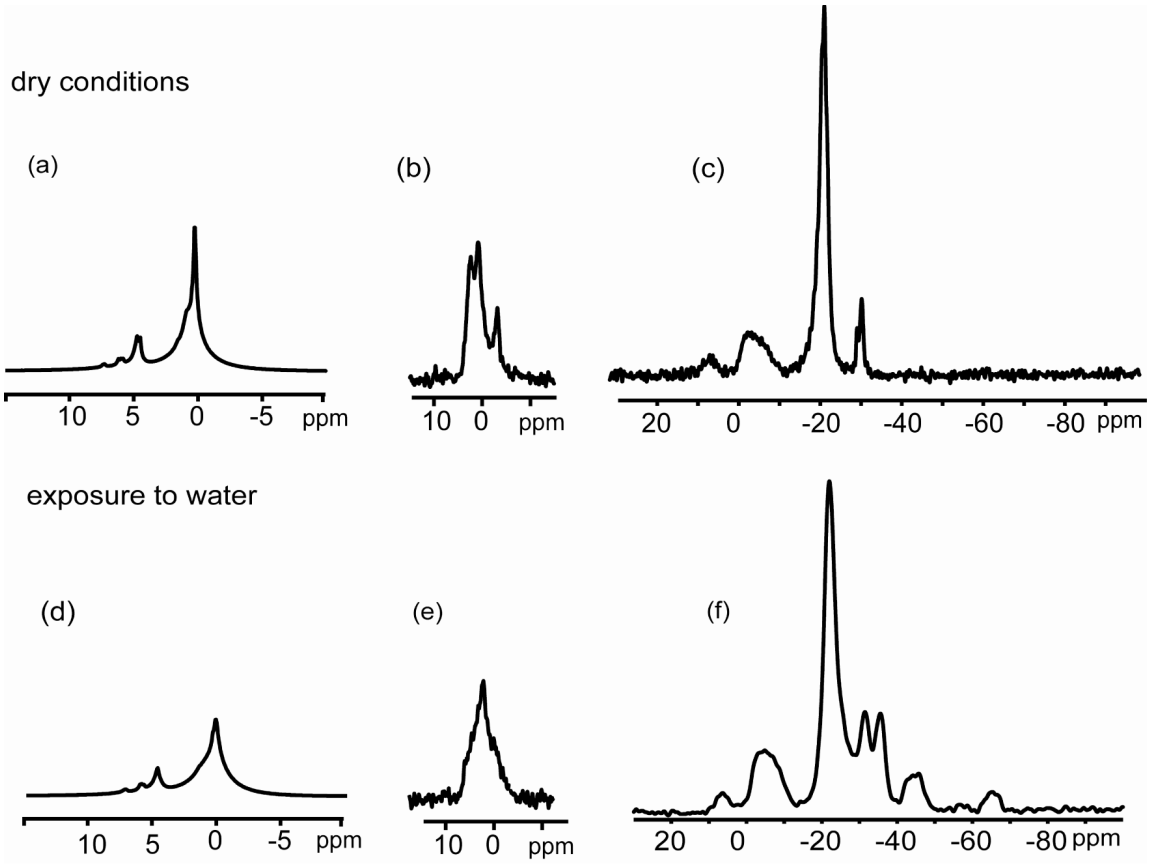

Figure 5.4: (a) ^{1}H, (b) ^{13}C and (c) ^{29}Si Solid State NMR spectra of a crosslinked PUMVS sample that is crosslinked under dry conditions. (d) ^{1}H, (e) ^{13}C and (f) ^{29}Si NMR spectra of a crosslinked PUMVS sample that is exposed to water during crosslinking

Table 5.4: Assignments for ^{1}H, ^{13}C and ^{29}Si Solid State NMR spectra for a crosslinked PUMVS sample that is exposed to water during crosslinking and for a sample that is crosslinked under dry conditions.

	Exposure to water[12, 9, 25]		**Dry conditions**	
	ppm		ppm	
^{1}H NMR	0	Si-CH_3, N-H	0.2	Si-CH_3, N-H
	4.5	Si–H	4.5	Si–H
	5.8	SiCH=CH2 (unreacted ceraset)	5.9	SiCH=CH2 (unreacted ceraset)
	7.0	Aryl group from dicumylperoxide	7.1	Aryl group from dicumylperoxide
^{13}C NMR	-4 – 7	Si – CH_3, SiCH-CH_2-	-5 – 5	Si – CH_3, SiCH-CH_2-
^{29}Si NMR	-68 - -62	CH_3SiO_3	-30	$CH_2(CH_3)SiON$
	-53	$CHSiO_2(OH)$	-21	CH_3–HSi–N_2
	-49- - 41	$H(CH_3)SiO_2$, $CH_2(CH_3)SiO_2$	-10 - 0	C_2–Si–N_2
	-35	$H(CH_3)SiON$	7	H_3N-HSi-N/ H_3N-SiCH_3-N end groups
	-31	$CH_2(CH_3)SiON$		
	-22	CH_3–HSi–N_2		
	-12 - 0	C_2–Si–N_2		
	7	H_3N-HSi-N/ H_3N-SiCH_3-N end groups		

The spectra show two small peaks at 6.0 ppm and 7.0 ppm, these peaks are assigned to unreacted SiCH=CH_2 and aryl groups in the dicumyl peroxide, respectively. The ^{13}C NMR spectra for both samples show a group of peaks around 0 ppm, which can be assigned to the Si-CH_3 groups and the SiCH_2-CH_2 groups.[14] The peaks of the vinyl groups are not observed anymore, whereas some unreacted SiCH=CH_2 groups were observed in the hydrogen spectrum, probably due to the reduced signal-to-noise ratio for the ^{13}C NMR spectrum. The ^{29}Si NMR spectrum for the sample that is crosslinked under dry conditions (sample V) shows four peaks. The broad peak around 0 – -10ppm and the peak at -21 ppm were expected and can be assigned to C_2–Si–N_2 and CH_3–HSi–N_2, respectively.[14] The peak at 7 ppm is assigned to H_3N–HSi–N or H_3N–SiCH_3–N end

groups and the peak at -30 ppm to $CH_2(CH_3)SiON$ groups. The ^{29}Si NMR spectrum for the sample that is crosslinked under ambient atmosphere (sample VI) deviates from the expected spectrum and shows no less than eight peaks. The first four peaks at 7, 0 – -10, -21 and -30 ppm are the same as for the other sample and can be assigned to the same groups. The additional peaks at -35, -45, -53 and -65 ppm can be assigned to $H(CH_3)SiON$, $H(CH_3)SiO_2$/ $CH_2(CH_3)SiO_2$, $(CH_3)SiO_2(OH)$ and CH_3SiO_3, respectively, in agreement with solid state NMR data on silicon oxycarbides [26].

The results corroborate the suggestion that the Si–N bond is attacked by water forming Si–OH bonds, convert to Si–O–Si bridges, evolving a molecule of ammonia in the process. In this scenario all the Si–N can be attacked, which means that all silicon atoms can be bonded to two oxygen atoms. The peak at -65ppm suggests that a silicon atom can be bonded to even three oxygen atoms. We believe that in addition to the Si-N bond the Si-H bond can be attacked as well. The relative decrease in intensity of the CH_3-HSi-N_2 groups at -22 ppm corroborates this. The fact that the spectra of the sample prepared under dry conditions also shows a peak at -30 ppm ($CH_2(CH_3)SiON$) can be explained by the fact that the NMR experiments were not performed right after the synthesis of the samples. In the period between synthesis and measurement the crosslinked film may have reacted with some source of moisture.

More ^{13}C and ^{29}Si solid state NMR experiments were performed on PUMVS/PI-*b*-PDMAEMA hybrids to investigate the influence of the block copolymer on the chemical composition of the hybrids synthesized under different conditions. Reactions of a block copolymer with PUMVS were described before by Wan et al where the hydroxy chain ends of the PB–*b*–PEO block copolymer react with PUMVS.[18] This kind of reaction is not expected in the current system, however, since the PI-*b*-PDMAEMA does not contain a hydroxyl end group. Again two samples were prepared; one under dry condi-

tions (sample VII) and the other under ambient atmosphere (sample VIII), but this time PI-*b*-PDMAEMA was added to obtain nanocomposites (see Experimental Part). Figure 5.5 shows the ^{13}C and ^{29}Si solid-state NMR spectra for both samples and Table 5.5 summarizes the results. The ^{13}C NMR spectra are again very similar for both samples and all the peaks are expected and can be assigned to groups in the block copolymer or crosslinked PUMVS. The ^{29}Si spectra for the hybrid samples (VII, VIII) are very similar to the ^{29}Si spectra for the crosslinked PUMVS (V, VI); the spectra of the samples prepared under dry conditions (V, VII) are almost identical. The same is true for the samples prepared under ambient atmosphere (VI, VIII). The ^{13}C NMR data suggests that the block copolymer does not react with PUMVS and from the combined ^{13}C and ^{29}Si NMR data it appears that the block copolymer does not influence the reaction of PUMVS with water.

The NMR and RBS data are consistent and suggest that PUMVS is susceptible to reaction with water. Not many previous reports regarding PUMVS mention its reactivity with water. We think that is because in contrast to most other studies we focus on relatively thin films. This is in agreement with the literature that does mention the reactivity with water [15, 27]; all of them report on the synthesis of relatively small structures, i.e. structures with large surface-to-volume ratios.

Morphology control

Now that we have established how to control the chemical composition of the PI-*b*-PDMAEMA/PUMVS hybrids we subsequently want to demonstrate that several morphologies can be obtained by systematically increasing the inorganic/ organic ratio. To this end we used one block copolymer that contains 10 wt% PDMAEMA (polymer A, see Table 5.1) and cast films (see Experimental Part) with inorganic/ organic ratios of

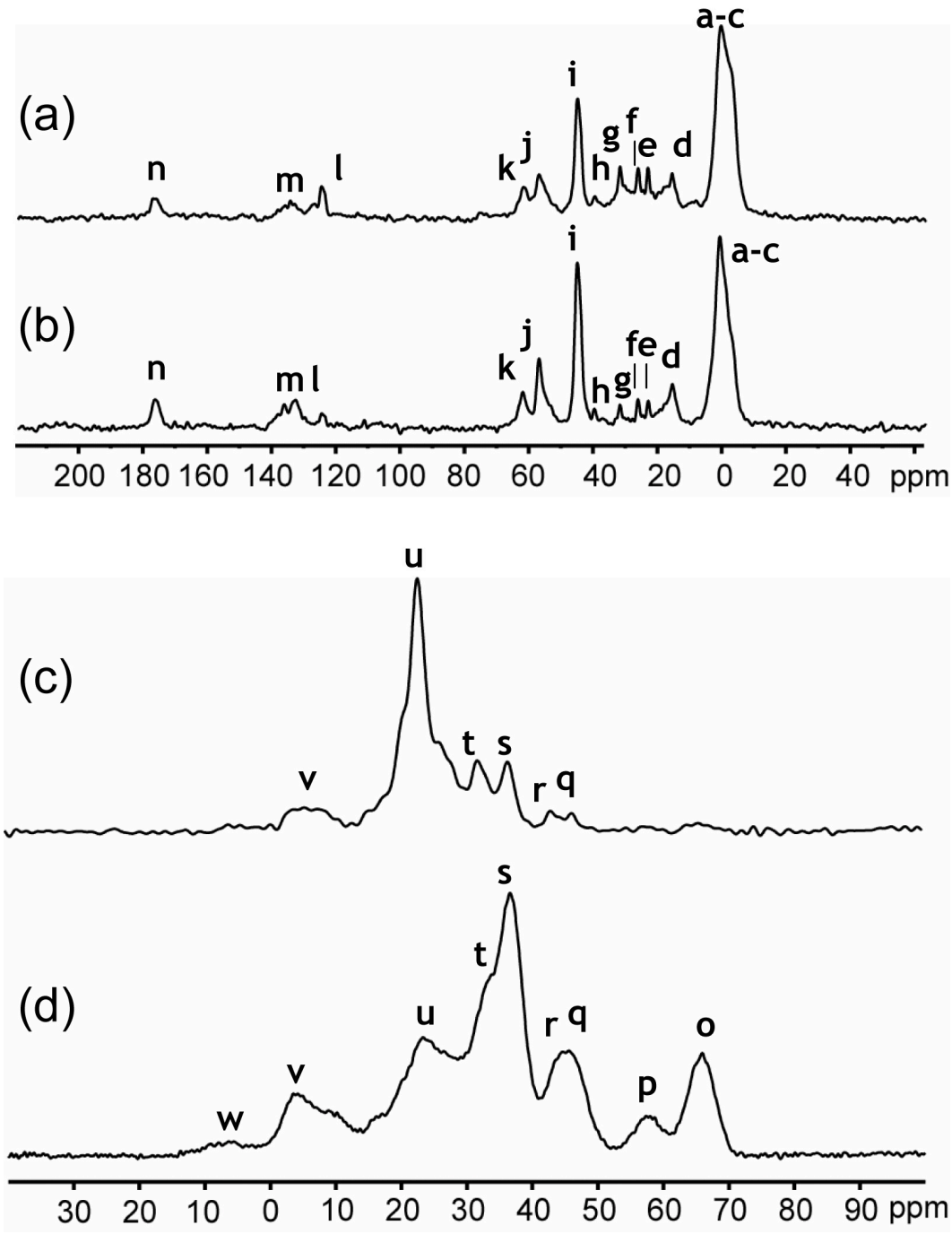

Figure 5.5: (a) ^{13}C and (c) ^{29}Si Solid State NMR spectra of a crosslinked block copolymer PUMVS hybrid sample that is crosslinked under dry conditions. (b) ^{13}C and (d) ^{29}Si NMR spectra of a crosslinked block copolymer PUMVS hybrid sample crosslinked under ambient atmosphere.

Table 5.5: Assignments for ^{13}C and ^{29}Si Solid State NMR spectra for a crosslinked block copolymer PUMVS hybrid sample that is exposed to water during crosslinking and for a sample that is crosslinked under dry conditions.

Crosslinked PUMVS				**PI-b-PDMAEMA**		
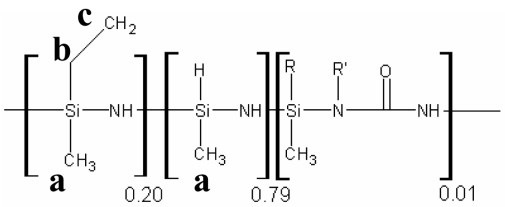				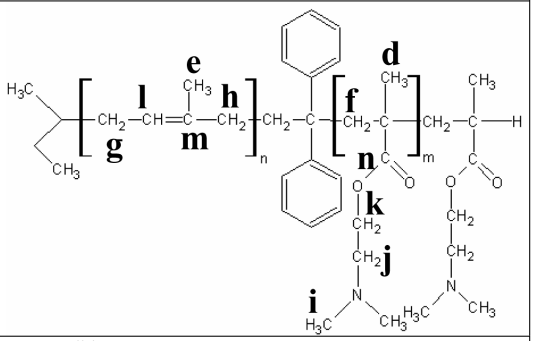		
	Exposure to water			Dry conditions		
	ppm	Crosslinked PUMVS (expected[9])	PI-*b*-PDMAEMA (expected[27,28])	ppm	Crosslinked PUMVS (expected[9])	PI-*b*-PDMAEMA (expected[27,28])
^{13}C NMR	1.27	**a** Si – CH_3 **b,c** SiCH-CH_2-		1.27	**a** Si – CH_3 **b,c** SiCH-CH_2-	
	16.02		**d** – CH_3	16.02		**d** – CH_3
	23.55		**e** – CH_3	23.55		**e** – CH_3
	26.71		**f** – CH_2	26.71		**f** – CH_2
	32.32		**g** – CH_2	32.32		**g** – CH_2
	40.30		**h** – CH_2	40.30		**h** – CH_2
	45.59		**i** N– CH_3	45.59		**i** N– CH_3
	57.48		**j** N – CH_2	57.48		**j** N – CH_2
	62.53		**k** O – CH_2	62.53		**k** O – CH_2
	125.10		**l** = CH	125.10		**l** = CH
	136.73		**m** = C	136.73		**m** = C
	176.93		**n** C = O	176.93		**n** C = O
	ppm	Crosslinked PUMVS (expected[9])	unexpected[25]	ppm	Crosslinked PUMVS (expected[9])	unexpected[25]
^{29}Si NMR	-65.95		**o** CH_3SiO_3	-46.54		**q** $CH_2(CH_3)SiO_2$
	-57.37		**p** $(CH_3)SiO_2$ (OH)	-43.31		**r** $H(CH_3)SiO_2$
	-45.58		**q** $CH_2(CH_3)SiO_2$	-36.76		**s** $H(CH_3)SiON$
			r $H(CH_3)SiO_2$	-32.15		**t** $CH_2(CH_3)SiON$
	-36.60		**s** $H(CH_3)SiON$	-23.00	**u** CH_3–HSi–N_2	
			t $CH_2(CH_3)SiON$	-5.74	**v** C_2–Si–N_2	
	-23.32	**u** CH_3–HSi–N_2				
	-3.54	**v** C_2–Si–N_2				
	6.34	**w** H_3N-HSi-N/ H_3N-SiCH_3-N end groups				

0.5 (sample 1), 1.5 (sample 2) and 2.5 (sample 3). SAXS traces of samples 1 and 3 (Figure 5.6a) both show peaks with q spacing ratios of 1,$\sqrt{3}$, and $\sqrt{4}$, consistent with hexagonally packed domains, whereas sample 2 shows peaks with q spacing ratios of 1, 2 and 3, consistent with a lamellar morphology. Transmission electron microscopy (TEM) was performed to corroborate these assignments. Representative TEM images of the three composites are shown in Figures 5.7a-c. The contrast arises from the density difference between PI and PDMAEMA/PUMVS domains, the latter appearing darker. Figure 5.7a (sample 1) clearly shows dark cylinders packed in a light matrix, which translates to PDMAEMA/PUMVS cylinders in a PI matrix. Figure 5.7b (sample 2) and 5.7c (sample 3) show alternating layers of PI and PDMAEMA/PUMVS domains and PI cylinders in a PDMAEMA/PUMVS matrix, respectively.

The d-spacing, and thereby the size of the domains, can be tuned as well by varying the molecular weight of the parent block copolymer. Sample 4 was synthesized using a block copolymer with a molecular weight of 31 000 g/mol (polymer C), which is much smaller than the 88 900 g/mol of the polymer used to synthesize samples 1 to 3 (see Table 5.1). The SAXS diffractogram of sample 4, composed of polymer C with a weight fraction of 33% PDMAEMA and an inorganic/organic ratio of 2, is shown in Figure 5.6b. The SAXS trace shows peaks with q spacing ratios of 1, $\sqrt{4}$, and $\sqrt{7}$, consistent with hexagonally packed domains. Comparison of samples 3 and 4, both exhibiting a hexagonal structure, shows a significant shift in d-spacing from 53.7 nm to 28.6 nm indicating the tunability of the domain size. Sample 4 was calcined to 1500 $^{\circ}$C under Ar/H_2 (see Experimental Part) to remove the organic material and convert the PUMVS into a mesoporous ceramic material (sample 5). The SAXS diffractogram of sample 5 contains peaks with q spacing ratios of 1, $\sqrt{3}$, and $\sqrt{4}$ (see Figure 5.6b) showing that the hexagonal structure is preserved. The spectrum of sample 5 is shifted

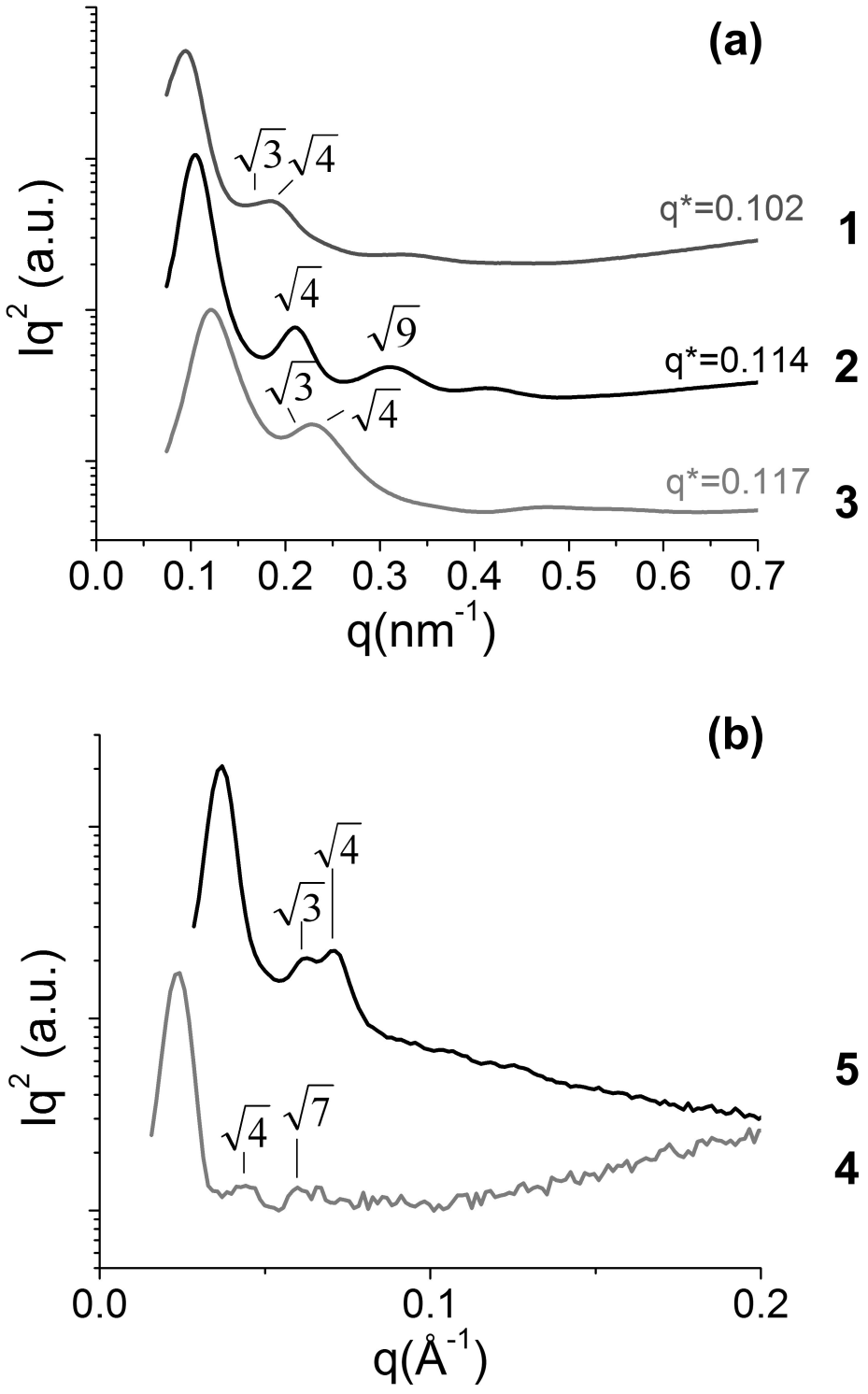

Figure 5.6: (a) SAXS traces of different morphologies of as-made composites by adding different amounts of inorganic to one polymer; 1. hexagonal cylinder morphology, 2. lamellar morphology and 3. hexagonal cylinder morphology. (b) SAXS traces for the as-made composite (4) and the resulting ceramic after calcinations to 1500 °C (5). Peak positions as expected for a hexagonal cylinder morphology are indicated by arrows.

to higher q-values compared to the composite (sample 4) indicating that the sample shrinks upon calcination. TEM images (Figure 5.7e) corroborated that the pores remain accessible and the hexagonal structure is preserved upon heating to 1500 °C.

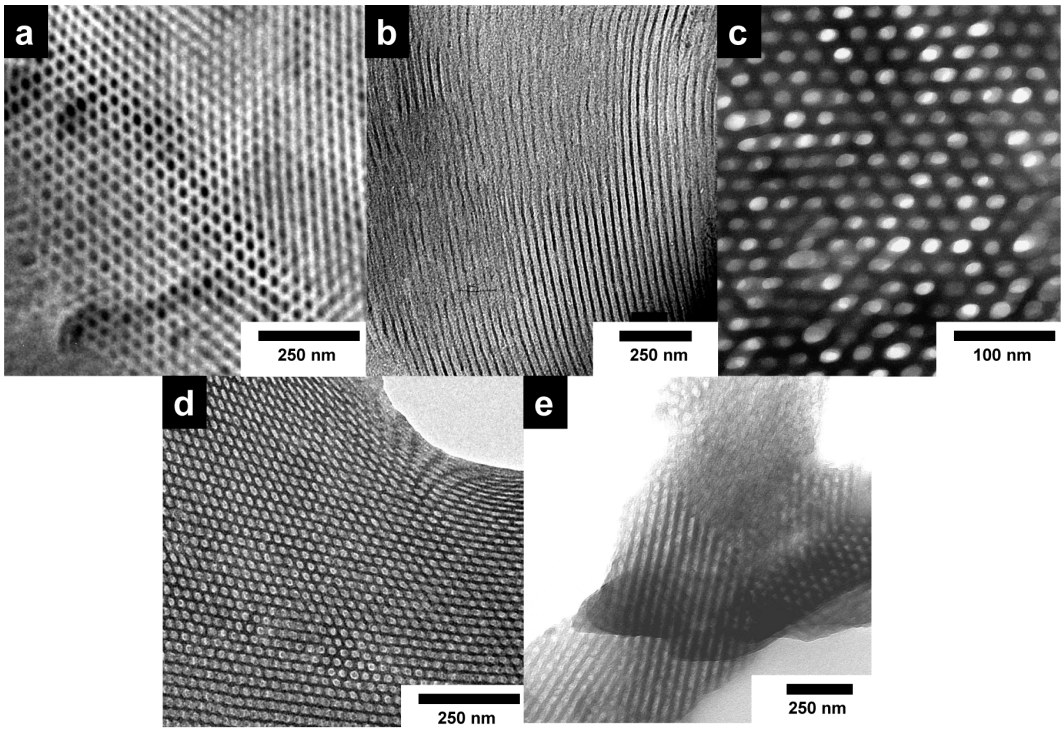

Figure 5.7: Bright-field TEM images of different morphologies of as-made composites by adding different amounts of inorganic to one polymer; (a) hexagonal cylinder morphology, (b) lamellar morphology and (c) hexagonal cylinder morphology. Bright-field TEM images for the as-made composite (d) and the resulting ceramic after calcinations to 1500 °C (e), demonstrating that the hexagonal structure is preserved during heat treatment.

Conclusion

In this full report we showed that the amphiphilic block copolymer PI-*b*-PDMAEMA can be used as a structure directing agent for PUMVS, a precursor for high temperature ceramics. We demonstrated that PUMVS is very susceptible to reaction with water, upon

which the chemical composition of the hybrid materials is changed from mainly Si-H-C-N to predominantly Si-H-C-O. Solid state NMR and RBS data showed that preparation and storage under dry conditions prevented reaction with water preserving the original chemical composition. Furthermore, we showed that by systematically increasing the inorganic/ organic ratio different morphologies can be obtained and by changing the molecular weight of the block copolymer the domain sizes can be tuned. High temperature treatment up to 1500°C resulted in a ceramic while retaining the morphology of the original hybrid material. This bottom-up approach provides a versatile method to synthesize mesostructured high temperature ceramics with tunable morphology and domain size, which may lead to materials with exciting new mechanical, thermal and chemical properties.

Bibliography

[1] C. T. Kresge, M. E. Leonowicz, W. J. Roth, J. C. Vartuli, and J. S. Beck. "Ordered mesoporous molecular-sieves synthesized by a liquid-crystal template mechanism" *Nature*, **1992**, *359*, 710.

[2] M. Templin, A. Franck, A. DuChesne, H. Leist, Y. M. Zhang, R. Ulrich, V. Schadler, and U. Wiesner. "Organically modified aluminosilicate mesostructures from block copolymer phases" *Science*, **1997**, *278*, 1795.

[3] D. Y. Zhao, J. L. Feng, Q. S. Huo, N. Melosh, G. H. Fredrickson, B. F. Chmelka, and G. D. Stucky. "Triblock copolymer syntheses of mesoporous silica with periodic 50 to 300 angstrom pores" *Science*, **1998**, *279*, 548.

[4] P. D. Yang, D. Y. Zhao, D. I. Margolese, B. F. Chmelka, and G. D. Stucky. "Generalized syntheses of large-pore mesoporous metal oxides with semicrystalline frameworks" *Nature*, **1998**, *396*, 152.

[5] B. K. Cho, A. Jain, S. Mahajan, H. Ow, S. M. Gruner, and U. Wiesner. "Nanohybrids from liquid crystalline extended amphiphilic dendrimers" *Journal of the American Chemical Society*, **2004**, *126*, 4070.

[6] C. Garcia, Y. M. Zhang, F. DiSalvo, and U. Wiesner. "Mesoporous aluminosilicate materials with superparamagnetic gamma-fe2o3 particles embedded in the walls" *Angewandte Chemie-International Edition*, **2003**, *42*, 1526.

[7] C. B. W. Garcia, Y. M. Zhang, S. Mahajan, F. DiSalvo, and U. Wiesner. "Self-assembly approach toward magnetic silica-type nanoparticles of different shapes from reverse block copolymer mesophases" *Journal of the American Chemical Society*, **2003**, *125*, 13310.

[8] P. Du, M. Q. Li, K. Douki, X. F. Li, C. B. W. Garcia, A. Jain, D. M. Smilgies, L. J. Fetters, S. M. Gruner, U. Wiesner, and C. K. Ober. "Additive-driven phase-selective chemistry in block copolymer thin films: The convergence of top-down and bottom-up approaches" *Advanced Materials*, **2004**, *16*, 953.

[9] Y. L. Li, E. Kroke, R. Riedel, C. Fasel, C. Gervais, and F. Babonneau. "Thermal cross-linking and pyrolytic conversion of poly(ureamethylvinyl)silazanes to silicon-based ceramics" *Applied Organometallic Chemistry*, **2001**, *15*, 820.

[10] S. R. Shah and R. Raj. "Mechanical properties of a fully dense polymer derived ceramic made by a novel pressure casting process" *Acta Materialia*, **2002**, *50*, 4093.

[11] R. Raj, R. Riedel, and G. D. Soraru. "Introduction to the special topical issue on ultrahigh-temperature polymer-derived ceramics" *Journal of the American Ceramic Society*, **2001**, *84*, 2158.

[12] D. Seyferth, C. Strohmann, N. R. Dando, and A. J. Perrotta. "Poly(ureidosilazanes) - preceramic polymeric precursors for silicon carbonitride and silicon-nitride - synthesis, characterization, and pyrolytic conversion to si3n4/sic ceramics" *Chemistry of Materials*, **1995**, *7*, 2058.

[13] J. M. Schwark. "Isocyanate-modified polysilazane ceramic precursors" *Polymer Preprints*, **1991**, *32*, 567.

[14] Y. F. Shi, Y. Meng, D. H. Chen, S. J. Cheng, P. Chen, H. F. Yang, and D. Y. Zhao. "Highly ordered mesoporous silicon carbide ceramics with large surface areas and high stability" *Advanced Functional Materials*, **2006**, *16*, 561.

[15] I. K. Sung, Christian, M. Mitchell, D. P. Kim, and P. J. A. Kenis. "Tailored macroporous sicn and sic structures for high-temperature fuel reforming" *Advanced Functional Materials*, **2005**, *15*, 1336.

[16] C. B. W. Garcia, C. Lovell, C. Curry, M. Faught, Y. M. Zhang, and U. Wiesner. "Synthesis and characterization of block copolymer/ceramic precursor nanocomposites based on a polysilazane" *Journal of Polymer Science Part B-Polymer Physics*, **2003**, *41*, 3346.

[17] M. Kamperman, C. B. W. Garcia, P. Du, H. S. Ow, and U. Wiesner. "Ordered mesoporous ceramics stable up to 1500 degrees c from diblock copolymer mesophases" *Journal of the American Chemical Society*, **2004**, *126*, 14708.

[18] J. L. Wan, A. Alizadeh, S. T. Taylor, P. R. L. Malenfant, M. Manoharan, and S. M. Loureiro. "Nanostructured non-oxide ceramics templated via block copolymer self-assembly" *Chemistry of Materials*, **2005**, *17*, 5613.

[19] S. Renker. *Neue Blockcopolymersysteme zur Strukturierung organisch-anorganischer Hybridmaterialen*. PhD thesis, Max Planck Institute for Polymer Research, 2003.

[20] S. Creutz, P. Teyssie, and R. Jerome. "Living anionic homopolymerization and block copolymerization of (dimethylamino)ethyl methacrylate" *Macromolecules*, **1997**, *30*, 6.

[21] B. M. Fung, A. K. Khitrin, and K. Ermolaev. "An improved broadband decoupling sequence for liquid crystals and solids" *Journal of Magnetic Resonance*, **2000**, *142*, 97.

[22] M. A. Hillmyer, P. M. Lipic, D. A. Hajduk, K. Almdal, and F. S. Bates. "Self-assembly and polymerization of epoxy resin amphiphilic block copolymer nanocomposites" *Journal of the American Chemical Society*, **1997**, *119*, 2749.

[23] P. M. Lipic, F. S. Bates, and M. A. Hillmyer. "Nanostructured thermosets from self-assembled amphiphilic block copolymer/epoxy resin mixtures" *Journal of the American Chemical Society*, **1998**, *120*, 8963.

[24] Kion Ceraset technical bulletin.

[25] Information about RUMP can be obtained at the following URL: http://www.genplot.com/.

[26] H. Brequel, J. Parmentier, S. Walter, R. Badheka, G. Trimmel, S. Masse, J. Latournerie, P. Dempsey, C. Turquat, A. Desmartin-Chomel, L. Le Neindre-Prum, U. A. Jayasooriya, D. Hourlier, H. J. Kleebe, G. D. Soraru, S. Enzo, and F. Babonneau. "Systematic structural characterization of the high-temperature behavior of nearly stoichiometric silicon oxycarbide glasses" *Chemistry of Materials*, **2004**, *16*, 2585.

[27] M. Zemanova, E. Lecomte, P. Sajgalik, and R. Riedel. "Polysilazane derived micro/nano si3n4/sic composites" *Journal of the European Ceramic Society*, **2002**, *22*, 2963.

[28] M. Camail, H. Essaoudi, A. Margaillan, and J. L. Vernet. "Radical polymerization of 2-aminomethylmethacrylates with methylmethacrylate" *European Polymer Journal*, **1995**, *31*, 1119.

[29] J. W. Cook, S. Edge, D. E. Packham, and A. S. Thompson. "Thermal behavior of natural rubber and chlorinated rubber blends" *Journal of Applied Polymer Science*, **1997**, *65*, 1379.

CHAPTER 6

CONCLUSION

The transition from the traditional all-organic to hybrid organic-inorganic thin film systems is achieved through the development of phase-selective, additive-driven chemistry with block copolymers as structure directing agents. Desired materials profiles can be achieved by the proper additive selection: light sensitivity through photoacid generators and crosslinking agents, thermal and mechanical stability through aluminosilicate and silicon carbide/silicon carbonitride precursors.

Correlations between processing/composition parameters and film ordering are established through measurements made through AFM, SEM, GISAXS and quantitative analysis/simulations of experimental data. This robust "one-pot" method of hybrid thin film synthesis can tolerate many different conditions, generating mono- to multilayer assemblies with various inorganic loading fractions across different block copolymer and inorganic chemistries.

The enhanced properties provided through the inorganic additives enable the development of novel processing techniques previously unavailable to pure organic systems. The thermal stability of the mesoporous aluminosilicate thin films allows for their use as templates in a laser-driven melting of an underlying silicon substrate and capillarity-driven pore filling to create nanopillar arrays with $\sim$30 nm pitch and 10-15 nm heights. Quantitative analysis of the parent template and resultant nanopillar arrays shows efficient pattern transfer with a high pore-to-pillar conversion and retention of local six-fold symmetry. Bottom-up patterning on the nanometer length scale is augmented by top-down macroscale patterning through the use of a mask to determine the placement of these nanopillar arrays.

The extent of ordering achieved in the polymer/silica hybrid thin film is most likely at a limit with the current fabrication techniques due to the uncontrolled crosslinking of the inorganic species. The transition to the polymer/Ceraset/initiator system allows for better control over the crosslinking progress and provide additional time for defect annihilation and morphology equilibrium. Optimization of the initiator component (concentration and time of addition) and the thermal treatment cycle (temperature and duration) should greatly enhance the ordering currently found in these hybrid thin films. A shift over to the hexatic ordering regime would greatly help with the fabrication of devices that require well-defined patterns.

The nanopillar arrays can be further improved in their height uniformity and lateral correlations. Part of the lateral improvements should flow naturally from better ordered templates and it has been clearly demonstrated that the amount of deposited amorphous silicon strongly affect both parameters. Thickness optimization of the the deposited silicon to insure proper filling of each pore, while at the same time avoiding overfilling, should greatly improve the quality of the nanopillar arrays. The current method of macroscopically defining regions of nanopillar array formation can be improved by moving the mask to reside within the optics line of the excimer laser. Not only would this eliminate any sample surface–mask interactions, but it would also decrease the power density at the mask to allow repeated use. Furthermore, lithographically defined masks would insure much smaller features sizes with sharper line definition. Finally, the use of a new block copolymer chemistry to achieve the $\sim$10 nm length scale would truly allow for the integration of these synthetic surfaces with biological systems.